Canonical-basis Time-Dependent Hartree-Fock-Bogoliubov Theory and Linear-Response Calculation for Light to Heavy Nuclei

Shuichiro EBATA

February 2011

Canonical-basis Time-Dependent Hartree-Fock-Bogoliubov Theory and Linear-Response Calculation for Light to Heavy Nuclei

Shuichiro EBATA
(Doctoral Program in Physics)

Submitted to the Graduate School of
Pure and Applied Sciences
in Partial Fulfillment of the Requirements
for the Degree of Doctor of Philosophy in
Science

at the
University of Tsukuba

Abstract

We have developed a new theory to study excited states and dynamics of atomic nuclei, which we call the Canonical-basis time-dependent Hartree-Fock-Bogoliubov (Cb-TDHFB). The Cb-TDHFB is a simplified theory of the full TDHFB theory, treating pairing energy functional with a BCS-like approximation which is assumed to be diagonal in the canonical basis. Implementing the theory with a real-space and real-time method, we can describe nuclear excitations and dynamics taking account of deformation effects and pairing correlations, even for heavy nuclei with a reasonable computational costs. In this thesis, we first present a derivation of the Cb-TDHFB theory and we apply the method to linear-response calculations for even-even light to heavy nuclei and demonstrate its capability and accuracy by comparing our results with recent calculations of the quasi-particle random-phase approximation (QRPA) which is equivalent to the small amplitude limit of TDHFB, with Skyrme functionals.

We derived the Cb-TDHFB equations starting with the full TDHFB equations, introducing a simplified form for the pairing energy functional. In the derivation, we start with the ordinary TDHFB equation written in terms of the time-dependent generalized density matrix $\mathcal{R}(t)$ which is composed of the time-dependent normal density matrix $\rho(t)$ and the pairing tensor $\kappa(t)$. We then rewrite the equation in the canonical basis, which diagonalize $\rho(t)$. The derived TDHFB equations in the canonical basis has a very simple form. However, they are not useful practically for a general case since it costs much to obtain the canonical basis themselves at each time. Solving the time-dependent equation for the canonical basis is as difficult as solving the full TDHFB equation. This difficulty disappears if we employ a simplified pairing energy density functional, which is equivalent to that employed in the BCS approximation for ground state calculations.

For linear response calculations, we present results of the Cb-TDHFB calculations for excited states of some spherical and deformed nuclei to show performance of the method. We show strength functions of isovector dipole and isoscalar quadrupole excitations for some spherical and deformed nuclei. First, we show the comparison results of Cb-TDHFB with the QRPA in order to confirm the justification of canonical-basis formulation and the reduction of computational cost with this new framework. We show isoscalar quadrupole strength functions of neutron-rich nucleus ^{34}Mg for confirmation of our new method, and also discuss full self-consistent calculations of ^{24}Mg as an example of light nucleus and ^{208}Pb and ^{154}Sm as an example of heavy nuclei, in order to be clear, especially, the effects of spin-orbit and Coulomb residual interaction. Next, in order to show typical strength functions for spherical and deformed nuclei, we discuss isovector dipole and isoscalar quadrupole mode for ^{34}Si as an example of spherical nucleus, for ^{34}Mg as an example of prolate deformed nucleus and for ^{24}Ne as an example of oblate deformed nucleus. For a confirmation of computational cost of the calculation using Cb-TDHFB, we isovector dipole strength functions of deformed heavy nuclei ^{172}Yb and $^{236-240}$U. We show then the comparison our results with experimental data for photo-nuclear reaction cross sections. And we also show systematic calculations low-energy $E1$ strength which is often called Pygmy dipole resonance and which is well-known as a important strength to understand nucleosynthesis. In this thesis, we discuss the appearance of low-energy $E1$ strength functions of C, O, Ne, Mg, Si, S, Ar and Ca isotopes which are relatively light nuclei.

Contents

Chapter 1

Introduction

The main purpose of the present paper is a construction of a new theoretical method which provides a practical and universal description of nuclear reaction dynamics and elementary modes of excitation. In order to achieve this, the theory should be able to describe nuclear many-body dynamics with pairing correlations (superfluidity) which are very important for heavy nuclei. In this chapter, we give a brief introduction of basic properties of stable nuclei and of theoretical approaches developed for description of nuclear dynamics. Then, we present new features in unstable nuclei, to which the present method should be applicable.

1.1 Basic properties and theoretical models of atomic nuclei

Atomic nucleus is a self-binding finite quantum many-body system of size of several femtometers. It is composed of two kinds of fermions (protons and neutrons) with spin 1/2 with (roughly) the identical masses. The general term for protons and neutrons is “nucleons”. The number of nucleons in the biggest nucleus in nature is a few hundreds at most. However, it is still impossible to describe properties of heavy nuclei, starting from the bare nucleon-nucleon interaction. This is mainly because the Fermions require the anti-symmetrization for wave functions and the nucleon-nucleon interaction has a repulsive core in a short distance. Even if we use the latest supercomputer, the current limit of the *ab-initio* calculation is nuclei with the mass number (A) less than 12 [5]. There are about 3,000 nuclei observed in experiments (Fig. 1.1), and yet more to be discovered. Therefore, the development of effective models is essential to understand a variety of nuclear phenomena.

Nucleus has “magic numbers”, which are analogous to those in atoms. This suggests that the mean free path of a nucleon is much larger than the mean distance between nucleons. Thus, the Fermi gas model could be a useful starting point to discuss nuclear properties. The magic numbers were explained with the $j-j$ coupling shell model, proposed by M.Mayer and J.H.D.Jensen [6], with a strong spin-orbit potential. Therefore, a crude approximation of the nucleus is given by independent nucleons freely moving in an attractive average potential.

The shell model, originally proposed by Mayer and Jensen, assumed a spherical potential. This model qualitatively explains many characteristic properties of nuclei near the magic numbers in simple pictures, including single-particle (hole) states (stripping and pickup reactions),

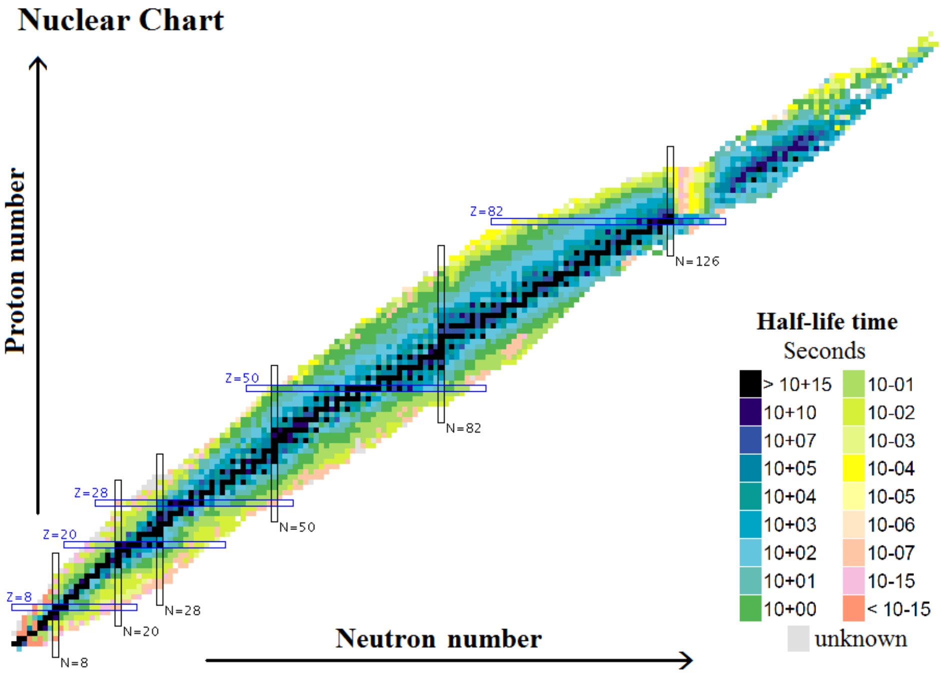

Figure 1.1: Nuclear Chart of observed isotopes. Total number of nuclei is 3175 in this figure. Each square means one nucleus and black ones correspond to stable nuclei. The numbers 2, 8, 20, . . . are called "magic number". This figure is taken from National Nuclear Data Center Home Page (http://www.nndc.bnl.gov/chart/)

magnetic moments, and low-energy spectra in odd-A nuclei. However, for nuclei whose proton and/or neutron numbers are far from the magic numbers, a simple interpretation according to the spherical shell model fails to explain nuclear properties. For instance, they were found to have the electrical quadrupole moments much larger than those predicted by the shell model [7]. It cannot be explained by the independent nucleons in the spherical mean-field potential. This fact suggests that the nucleons collectively move to enhance the quadrupole moment, which may eventually lead to a static deformation of the nucleus.

The deformation of the nucleus introduces an anisotropy that makes possible to specify an orientation of the whole system. Then, it generates the rotational degrees of freedom and exhibits rotational spectra. Vast amount of experimental data can be understood by a model that the nucleons are moving independently in a deformed potential (Nilsson model) [8]. Figure 1.2 shows the adiabatic changes of single-particle levels in a deformed Nilsson potential with respect to quadrupole deformation parameter β [9].

The nuclear deformation results from the quantum shell effects, which is a consequence of couplings between the single-particle motion and the deformed potential. This leads to an idea of the collective (unified) model by A.Bohr and B.R.Mottelson [10, 11]. Nucleons are independently moving in an average nuclear potential, while the shape of the potential slowly changes (vibrates). The shape change of the potential affects the single-particle motion, then, the change in single-particle motion leads to modification of the potential. This feedback mechanism is caused by

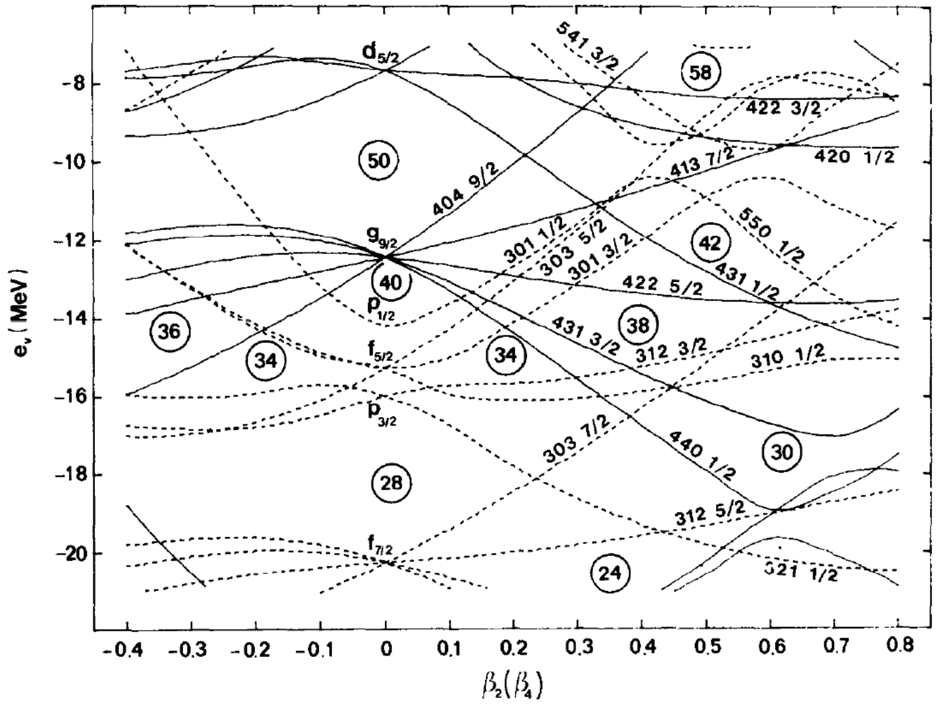

Figure 1.2: Neutron single-particle levels in the deformed Woods-Saxon potential as functions of the quadrupole deformation parameter β. This figure is taken from Ref.[9].

the coupling between them. Therefore, the Hamiltonian of the collective model contains the following three parts; the collective part to describe the vibrations of the potential shape, the nucleonic part for the single-particle motion in the potential, and the coupling terms between them.

The time-dependent mean-field theory can be regarded as a microscopic realization of the collective model, using only nucleons' degrees of freedom[1]. The time-dependent mean-field potential is constructed from the microscopic interaction among nucleons, while the nucleons are excited by motion of the mean-field potential. The self-consistency between the mean field and one-body density represents the coupling terms. There have been extensive studies using the time-dependent Hartree-Fock (TDHF) method, especially in 1970's and 1980's [12]. At later chapters, we recapitulate the TDHF theory. Many of those TDHF calculations were performed in the coordinate-space representation [13, 14, 15, 16, 17] to describe nuclear fusion and heavy-ion collision dynamics, recently they have been also carried out [18, 19, 20, 21, 22]. In the small amplitude limit, the TDHF is able to describe nuclear excitation spectra and transition densities, equivalent to the random-phase approximation (RPA) method [3]. Real-time calculations of the small-amplitude TDHF have been carried out recently [23, 24].

The RPA and TDHF are good tools to describe excited state and collective motion in nuclei,

---

[1] Since the bare nucleon-nucleon interaction has a strong repulsive core, a direct application of the mean-field approximation breaks down. Thus, historically, effective interactions, that renormalize high-momentum components of the two-body interaction, are used for the mean-field calculations [12]

however, they can not deal with an important correlation in nuclei, the pairing correlation. For instance, the nuclear binding energies are known to have a systematic variation depending on the evenness or oddness of the proton (Z) and neutron (N) numbers (Fig. 1.3). This is known as "odd-even effect" even present in the old empirical mass formula of by H.Bethe and R.Weizsäcker [25]. This odd-even effect may be described in terms of the pairing correlation. For the description of the nuclear pairing, A.Bohr, B.R.Mottelson and D.Pines successfully applied the BCS theory to nuclei [26] in the following year after the BCS theory was published [27]. The gap energy can be seen in low-lying excitation spectra (Fig. 1.4). The pairing condensate leads to the nuclear superfluidity and the moment of inertia is expected to become smaller than the rigid-body value. This is also confirmed in experiment (Fig. 1.5).

The pairing is know to be very important for nuclear collective dynamics as well. Figure 1.6 presents lifetimes of spontaneous fissioning nuclei. The lifetimes of even-even nuclei are systematically larger than those of odd-even nuclei, and those of odd-odd nuclei are even shorter [28, 29] (Fig. 1.6). The nuclear softness (deformability) significantly depends on the evenness or oddness of Z and N. The pairing correlation is supposed to be responsible for this. From these observations, we believe that the inclusion of the pairing is essential for description of dynamical properties of heavy nuclei.

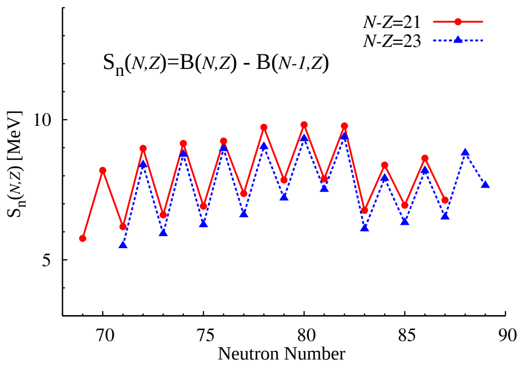

Figure 1.3: Neutron separation energies $S_n(N, Z)$ [1]. The data are taken from Ref.[30]

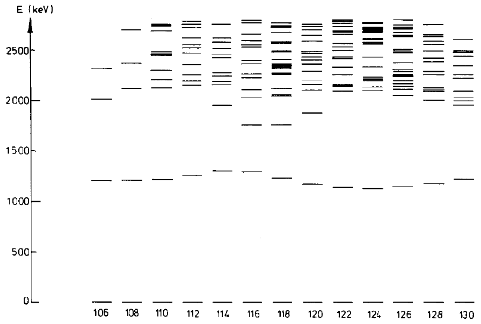

Figure 1.4: Low-lying excited states in the even-even tin isotopes below 2.8 MeV. This figure is taken from Ref.[31].

1.2 New phenomena in unstable nuclei

Structure and reaction of unstable nuclei are of great interest as current topics in nuclear physics. Recent developments of radioactive isotope facilities in the world, including RI Beam Factory (RIBF) at RIKEN, enable generation and detection of diverse rare isotopes. We are now able to experimentally investigate properties of these unknown nuclei. It demands a theoretical model that is capable of a non-empirical description of a variety of nuclear properties. This is one of the motivations for the new approach we are going to present in this article. In this section, we recapitulate interesting properties of these unstable nuclei, especially focusing on neutron skin and halo structure [33, 34], and new magic numbers [35, 36].

The density distribution of neutrons is almost identical to that of protons in stable nuclei.

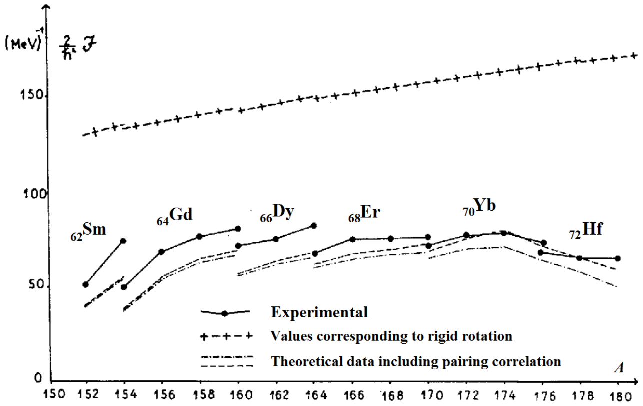

Figure 1.5: Moments of inertia of deformed nuclei as function of mass A in the so-called rare-earth region ($150 < A < 190$). Solid lines indicate experimental data, crossed line shows the rigid momentum of inertia and dashed and dot-dashed lines show the calculation with pairing correlation. This figure is taken from Ref.[32]

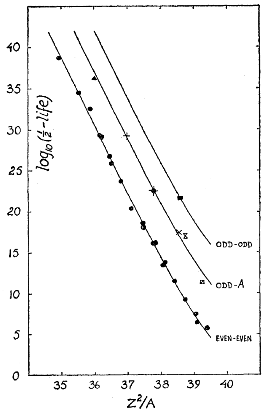

Figure 1.6: Spontaneous fission half-lives as a function of Z^2/A. From left to right, the lines indicates even-even, odd-even and odd-odd nuclei. This figure is taken from Ref.[28].

There is little difference in Fermi levels of neutrons and protons. However, the Fermi level for neutrons in neutron-rich nuclei becomes much higher than that of protons. This may lead to a significant difference in the density distribution of protons and neutrons, to produce phenomena called neutron skin and neutron halo. The neutron skin structure basically means that the neutrons and protons have different radii, thus to create a nuclear surface region in which only the neutrons exist. The neutron halo is a consequence of the weak binding of neutrons, having a very extended density distribution of neutrons because the wave function damps very weakly in a classically forbidden region, $\psi(r) \sim e^{-\kappa r}$. The most famous example of the neutron halo is ^{11}Li [33](Fig. 1.7). The neutrons of the halo nucleus is very dilute in a surface area. Theoretically, properties of the pairing in the dilute neutron matter is predicted to be very different from those in nuclear matter at the normal density. The pairing correlation at the normal density produces a Cooper pair of nucleons, that is spatially very extended, similar to the electron Cooper pair in superconductors. However, this property is drastically modified by changing the neutron density. The Cooper pair at low density is becoming very compact, which is often called “di-neutron correlation” [37]. Since two neutrons do not create a bound state in the vacuum, the real Bose-Einstein Condensation (BEC) is not realized in the neutron matter. However, the neutron density in the surface region of halo nuclei approximately corresponds to the BCS-BEC cross over region [38].

Since the structure and the correlation in the ground state are significantly modified in the neutron-rich nuclei, we may expect a new type of elementary excitations. The pygmy dipole resonance (PDR) is such an example expected to appear in unstable nuclei. The PDR is a dipole oscillation whose frequency much lower than the giant dipole resonance (GDR). It has been predicted as a collective soft-dipole excitation which is the oscillation of the core against the weakly-bound neutrons [39, 40] (see Fig. 1.8), Despite of recent experimental and theoretical studies, it has not yet been confirmed the soft-dipole picture in neutron-rich nuclei.

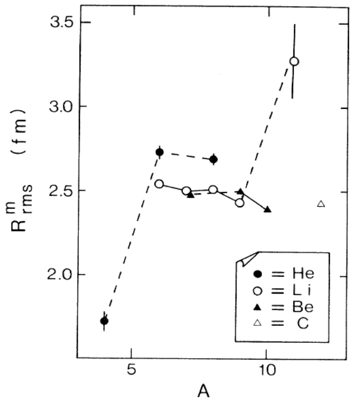

Figure 1.7: Observed matter root mean square (rms) radii for light nuclei. Lines connect isotopes only for guides. ^{11}Li has a radius much lager than the other nuclei. This figure is taken from Ref.[33]

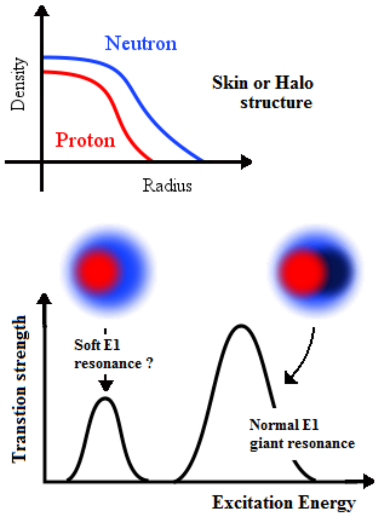

Figure 1.8: Schematic picture of the soft-$E1$ resonance. This figure is taken from Ref.[34].

The collectivity of the PDR is one of current issues in physics of unstable nuclei [41]. It should be also emphasized that the PDR plays an important role for element synthesis [42, 43].

The nuclear deformation is mainly determined by the shell effect. Therefore, we expect that nuclei near the magic numbers are spherical, which has been confirmed for stable nuclei. However, experimental data of unstable nuclei reveal a nuclear mass region, often called "island of inversion" [44], in which the nuclei are deformed even though they correspond to the magic numbers. An example with the neutron magic number 20 is shown in Fig. 1.9. It is suggested that, in this region, the magic number may change from $N = 20$ to $N = 16$ [35] (Fig. 1.10). Similar phenomena are theoretically predicted in heavier neutron-rich regions as well ($N = 40$ with $17 \leq Z \leq 25$) [45, 46, 47]. The shell structure and magic numbers are essential ingredients for understanding of nuclear structure. Since the shell effect affects the total binding energy, they are also important for element synthesis reactions, such as the determination of the path of rapid neutron capture process (r-process). A non-empirical model, which is able to describe and determine an arbitrary nuclear shape, is desirable, because we may encounter unknown phenomena. The discovery of the island of inversion gives us a lesson that it may be dangerous to make an assumption according to the common sense in physics of stable nuclei.

1.3 Purpose of the present study and outline of this paper

The purpose of this study is to construct a feasible method which can universally describe properties of nuclei in the entire nuclear chart, including stable and unstable nuclei. The method should be able to describe properties of stable nuclei and also applicable to new phenomena in unstable nuclei. In order to predict properties of unknown nuclei, it is essential for the model to possess a predictive power without adjusting parameters from nucleus to nucleus. With

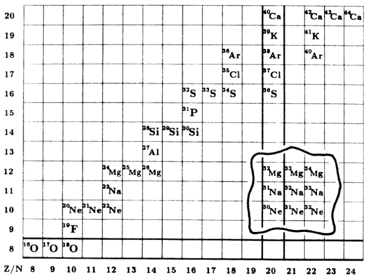

Figure 1.9: Partial periodic table highlighting the "island of inversion" centered at ^{32}Na. The "inversion" means that the ordering of some single-particle levels are inverted in this region. The magic numbers $Z = 8$ and $N = 20$ are emphasized with bold lines. This figure is taken from Ref.[44]

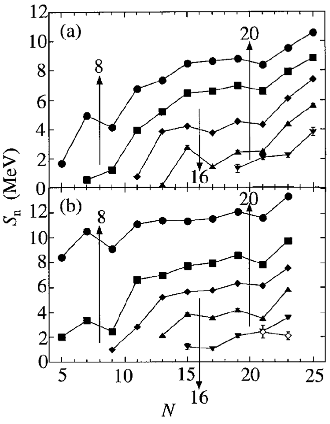

Figure 1.10: Neutron number (N) dependence of observed neutron separation energy S_n for (a) nuclei with odd N and even Z, and for (b) nuclei with odd N and odd Z. The arrows indicate to magic numbers. This figure is taken from Ref.[35].

this respect, the self-consistent mean-field (density-functional) models are superior to other approaches. They are also computationally feasible. Using the parallel supercomputers, a systematic calculation of the ground-state properties of all nuclei can be achieved in several hours [48].

In order to describe reaction dynamics and nuclear response properties, the time-dependent mean-field approach would be a good candidate. The TDHF theory, previously mentioned, can be extended to the one applicable to superfluid nuclei. The inclusion of the pairing correlation leads to the "time-dependent Hartree-Fock-Bogoliubov" (TDHFB) theory. However, it requires enormous computational resources because the number of orbitals to treat is, in principle, infinite. Only recently, a few attempts of the TDHFB have been done for realistic applications, but either with a spherical restriction [49] or with a small model space [50].

The small-amplitude limit of the TDHFB is identical to the quasi-particle RPA (QRPA). For spherical nuclei, there have been extensive studies with the QRPA to investigate excited states in stable and unstable nuclei [51, 39]. The QRPA methods with the coupling with continuum state are also in progress [52, 53, 54]. Very recently, the QRPA calculations have become possible for nuclei with axially deformed ground states [55, 56, 57]. However, the fully self-consistent QRPA calculation including the spin-orbit and residual Coulomb interactions requires a massive computational cost. For example, in Ref.[57], the calculation was performed in a massively parallel computer using ten thousands of CPU's.

In this thesis, we propose an alternative yet feasible approach, "Canonical-basis TDHFB" (Cb-TDHFB) in the three-dimensional coordinate-space representation. The Cb-TDHFB is formulated in the canonical-basis representation and an approximation for the pair potential leads to a simple theory that requires the computational cost much smaller than the full TDHFB calculation. We show a basic idea and the derivation of the Cb-TDHFB equations. Then, as the first numerical application, we apply the method to calculation of the linear response, to show the strength distributions calculated with the real-time approach. We compare the result of the Cb-TDHFB with those of recent QRPA calculations, to demonstrate the validity and accuracy of the Cb-TDHFB method. The dynamical effects of the pairing correlation will be addressed.

This thesis is organized as follows. In Chapter 2, we derive the basic equations of Cb-TDHFB method. According to a pairing energy functional, it may require a careful treatment on the time-dependent phases of the canonical states. In Chapter 3, we show details of numerical calculation. In Chapter 4, we show results for the strength functions of isovector dipole and isoscalar quadrupole modes. The subjects of nuclei are in light ones, carbon (C), oxygen (O), neon (Ne), magnesium (Mg), silicon (Si), sulfur (S), argon (Ar), calcium (Ca) isotopes, and in heavy ones are samarium (Sm) and uranium (U) isotopes and zirconium of 90 (^{90}Zr), ytterbium of 172 (^{172}Yb) and lead of 208 (^{208}Pb). First, we compare our results with other calculations in order to confirm the accuracy of Cb-TDHFB method as time-dependent scheme. And we show the basic properties of deformed nucleus and the effects of pairing correlation on isovector dipole and isoscalar quadrupole modes of each deformed nucleus. And we discuss the full self-consistency and computational cost of Cb-TDHFB with calculation results, we compare Cb-TDHFB results with experimental data from light to heavy nuclei. Then we show the properties and effects of pairing on pygmy dipole resonances for nuclei up to $A = 64$. Finally, the summary and future work of this study are given in Chapter 5.

Chapter 2

Formulation

2.1 Time-dependent mean field theory

In this section, we show the derivations of time-dependent Hartree-Fock (TDHF) and time-dependent Hartree-Fock-Bogoliubov (TDHFB) equations in order to lead to the canonical-basis TDHFB. We need some preparations.

We start to derive TDHF(B) equations from time-dependent many-body Schrödinger equation. We set a time-dependent many-body wave function $|\Phi(t)\rangle$. When this $|\Phi(t)\rangle$ obey the many-body Schrödinger equation, the time evolution of $|\Phi(t)\rangle$ is given by

$$|\Phi(t)\rangle = e^{-iHt/\hbar}|\Phi(0)\rangle. \tag{2.1}$$

We assume Hamiltonian H is the sum of a kinetic energy and a two-body interaction. H can be written with a Fermion creation and annihilation operator by

$$H = \sum_{\alpha,\beta} t_{\alpha\beta} c^\dagger_\alpha c_\beta + \frac{1}{4}\sum_{\alpha,\beta,\mu,\nu} \bar{\mathcal{V}}_{\alpha\beta\mu\nu} c^\dagger_\alpha c^\dagger_\beta c_\nu c_\mu, \tag{2.2}$$

where $\bar{\mathcal{V}}_{\alpha\beta\mu\nu} = \mathcal{V}_{\alpha\beta\mu\nu} - \mathcal{V}_{\alpha\beta\nu\mu}$ and Fermion operators obey $\{c_i, c^\dagger_j\} = \delta_{ij}$. We set the time-dependent normal density matrix $\rho(t)$ and pairing tensor $\kappa(t)$ as

$$\rho_{ij}(t) \equiv \langle\Phi(t)|c^\dagger_j c_i|\Phi(t)\rangle, \tag{2.3}$$

$$\kappa_{ij}(t) \equiv \langle\Phi(t)|c_j c_i|\Phi(t)\rangle. \tag{2.4}$$

When we regard that the time-evolution of $|\Phi(t)\rangle$ obey Eq.(2.1), to obtain an equation of motion, we can calculate their time derivative:

$$i\hbar\frac{\partial}{\partial t}\rho_{ij}(t) = \langle\Phi(t)|[c^\dagger_j c_i, H]|\Phi(t)\rangle, \tag{2.5}$$

$$i\hbar\frac{\partial}{\partial t}\kappa_{ij}(t) = \langle\Phi(t)|[c_j c_i, H]|\Phi(t)\rangle. \tag{2.6}$$

In order to expand the commutation relation $[c_j^\dagger c_i, H]$, we use followings

$$\begin{aligned}
[c_j^\dagger c_i, c_\alpha^\dagger c_\beta] &= c_j^\dagger c_\beta \delta_{i\alpha} - c_\alpha^\dagger c_i \delta_{\beta j}, \\
[c_j^\dagger c_i, c_\alpha^\dagger c_\beta^\dagger c_\nu c_\mu] &= c_j^\dagger c_\beta^\dagger c_\nu c_\mu \delta_{i\alpha} - c_j^\dagger c_\alpha^\dagger c_\nu c_\mu \delta_{i\beta} - c_\alpha^\dagger c_\beta^\dagger c_i c_\mu \delta_{j\nu} + c_\alpha^\dagger c_\beta^\dagger c_i c_\nu \delta_{j\mu}.
\end{aligned}$$

And in order to expand the commutation relation $[c_j c_i, H]$, we use followings

$$\begin{aligned}
[c_j c_i, c_\alpha^\dagger c_\beta] &= c_j c_\beta \delta_{i\alpha} - c_i c_\beta \delta_{j\alpha}, \\
[c_j c_i, c_\alpha^\dagger c_\beta^\dagger c_\nu c_\mu] &= c_\alpha^\dagger c_j c_\nu c_\mu \delta_{i\beta} - c_\alpha^\dagger c_i c_\nu c_\mu \delta_{j\beta} + c_j c_\beta^\dagger c_\nu c_\mu \delta_{i\alpha} - c_i c_\beta^\dagger c_\nu c_\mu \delta_{j\alpha}.
\end{aligned}$$

2.1.1 Time-dependent Hartree-Fock theory (TDHF)

In the TDHF theory, the many-body wave function $|\Phi(t)\rangle$ is replaced with a single Slater determinant as

$$|\Phi(t)\rangle \equiv \prod_{i=1}^{N} c_i^\dagger |0\rangle, \tag{2.7}$$

where N is the number of particles in the system. This wave function is called Hartree-Fock (HF) state, and this replacement is Hartree-Fock approximation. HF state can not deal with κ, so TDHF equation is written by only the time-derivative of ρ. Eq.(2.5) can be expanded then in HF state as

$$\begin{aligned}
i\hbar \frac{\partial}{\partial t} \rho_{ij} &= \sum_\beta t_{i\beta} \rho_{\beta j} - \sum_\alpha t_{\alpha j} \rho_{i\alpha} \\
&+ \frac{1}{2} \sum_{\beta,\mu,\nu} \bar{\mathcal{V}}_{i\beta\mu\nu} \big(\rho_{\nu\beta} \rho_{\mu j} - \rho_{\mu\beta} \rho_{\nu j} \big) \\
&- \frac{1}{2} \sum_{\alpha,\beta,\mu} \bar{\mathcal{V}}_{\alpha\beta\mu j} \big(\rho_{i\beta} \rho_{\mu\alpha} - \rho_{i\alpha} \rho_{\mu\beta} \big) \\
&= \sum_\mu \{ (t_{i\mu} + \Gamma_{i\mu}) \rho_{\mu j} - \rho_{i\mu} (t_{\mu j} + \Gamma_{\mu j}) \} = [h, \rho]_{ij},
\end{aligned} \tag{2.8}$$

where we introduce $\Gamma_{\alpha\mu} \equiv \sum_{\beta\nu} \bar{\mathcal{V}}_{\alpha\beta\mu\nu} \rho_{\nu\beta}$ called HF potential, $h \equiv t + \Gamma$ so-called single-particle Hamiltonian and the Eq.(2.8) is called TDHF equation.

2.1.2 Time-dependent Hartree-Fock-Bogoliubov theory (TDHFB)

We can derive the TDHFB equations with similar procedure for TDHF. First, we need to chose a quasi-particle vacuum $|\Phi(t)\rangle$ as many-body wave function. The quasi-particle operators $\beta_k^\dagger, \beta_k$ are usually defined as

$$\beta_k^\dagger \equiv \sum_\alpha U_{\alpha k} c_\alpha^\dagger + V_{\alpha k} c_k, \quad \beta_k = \sum_\alpha U_{\alpha k}^* c_\alpha + V_{\alpha k}^* c_k^\dagger, \tag{2.9}$$

$$|\Phi(t)\rangle \equiv \prod_k \beta_k^\dagger |0\rangle. \tag{2.10}$$

The vacuum of this quasi-particle state $|\Phi(t)\rangle$ is called Hartree-Fock-Bogoliubov (HFB) state. The replacement of many-body wave function to HFB state is HFB approximation. HFB state can deal with pairing tensor κ. TDHFB equations are derived from time-derivatives of ρ and κ. Eq.(2.5),(2.6) can be expanded in HFB state as

$$\begin{aligned}
i\hbar\frac{\partial}{\partial t}\rho_{ij} &= \sum_{\beta} t_{i\beta}\rho_{\beta j} - \sum_{\alpha} t_{\alpha j}\rho_{i\alpha} \\
&+ \frac{1}{2}\sum_{\beta,\mu,\nu} \bar{\mathcal{V}}_{i\beta\mu\nu}\big(\rho_{\nu\beta}\rho_{\mu j} - \rho_{\mu\beta}\rho_{\nu j} + \kappa^*_{j\beta}\kappa_{\mu\nu}\big) \\
&- \frac{1}{2}\sum_{\alpha,\beta,\mu} \bar{\mathcal{V}}_{\alpha\beta\mu j}\big(\rho_{i\beta}\rho_{\mu\alpha} - \rho_{i\alpha}\rho_{\mu\beta} + \kappa^*_{\alpha\beta}\kappa_{\mu i}\big), \qquad (2.11)
\end{aligned}$$

$$\begin{aligned}
i\hbar\frac{\partial}{\partial t}\kappa_{ij} &= \sum_{\beta} t_{i\beta}\kappa_{\beta j} - t_{j\beta}\kappa_{\beta i} + \frac{1}{2}\sum_{\mu,\nu} \bar{\mathcal{V}}_{ij\mu\nu}\kappa_{\mu\nu} \\
&+ \frac{1}{2}\sum_{\alpha,\mu,\nu} \bar{\mathcal{V}}_{\alpha i\mu\nu}\big(\rho_{j\alpha}\kappa_{\mu\nu} - \rho_{\nu\alpha}\kappa_{\mu j} + \rho_{\mu\alpha}\kappa_{\nu j}\big) \\
&- \frac{1}{2}\sum_{\alpha,\mu,\nu} \bar{\mathcal{V}}_{\alpha j\mu\nu}\big(\rho_{i\alpha}\kappa_{\mu\nu} - \rho_{\nu\alpha}\kappa_{\mu j} + \rho_{\mu\alpha}\kappa_{\nu i}\big). \qquad (2.12)
\end{aligned}$$

When we introduce $\Gamma_{\alpha\mu} = \sum_{\beta\nu} \bar{\mathcal{V}}_{\alpha\beta\mu\nu}\rho_{\nu\beta}$ and $\Delta_{\alpha\beta} \equiv \frac{1}{2}\sum_{\mu\nu} \bar{\mathcal{V}}_{\alpha\beta\mu\nu}\kappa_{\mu\nu}$ called pair potential, so Eq.(2.11) and (2.12) can be rewritten as

$$\begin{aligned}
i\hbar\frac{\partial}{\partial t}\rho_{ij} &= \sum_{\mu}\left\{(t_{i\mu}+\Gamma_{i\mu})\rho_{\mu j} - \rho_{i\mu}(t_{\mu j}+\Gamma_{\mu j}) + \Delta_{i\mu}\kappa^*_{j\mu} - \kappa_{\mu i}\Delta^*_{\mu j}\right\}, \\
i\hbar\frac{\partial}{\partial t}\kappa_{ij} &= \sum_{\mu}\left\{(t_{i\mu}+\Gamma_{i\mu})\kappa_{\mu j} - (t_{j\mu}+\Gamma_{j\mu})\kappa_{\mu i} - \Delta_{i\mu}\rho^*_{\mu j} - \rho_{i\mu}\Delta_{\mu j}\right\} + \Delta_{ij}.
\end{aligned}$$

We introduce $h = t + \Gamma$ to them, then we can get usual TDHFB equations as

$$i\hbar\frac{\partial}{\partial t}\rho = [h,\rho] + \kappa\Delta^* - \Delta\kappa^*, \qquad (2.13)$$

$$i\hbar\frac{\partial}{\partial t}\kappa = h\kappa + \kappa h^* + \Delta(1-\rho^*) - \rho\Delta. \qquad (2.14)$$

Properties of TDHFB

We show that TDHFB conserves expectation values of total number and total energy. Total number N and energy E can be written with using HFB many-body wave function $|\Phi\rangle$ as

$$N \equiv \langle\Phi|N|\Phi\rangle = \sum_i \langle\Phi|c_i^\dagger c_i|\Phi\rangle = \sum_i \rho_{ii} = \mathrm{Tr}\{\rho\}, \qquad (2.15)$$

$$E \equiv \langle\Phi|H|\Phi\rangle = \sum_{\alpha,\beta} h_{\alpha\beta}\rho_{\beta\alpha} - \frac{1}{2}\Gamma_{\alpha\beta}\rho_{\beta\alpha} - \frac{1}{2}\Delta^*_{\alpha\beta}\kappa_{\beta\alpha} = \mathrm{Tr}\left\{h\rho - \frac{1}{2}\Gamma\rho - \frac{1}{2}\Delta^*\kappa\right\}, \qquad (2.16)$$

where the notation Tr stands for taking the trace of the matrices and we assume the Hamiltonian H given as (2.2). We expand above values with the small time-variations of ρ and κ. These variations can be expressed TDHFB equations (2.13) and (2.14) as

$$\begin{aligned}\rho' &= \rho - i\eta([h,\rho] + \kappa\Delta^* - \Delta\kappa^*),\\ \kappa' &= \kappa - i\eta(h\kappa + \kappa h^* + \Delta(1-\rho^*) - \rho\Delta),\end{aligned}$$

where η is equivalent to value of $dt/\hbar$. Then, we can express time-variations δN as

$$\delta N = \mathrm{Tr}\{\rho' - \rho\} = -i\eta\mathrm{Tr}\{[h,\rho] + \kappa\Delta^* - \Delta\kappa^*\} = 0. \tag{2.17}$$

It is given by following relations,

$$\begin{aligned}[h,\rho]_{\alpha\beta} &= \sum_{\mu} h_{\alpha\mu}\rho_{\mu\beta} - \rho_{\alpha\mu}h_{\mu\beta} \to 0 \quad (\text{with } \delta_{\alpha\beta}),\\ \mathrm{Tr}\{\kappa\Delta^* - \Delta\kappa^*\} &= \sum_{\alpha,\beta} \delta_{\alpha\beta}(\kappa\Delta^* - \Delta\kappa^*)_{\alpha\beta}\\ &= \frac{1}{2}\sum_{\alpha,\mu,m,n} \kappa_{\alpha\mu}\bar{\mathcal{V}}_{\mu\alpha mn}\kappa^*_{mn} - \bar{\mathcal{V}}_{\alpha\mu mn}\kappa_{mn}\kappa^*_{\mu\alpha} = 0.\end{aligned}$$

And also we can express time-variation δE as

$$\begin{aligned}\delta E = &- i\eta\mathrm{Tr}\{h[h,\rho] + h\kappa\Delta^* - h\Delta\kappa^*\}\\ &- \frac{i\eta}{2}\mathrm{Tr}\left\{-\Delta^* h\kappa - \Delta^*\kappa h^* - \Delta^*\Delta + \Delta^*\Delta\rho^* + \Delta^*\rho\Delta\right\}\\ . &- \frac{i\eta}{2}\mathrm{Tr}\left\{\ h^*\kappa^*\Delta + \kappa^* h\Delta + \Delta^*\Delta - \Delta^*\rho\Delta - \rho^*\Delta^*\Delta\right\} = 0,\end{aligned}$$

where we use the relations $h^* = h^T, \kappa^T = -\kappa$ and $\Delta^T = -\Delta$ and the time-variation from $\Gamma\rho$ in Eq.(2.16) is zero because $\mathrm{Tr}\{[h,\rho]\} = 0$.

2.2 Canonical-basis formulation of time-dependent mean field theory

In this section, we derive the basic equations of Cb-TDHFB method. Using the time-dependent variational principle, the similar equations were derived by Błocki and Flocard [58]. However, it was not clear that what kind of approximation was introduced and how they are different from the full TDHFB. We present here a sufficient condition to reduce the TDHFB equations to those in a simple canonical form.

We start from the density-matrix equation of the TDHFB and find equations for the canonical-basis states and their occupation- and pair-probability factors. In order to clarify our heuristic strategy, let us start from a simpler case without the pairing correlation.

2.2.1 TDHF equation

The TDHF equation in the density-matrix formalism is written as Eq.(2.8) or [3]

$$i\frac{\partial}{\partial t}\rho(t) = [h(t), \rho(t)]\,,$$

where $\rho(t)$ and $h(t)$ are the one-body density operator and the single-particle (Hartree-Fock) Hamiltonian, respectively. We now express the one-body density using the time-dependent canonical single-particle basis, $\{|\phi_k(t)\rangle\}$, which are assumed to be orthonormal ($\langle\phi_k(t)|\phi_l(t)\rangle = \delta_{kl}$).

$$\rho(t) = \sum_{k=1}^{N} |\phi_k(t)\rangle\langle\phi_k(t)|, \tag{2.18}$$

where N is the total particle number. Substituting this into Eq.(2.8), we have

$$\sum_{k=1}^{N} \left\{ i|\dot{\phi}_k(t)\rangle\langle\phi_k(t)| + i|\phi_k(t)\rangle\langle\dot{\phi}_k(t)| \right\} = \sum_{k=1}^{N} \left\{ h(t)|\phi_k(t)\rangle\langle\phi_k(t)| - |\phi_k(t)\rangle\langle\phi_k(t)|h(t) \right\}. \tag{2.19}$$

the inner product with $|\phi_k(t)\rangle$ leads to

$$\hat{P}\left(i\frac{\partial}{\partial t} - h(t)\right)|\phi_k(t)\rangle = 0 \qquad k = 1, \cdots, N, \tag{2.20}$$

with $\hat{P} = 1 - \sum_{k=1}^{N} |\phi_k(t)\rangle\langle\phi_k(t)|$. Here, we used the conservation of the orthonormal property for the canonical states, $d/dt\langle\phi_k(t)|\phi_l(t)\rangle = 0$. This leads to the most general canonical-basis TDHF (Cb-TDHF) equations

$$i\frac{\partial}{\partial t}|\phi_k(t)\rangle = h(t)|\phi_k(t)\rangle - \sum_{l=1}^{N} |\phi_l(t)\rangle\eta_{lk}(t), \qquad k = 1, \cdots, N, \tag{2.21}$$

where the matrix $\eta_{lk}(t)$ is arbitrary but should be hermitian to conserve the orthonormal property. It is easy to see that the time evolution of the density does not depend on the choice of η_{lk}. This is related to the gauge invariance with respect to the unitary transformations among $|\phi_k(t)\rangle$ ($k = 1, \cdots, N$). The most common choice is $\eta_{lk} = 0$, which leads to the TDHF equation shown in most textbooks.

2.2.2 Canonical-basis TDHFB (Cb-TDHFB) equations

We now derive Cb-TDHFB equations starting from TDHFB equations Eq.(2.13) and (2.14) [1].

$$\begin{aligned} i\frac{\partial}{\partial t}\rho(t) &= [h(t), \rho(t)] + \kappa(t)\Delta^*(t) - \Delta(t)\kappa^*(t), \\ i\frac{\partial}{\partial t}\kappa(t) &= h(t)\kappa(t) + \kappa(t)h^*(t) + \Delta(t)(1-\rho^*(t)) - \rho(t)\Delta(t). \end{aligned}$$

At each instant of time, we may diagonalize the density operator $\hat{\rho}$ in the orthonormal canonical basis, $\{\phi_k(t), \phi_{\bar{k}}(t)\}$ with the occupation probabilities ρ_k. For the canonical states, we use the alphabetic indexes such as k for half of the total space indicated by $k > 0$. For each state with $k > 0$, there exists a "paired" state $\bar{k} < 0$ which is orthogonal to all the states with $k > 0$. The set of states $\{\phi_k, \phi_{\bar{k}}\}$ generate the whole single-particle space[2]. We use the Greek letters $\mu, \nu, \cdots$ for indexes of an adopted representation (complete set) for the single-particle states. The creation operator of particles at the state $|\phi_k(t)\rangle$ is expressed as $\hat{c}_k^\dagger(t) = \sum_\mu \langle\mu|\phi_k(t)\rangle\hat{c}_\mu^\dagger$, and the TDHFB state is expressed in the canonical (BCS) form as

$$|\Psi(t)\rangle = \prod_{k>0}\left\{u_k(t) + v_k(t)c_k^\dagger(t)c_{\bar{k}}^\dagger(t)\right\}|0\rangle. \tag{2.22}$$

For later purposes, it is convenient to introduce the following notations for two-particle states:

$$\begin{aligned} \langle\mu\nu|\phi_k(t)\phi_{\bar{k}}(t)\rangle &\equiv \langle\mu|\phi_k(t)\rangle\langle\nu|\phi_{\bar{k}}(t)\rangle, && (2.23) \\ \langle\langle\mu\nu|\phi_k(t)\phi_{\bar{k}}(t)\rangle\rangle &\equiv \langle\mu\nu|\phi_k(t)\phi_{\bar{k}}(t)\rangle - \langle\mu\nu|\phi_{\bar{k}}(t)\phi_k(t)\rangle, && (2.24) \end{aligned}$$

and for projection operator on a canonical pair of states $(k, \bar{k})$,

$$\hat{\pi}_k(t) \equiv |\phi_k(t)\rangle\langle\phi_k(t)| + |\phi_{\bar{k}}(t)\rangle\langle\phi_{\bar{k}}(t)|. \tag{2.25}$$

Then, it is easy to show the following properties $(k, l > 0)$:

$$\begin{aligned} \sum_{\mu\nu}\langle\mu\nu|\phi_k(t)\phi_{\bar{k}}(t)\rangle\langle\phi_l(t)\phi_{\bar{l}}(t)|\mu\nu\rangle &= \delta_{kl}, && (2.26) \\ \sum_{\mu\nu}\langle\langle\mu\nu|\phi_k(t)\phi_{\bar{k}}(t)\rangle\rangle\langle\langle\phi_l(t)\phi_{\bar{l}}(t)|\mu\nu\rangle\rangle &= 2\delta_{kl}, && (2.27) \\ \sum_{\sigma}\langle\langle\mu\sigma|\phi_k(t)\phi_{\bar{k}}(t)\rangle\rangle\langle\langle\phi_l(t)\phi_{\bar{l}}(t)|\nu\sigma\rangle\rangle &= \delta_{kl}\langle\mu|\hat{\pi}(t)_k|\nu\rangle, && (2.28) \\ \sum_{\sigma}\langle\langle\mu\sigma|\phi_k(t)\phi_{\bar{k}}(t)\rangle\rangle\langle\nu|\hat{\pi}_l|\sigma\rangle &= \delta_{kl}\langle\langle\mu\nu|\phi_k(t)\phi_{\bar{k}}(t)\rangle\rangle. && (2.29) \end{aligned}$$

---

[1] In some case, the TDHFB equation can be written in terms of the generalized density matrix [4] as

$$i\frac{\partial}{\partial t}R = [\mathcal{H}, R],$$

where

$$R \equiv \begin{pmatrix} \rho & \kappa \\ -\kappa^* & 1-\rho^* \end{pmatrix}, \qquad \mathcal{H} \equiv \begin{pmatrix} h & \Delta \\ -\Delta^* & -h^* \end{pmatrix}.$$

[2] In the case without pairing ($\Delta = 0$), the canonical pair becomes arbitrary as far as they have the same occupation probability ρ_k that is either 1 or 0.

Using these notations, the density and the pairing-tensor matrixes are given by

$$\begin{aligned}\rho_{\mu\nu}(t) &= \sum_{k>0} \rho_k(t)\langle\mu|\hat{\pi}_k(t)|\nu\rangle, & (2.30)\\ \kappa_{\mu\nu}(t) &= \sum_{k>0} \kappa_k(t)\langle\langle\mu\nu|\phi_k(t)\phi_{\bar{k}}(t)\rangle\rangle, & (2.31)\end{aligned}$$

where $\rho_k(t)$ and $\kappa_k(t)$ are occupation and pair probabilities, respectively. In terms of the BCS factors of (u,v) [3], they are given as $\rho_k(t)=|v_k(t)|^2$ and $\kappa_k(t)=u_{\bar{k}}^*(t)v_k(t)$. It should be noted that the canonical pair of states, $|\phi_k(t)\rangle$ and $|\phi_{\bar{k}}(t)\rangle$, are assumed to be orthonormal but not necessarily related with each other by the time reversal, $|\phi_{\bar{k}}\rangle \neq T|\phi_k\rangle$.

Thanks to the orthonormal property, we can invert Eqs.(2.30) and (2.31) for ρ_k and κ_k,

$$\begin{aligned}\rho_k(t) &= \sum_{\mu\nu}\langle\phi_k(t)|\mu\rangle\rho_{\mu\nu}(t)\langle\nu|\phi_k(t)\rangle = \sum_{\mu\nu}\langle\phi_{\bar{k}}(t)|\mu\rangle\rho_{\mu\nu}(t)\langle\nu|\phi_{\bar{k}}(t)\rangle, & (2.32)\\ \kappa_k(t) &= \sum_{\mu\nu}\langle\phi_k(t)\phi_{\bar{k}}(t)|\mu\nu\rangle\kappa_{\mu\nu}(t) = \frac{1}{2}\sum_{\mu\nu}\langle\langle\phi_k(t)\phi_{\bar{k}}(t)|\mu\nu\rangle\rangle\kappa_{\mu\nu}(t). & (2.33)\end{aligned}$$

With help of Eq.(2.30), the derivative of $\rho_k(t)$ with respect to time t leads to

$$\begin{aligned} i\frac{d}{dt}\rho_k(t) &= \sum_{\mu\nu}\langle\phi_k(t)|\mu\rangle i\frac{d\rho_{\mu\nu}}{dt}\langle\nu|\phi_k(t)\rangle + i\rho_k(t)\frac{d}{dt}\langle\phi_k(t)|\phi_k(t)\rangle\\ &= \sum_{\mu\nu}\langle\phi_k(t)|\mu\rangle i\frac{d\rho_{\mu\nu}}{dt}\langle\nu|\phi_k(t)\rangle\\ &= \sum_{\mu\nu}\left\{\kappa_k(t)\Delta_{\mu\nu}^*(t)\langle\nu\mu|\phi_k(t)\phi_{\bar{k}}(t)\rangle + \kappa_k^*(t)\Delta_{\mu\nu}(t)\langle\phi_k(t)\phi_{\bar{k}}(t)|\mu\nu\rangle\right\}. & (2.34)\end{aligned}$$

We used the assumption of norm conservation for the second equation, and used the TDHFB equation (2.13) in the last equation. Since the pair potential $\Delta_{\mu\nu}(t)$ is anti-symmetric, it is written in a simple form as

$$i\frac{d}{dt}\rho_k(t) = \kappa_k(t)\Delta_k^*(t) - \kappa_k^*(t)\Delta_k(t), \tag{2.35}$$

$$\Delta_k(t) \equiv -\sum_{\mu\nu}\Delta_{\mu\nu}(t)\langle\phi_k(t)\phi_{\bar{k}}(t)|\mu\nu\rangle = -\frac{1}{2}\sum_{\mu\nu}\Delta_{\mu\nu}(t)\langle\langle\phi_k(t)\phi_{\bar{k}}(t)|\mu\nu\rangle\rangle. \tag{2.36}$$

In case that the pair potential is computed from a two-body interaction v as $\Delta_{\mu\nu}(t)=\sum_{\alpha\beta}v_{\mu\nu,\alpha\beta}\kappa_{\alpha\beta}(t)$, the gap parameters, $\Delta_k(t)$, are identical to those of the BCS approximation [3].

$$\Delta_k(t) = -\sum_{l>0}\kappa_l(t)(v_{k\bar{k},l\bar{l}} - v_{k\bar{k},\bar{l}l}) \equiv -\sum_{l>0}\kappa_l(t)\bar{v}_{k\bar{k},l\bar{l}}. \tag{2.37}$$

It should be noted here that the two-body matrix elements $v_{k\bar{k},l\bar{l}}$ (and the anti-symmetric $\bar{v}_{k\bar{k},l\bar{l}}$) are time-dependent because the canonical basis, $(k,\bar{k})$ and $(l,\bar{l})$, are time-dependent.

In the same way, we evaluate the time derivative of $\kappa_k(t)$ as

$$i\frac{d}{dt}\kappa_k(t) = \sum_{\mu\nu} \langle \phi_k(t)\phi_{\bar{k}}(t)|\mu\nu\rangle i\frac{d\kappa_{\mu\nu}}{dt} + i\kappa_k(t)\left(\langle \frac{d\phi_k}{dt}|\phi_k(t)\rangle + \langle \frac{d\phi_{\bar{k}}}{dt}|\phi_{\bar{k}}(t)\rangle \right). \tag{2.38}$$

Then, using the TDHFB equation (2.14), we obtain

$$i\frac{d}{dt}\kappa_k(t) = \left(\eta_k(t) + \eta_{\bar{k}}(t)\right)\kappa_k(t) + \Delta_k(t)\left(2\rho_k(t) - 1\right), \tag{2.39}$$

where $\eta_k(t) \equiv \langle \phi_k(t)|h(t)|\phi_k(t)\rangle + i\langle \frac{\partial \phi_k}{\partial t}|\phi_k(t)\rangle$.

The time-dependent equations for $\rho_k(t)$ and $\kappa_k(t)$ are now given in rather simple forms as Eqs.(2.35) and (2.39). So far, their derivation is solely based on the TDHFB equations, utilizing the fact that $\rho_{\mu\nu}(t)$ and $\kappa_{\mu\nu}(t)$ can be expressed by the orthonormal canonical basis, $|\phi_k(t)\rangle$ and $|\phi_{\bar{k}}(t)\rangle$, and their occupation and pair probabilities, $\rho_k(t)$ and $\kappa_k(t)$. However, in general, the time evolution of the canonical basis is not given by a simple equation. Therefore, we now introduce an assumption (approximation) that the pair potential is written as

$$\Delta_{\mu\nu}(t) = -\sum_{k>0} \Delta_k(t)\langle\langle \mu\nu|\phi_k(t)\phi_{\bar{k}}(t)\rangle\rangle. \tag{2.40}$$

This satisfies Eq.(2.36), but in general, Eq.(2.36) can not be inverted because the two-particle states $|\phi_k\phi_{\bar{k}}\rangle$ do not span the whole space. In other words, we only take into account the pair potential of the "diagonal" parts in the canonical basis, $\Delta_{k\bar{l}} = -\Delta_k\delta_{kl}$. In the stationary limit ($|\phi_{\bar{k}}\rangle = T|\phi_k\rangle$), this is equivalent to the ordinary BCS approximation (see Sec. 2.3.3).

With the approximation of Eq.(2.40), it is easy to see that the TDHFB equations, (2.13) and (2.14), are consistent with the following equations:

$$i\frac{\partial}{\partial t}|\phi_k(t)\rangle = (h(t) - \eta_k(t))|\phi_k(t)\rangle, \qquad i\frac{\partial}{\partial t}|\phi_{\bar{k}}(t)\rangle = (h(t) - \eta_{\bar{k}}(t))|\phi_{\bar{k}}(t)\rangle. \tag{2.41}$$

In summary, the Cb-TDHFB equations consists of Eqs. (2.41), (2.35), and (2.39). To derive these equations from the TDHFB equations, we have assumed the diagonal property of the pair potential, Eq.(2.40).

2.3 Properties of the Cb-TDHFB equations

2.3.1 Gauge invariance

The $\eta_k(t)$ and $\eta_{\bar{k}}(t)$, in Eqs.(2.39) and (2.41), must be real to conserve the orthonormal property, however, they are arbitrary. This is related to the phase degrees of freedom of the canonical states. The Cb-TDHFB equations, (2.35), (2.39) and (2.41), are invariant with respect to the following gauge transformations with arbitrary real functions, $\theta_k(t)$ and $\theta_{\bar{k}}(t)$.

$$|\phi_k\rangle \rightarrow e^{i\theta_k(t)}|\phi_k\rangle \quad \text{and} \quad |\phi_{\bar{k}}\rangle \rightarrow e^{i\theta_{\bar{k}}(t)}|\phi_{\bar{k}}\rangle \tag{2.42}$$

$$\kappa_k \rightarrow e^{-i(\theta_k(t)+\theta_{\bar{k}}(t))}\kappa_k \quad \text{and} \quad \Delta_k \rightarrow e^{-i(\theta_k(t)+\theta_{\bar{k}}(t))}\Delta_k \tag{2.43}$$

simultaneously with

$$\eta_k(t) \to \eta_k(t) + \frac{d\theta_k}{dt} \quad \text{and} \quad \eta_{\bar{k}}(t) \to \eta_{\bar{k}}(t) + \frac{d\theta_{\bar{k}}}{dt}.$$

The phase relations of Eq.(2.43) are obtained from Eqs.(2.33) and (2.36).

2.3.2 Conservation laws

Orthonormality of canonical states

Apparently, Eq.(2.41) conserves the orthonormal property of canonical states, as far as η_k are real.

$$i\frac{\partial}{\partial t}\langle\phi_k(t)|\phi_l(t)\rangle = \langle\phi_k(t)|\{(h(t)-\eta_l(t)) - (h^\dagger(t)-\eta_k(t))\}|\phi_l(t)\rangle = 0. \tag{2.44}$$

Here, we assume $\langle\phi_k(t)|\phi_l(t)\rangle = \delta_{kl}$ at time t.

Average particle number

The average particle number also conserves because

$$i\frac{d}{dt}N(t) = 2i\frac{d}{dt}\sum_{k>0}\rho_k(t) = 2\sum_{k>0}(\kappa_k(t)\Delta_k^*(t) - \kappa_k^*(t)\Delta_k(t)) = 0, \tag{2.45}$$

where we used the expression of the pairing energy, Eq.(2.71), for the last equation.

Average total energy

Time variation of the energy functional $E[\rho,\kappa]$ can be divided into two: $dE/dt = dE/dt|_\rho + dE/dt|_\kappa$. The variation of energy associated with the normal-density fluctuation is

$$i\left.\frac{dE}{dt}\right|_\rho = i\sum_{\mu\nu}\frac{\partial E}{\partial\rho_{\mu\nu}}\frac{d\rho_{\mu\nu}}{dt} = i\sum_{k>0}\frac{d\rho_k}{dt}(\epsilon_k(t)+\epsilon_{\bar{k}}(t)), \tag{2.46}$$

where $\epsilon_k(t) = \langle\phi_k(t)|h(t)|\phi_k(t)\rangle$. This equation has an intuitive physical interpretation. The energy carried by a canonical state $|\phi_k\rangle$ is $\epsilon_k(t)\times\rho_k$. If the occupation probability is fixed during the time evolution, the right-hand side of Eq.(2.46) vanishes. This corresponds to the cases such as the TDHF and its extension with fixed BCS occupation probabilities. In the TDHFB, the energy variation in Eq.(2.46) transfers from/to the pairing energy. In fact, time variation due to the pairing tensors-produce fluctuation produces

$$i\left.\frac{dE}{dt}\right|_\kappa = i\frac{1}{2}\sum_{\mu\nu}\left(\frac{\partial E}{\partial\kappa_{\mu\nu}}\frac{d\kappa_{\mu\nu}}{dt} + \frac{\partial E}{\partial\kappa_{\mu\nu}^*}\frac{d\kappa_{\mu\nu}^*}{dt}\right) = \sum_{k>0}(\kappa_k^*\Delta_k - \kappa_k\Delta_k^*)(\epsilon_k(t)+\epsilon_{\bar{k}}(t)), \tag{2.47}$$

where Eq.(2.40) is used. Because of Eq.(2.35), two contributions of Eqs.(2.46) and (2.47) always cancel and the total energy is conserved. This is natural because the Cb-TDHFB equations satisfy the TDHFB equations, (2.13) and (2.14), for which the conservation of the total energy in TDHFB is well known [4].

2.3.3 Stationary solution

When we assume that all the canonical states are eigenstates of the time-independent single-particle Hamiltonian h_0.

$$|\phi_k(t)\rangle = |\phi_k^0\rangle e^{i\theta_k(t)}, \quad |\phi_{\bar{k}}(t)\rangle = |\phi_{\bar{k}}^0\rangle e^{i\theta_{\bar{k}}(t)}, \tag{2.48}$$

$$h_0|\phi_k^0\rangle = \epsilon_k^0|\phi_k^0\rangle, \quad h_0|\phi_{\bar{k}}^0\rangle = \epsilon_k^0|\phi_{\bar{k}}^0\rangle, \tag{2.49}$$

where $|\phi_{\bar{k}}\rangle = T|\phi_k\rangle$ have the same eigenvalues ϵ_k^0 as $|\phi_k\rangle$. Here, $d\theta_k/dt = i\langle\partial\phi_k/\partial t|\phi_k\rangle$ and $d\theta_{\bar{k}}/dt = i\langle\partial\phi_{\bar{k}}/\partial t|\phi_{\bar{k}}\rangle$ are arbitrary real functions of t. $\kappa_k(t)$ and $\Delta_k(t)$ should have a common time-dependent phase associated with the chemical potential λ as $e^{-2i\lambda t}$. In addition to this, according to their definition, Eqs.(2.33) and (2.36), they have the following additional phases connected with the phases of the canonical states.

$$\kappa_k(t) = \kappa_k^0 \exp\{-i(2\lambda t + \theta_k(t) + \theta_{\bar{k}}(t))\}, \tag{2.50}$$

$$\Delta_k(t) = \Delta_k^0 \exp\{-i(2\lambda t + \theta_k(t) + \theta_{\bar{k}}(t))\}, \tag{2.51}$$

The stationary case of Eq.(2.35), $d\rho_k^0/dt = 0$, indicates that κ_k^0 and Δ_k^0 have the same arguments to make $\kappa_k(t)\Delta_k^*(t)$ real. If all the pairing matrix elements are real, we can choose both κ_k^0 and Δ_k^0 are real. Then, Eq.(2.39) reduces to

$$2(\epsilon_k^0 - \lambda)\kappa_k^0 + \Delta_k^0(2\rho_k^0 - 1) = 0. \tag{2.52}$$

This is consistent with the ordinary BCS result[3].

$$\rho_k^0 = \frac{1}{2}\left(1 - \frac{\epsilon_k^0 - \lambda}{\sqrt{(\epsilon_k^0 - \lambda)^2 + (\Delta_k^0)^2}}\right), \tag{2.53}$$

$$\kappa_k^0 = \frac{1}{2}\frac{\Delta_k^0}{\sqrt{(\epsilon_k^0 - \lambda)^2 + (\Delta_k^0)^2}}. \tag{2.54}$$

2.3.4 Small amplitude limit and the Nambu-Goldstone modes

It is known that the small-amplitude approximation for the TDHFB around the HFB ground state is identical to the QRPA. In the QRPA, when the ground state (HFB state) breaks continuous symmetry of the Hamiltonian, the Nambu-Goldstone modes appear as the zero-energy modes. In this section, we show that this is also true for the small-amplitude limit of the Cb-TDHFB.

The ground state is given by $|\phi_k^0\rangle$, $|\phi_{\bar{k}}^0\rangle$, κ_k^0, and ρ_k^0 which satisfy Eqs.(2.49) and (2.52). Extracting trivial phase factors, $\xi_k(t) \equiv \int_0^t \left\{\eta_k(t') - \epsilon_k^0\right\} dt'$, we express the time-dependent quantities as follows:

$$|\phi_k(t)\rangle = \left\{|\phi_k^0\rangle + |\delta\phi_k(t)\rangle\right\} e^{i\xi_k(t)}, \; |\phi_{\bar{k}}(t)\rangle = \left\{|\phi_{\bar{k}}^0\rangle + |\delta\phi_{\bar{k}}(t)\rangle\right\} e^{i\xi_{\bar{k}}(t)}, \tag{2.55}$$

$$\kappa_k(t) = \left\{\kappa_k^0 + \delta\kappa_k(t)\right\} e^{-i\{\xi_k(t)+\xi_{\bar{k}}(t)+2\lambda t\}}, \; \Delta_k(t) = \left\{\Delta_k^0 + \delta\Delta_k(t)\right\} e^{-i\{\xi_k(t)+\xi_{\bar{k}}(t)+2\lambda t\}}, \tag{2.56}$$

$$\rho_k(t) = \rho_k^0 + \delta\rho_k(t), \; h(t) = h_0 + \delta h(t), \tag{2.57}$$

---

[3] BCS equation is given in Appendix.C

Substituting these into Eqs.(2.41), (2.35), and (2.39), they lead to the following equations in the linear order with respect to the fluctuation.

$$\begin{aligned}
i\frac{\partial}{\partial t}|\delta\phi_k(t)\rangle &= (h_0-\epsilon_k^0)|\delta\phi_k(t)\rangle + \delta h(t)|\phi_k^0\rangle, \quad (k\leftrightarrow\bar{k}), && (2.58)\\
i\frac{\partial}{\partial t}\delta\rho_k(t) &= \Delta_k^{0*}\delta\kappa_k(t) + \kappa_k^0\delta\Delta_k^*(t) - \text{ c.c.}, && (2.59)\\
i\frac{\partial}{\partial t}\delta\kappa_k(t) &= 2(\epsilon_k^0-\lambda)\delta\kappa_k(t) + (2\rho_k^0-1)\delta\Delta_k(t) + 2\Delta_k^0\delta\rho_k(t). && (2.60)
\end{aligned}$$

When these fluctuating parts have specific oscillating frequency ω, they correspond to the normal modes. The zero-energy modes correspond to stationary normal-mode solutions with $\omega = 0$.

Translation and rotation

When the HFB ground state spontaneously violates the translational (rotational) symmetry, there are generators, $\vec{P}$ ($\vec{J}$), which transform the ground state into a new state but keep the energy invariant. Here, let us denote one of those hermitian generators, S. The transformation with respect to the generator S with real parameter α leads to

$$\begin{aligned}
|\phi_k^0\rangle &\rightarrow |\phi_k^0(\alpha)\rangle = e^{i\alpha S}|\phi_k^0\rangle \quad (k\leftrightarrow\bar{k}), && (2.61)\\
h_0 &\rightarrow h_0(\alpha) = e^{i\alpha S}h_0e^{-i\alpha S}, && (2.62)
\end{aligned}$$

with $\rho_k(\alpha)=\rho_k^0$, $\kappa_k(\alpha)=\kappa_k^0$, $\epsilon_k(\alpha)=\epsilon_k^0$, and $\Delta_k(\alpha)=\Delta_k^0$. These transformed quantities should also satisfy Eq.(2.49).

$$(h_0(\alpha)-\epsilon_k^0)|\phi_k^0(\alpha)\rangle = 0. \tag{2.63}$$

In the linear order with respect to the parameter α, we have

$$i\alpha(h_0-\epsilon_k^0)S|\phi_k^0\rangle + i\alpha[S,h_0]|\phi_k^0\rangle = 0. \tag{2.64}$$

Equation (2.64) means that $|\delta\phi_k^S\rangle \equiv i\alpha S|\phi_k^0\rangle$ and $\delta h_S \equiv i\alpha[S,h_0]$ correspond to a normal-mode solution with $\omega = 0$ for Eq.(2.58). $\delta\rho_k^S = 0$, $\delta\kappa_k^S = 0$, and $\delta\Delta_k^S = 0$ also satisfy Eqs.(2.59) and (2.60). Therefore, the Nambu-Goldstone modes related to the spontaneous breaking of the translational and rotational symmetries become zero-energy modes in the small-amplitude Cb-TDHFB equations.

Pairing rotation

When the ground state is in the superfluid phase, we have $\kappa_k^0 \neq 0$ at least for a certain k. The ground state can be transformed into a new state by operation of $e^{i\theta N}$ where N is the number operator. This transformation changes the phase of κ_k and Δ_k but keeps the other quantities invariant.

$$\begin{aligned}
\delta\kappa_k^N &= e^{2i\theta}\kappa_k^0-\kappa_k^0 \approx 2i\theta\kappa_k^0, \quad \delta\Delta_k^N = e^{2i\theta}\Delta_k^0-\Delta_k^0 \approx 2i\theta\Delta_k^0, && (2.65)\\
\delta\rho_k^N &= \delta h_N = 0, \quad |\delta\phi_k^N\rangle = |\delta\phi_{\bar{k}}^N\rangle = 0. && (2.66)
\end{aligned}$$

Using Eq.(2.52), it is easy to see that these quantities correspond to an $\omega = 0$ solution of Eqs.(2.58), (2.59), and (2.60). Thus, the pairing rotational modes appear as the zero energy modes as well.

Particle-particle (hole-hole) RPA

The Cb-TDHFB equation (2.58) seems to be independent from the rest of equations, (2.59) and (2.60), at first sight. However, this is not true in general, because $\delta\Delta_k(t)$ depend on $|\delta\phi_k(t)\rangle$ and $\delta h(t)$ depends on $\delta\rho_k(t)$. In contrast, when the ground state is in the normal phase ($\kappa_k^0 = \Delta_k^0 = 0$), $\delta\Delta_k(t)$ becomes independent from $|\delta\phi_l(t)\rangle$, and we have $\delta\rho_k(t) = 0$. This means that the particle-hole (p-h) channel is exactly decoupled from the particle-particle (p-p) and hole-hole (h-h) channels. It is well-known that TDHF equations in the small-amplitude limit, (2.58), reduce to the RPA equation in the ph-channel [3, 4, 59]. Thus, we here discuss properties of the p-p and h-h channels.

The p-p and h-h dynamics are described by the following equations.

$$i\frac{\partial}{\partial t}\delta\kappa_k(t) = 2\epsilon_k^0\delta\kappa_k(t) \pm \delta\Delta_k(t), \tag{2.67}$$

where the sign $+$ $(-)$ is for hole (particle) orbitals, and we omit the chemical potential λ. For the p-p channel ($\omega = E_{N+2} - E_N$), a normal mode with frequency ω is described by $\delta\kappa_p = X_p e^{-i\omega t}$ for particle orbitals ($|p| > N/2$) and $\delta\kappa_h = -Y_h e^{-i\omega t}$ for hole orbitals ($|h| \leq N/2$). For the h-h channel ($\omega = E_{N-2} - E_N$), it is described by $\delta\kappa_h = X_h e^{-i\omega t}$ for hole orbitals ($|h| \leq N/2$) and $\delta\kappa_p = -Y_p e^{-i\omega t}$ for particle orbitals ($|k| > N/2$). Equation (2.67) can be rewritten in a matrix form as

$$\begin{pmatrix} 2\epsilon_p^0\delta_{pp'} + \bar{v}_{p\bar{p}p'\bar{p}'} & -\bar{v}_{p\bar{p}h'\bar{h}'} \\ -\bar{v}_{h\bar{h}p'\bar{p}'} & -2\epsilon_h^0\delta_{hh'} + \bar{v}_{h\bar{h}h'\bar{h}'} \end{pmatrix} \begin{pmatrix} Z_{p'} \\ Z_{h'} \end{pmatrix} = \omega \begin{pmatrix} 1 & 0 \\ 0 & -1 \end{pmatrix} \begin{pmatrix} Z_p \\ Z_h \end{pmatrix}, \tag{2.68}$$

where $Z_p = X_p$ $(Z_p = Y_p)$ and $Z_h = Y_h$ $(Z_h = X_h)$ for the p-p (h-h) channel. This is equivalent to the p-p and h-h RPA in the BCS approximation [3].

2.4 Cb-TDHFB equations with a simple pairing energy functional and gauge condition

2.4.1 Pairing energy functional

Normally, the pairing energy functional is bi-linear with respect to $\kappa_{\mu\nu}$ and $\kappa_{\mu\nu}^*$. For instance, when it is calculated from the two-body interaction, it is given by

$$E_\kappa(t) = \sum_{\mu,\nu,\rho,\sigma} v_{\mu\nu,\rho\sigma}\kappa_{\mu\nu}^*(t)\kappa_{\rho\sigma}(t). \tag{2.69}$$

Thus, the pairing energy can be also written as

$$\begin{aligned} E_\kappa(t) &= \frac{1}{2}\sum_{\mu\nu}\kappa_{\mu\nu}(t)\Delta_{\mu\nu}^*(t) = \frac{1}{2}\sum_{\mu\nu}\kappa_{\mu\nu}^*(t)\Delta_{\mu\nu}(t) && (2.70) \\ &= -\sum_{k>0}\kappa_k(t)\Delta_k^*(t) = -\sum_{k>0}\kappa_k^*(t)\Delta_k(t). && (2.71) \end{aligned}$$

For numerical calculations in the present study, we adopt a schematic pairing functional in a form of

$$E_g(t) = -\sum_{k,l>0} G_{kl}\kappa_k^*(t)\kappa_l(t), = -\sum_{k>0}\kappa_k^*(t)\Delta_k(t), \quad \Delta_k(t) = \sum_{l>0} G_{kl}\kappa_l(t), \tag{2.72}$$

where G_{kl} is a hermitian matrix. This pairing functional produces a pair potential which is diagonal in the canonical basis. This is consistent with the approximation of Eq. (2.40). However, the functional violates the gauge invariance (2.43), because

$$\sum_{l>0} G_{kl} e^{-i\theta_l + \theta_{\bar{l}}}\kappa_l(t) \neq e^{-i\theta_k + \theta_{\bar{k}}}\sum_{k>0} G_{kl}\kappa_l(t). \tag{2.73}$$

The violation comes from the fact that the $\Delta_k(t)$ in this schematic definition no longer hold the correct phase relation to canonical states $(k, \bar{k})$, according to the definition of Eq.(2.36). Therefore, we require the gauge condition of $\langle \frac{\partial \phi_k}{\partial t}|\phi_k\rangle = \langle \frac{\partial \phi_{\bar{k}}}{\partial t}|\phi_{\bar{k}}\rangle = 0$, so as to minimize the phase change of canonical states. This means that we choose the gauge parameters $\eta_k(t)$ as

$$\eta_k(t) = \epsilon_k(t) = \langle \phi_k(t)|h(t)|\phi_k(t)\rangle, \quad \eta_{\bar{k}}(t) = \epsilon_{\bar{k}}(t) = \langle \phi_{\bar{k}}(t)|h(t)|\phi_{\bar{k}}(t)\rangle. \tag{2.74}$$

2.4.2 Properties of Cb-TDHFB equations with E_g

The Cb-TDHFB equations with the simple pairing functional (2.72) keep the following desired properties, if we adopt the special gauge condition (2.74).

1. Conservation law
   - (a) Conservation of orthonormal property of the canonical states
   - (b) Conservation of average particle number
   - (c) Conservation of average total energy
2. The stationary solution corresponds to the HF+BCS solution.
3. Small-amplitude limit
   - (a) The Nambu-Goldstone modes are zero-energy normal-mode solutions.
   - (b) If the ground state is in the normal phase, the equations are identical to the particle-hole, particle-particle, and hole-hole RPA with the BCS approximation.

Among these properties, 1(a) and 1(b) do not depend on the choice of the gauge, however, the other properties are guaranteed only with the special choice of gauge (2.74).

Chapter 3

Application of Cb-TDHFB to linear-response calculations

3.1 Determination of the pairing strength g

In numerical calculations, we start from the HF+BCS calculation for the ground state. The pairing energy is calculated for the constant monopole pairing interaction with a smooth truncation for the model space. We follow the prescription given by Tajima *et al.* [60], which is equivalent to the following choice of G_{kl} of Eq.(2.72).

$$G_{kl} = g f(\epsilon_k^0) f(\epsilon_l^0), \tag{3.1}$$

with a constant real parameter g. The cut-off function $f(\varepsilon)$, which depends on the ground-state single-particle energies, is in the following form

$$f(\varepsilon) = \left(1 + \exp\left[\frac{\varepsilon - \epsilon_{\mathrm{c}}}{0.5\ \mathrm{MeV}}\right]\right)^{-1/2} \theta(e_{\mathrm{c}} - \varepsilon), \tag{3.2}$$

with the cut-off energies

$$\epsilon_{\mathrm{c}} = \tilde{\lambda} + 5.0\ \mathrm{MeV}, \quad e_{\mathrm{c}} = \epsilon_{\mathrm{c}} + 2.3\ \mathrm{MeV}, \tag{3.3}$$

where $\tilde{\lambda}$ is the average of the highest occupied level and the lowest unoccupied level in the HF state. Here, the cut-off parameter e_{c} is necessary to prevent occupation of spatially unlocalized single-particle states, known as the problem of unphysical gas near the drip line. For neutrons, if e_{c} becomes positive, we replace it by zero.

To determine the pairing strength constant g for each nuclei, we again follow the prescription of Ref.[60] which is practically identical to the one in Ref.[61]. The pairing strength constant g in this thesis is determined in order to treat a wide range of nuclei. For this purpose, the determination of pairing strength g is introduced the continuous spectrum approximation. So, we solve the following particle-number and gap equation expressed with level density $\bar{D}(\varepsilon)$,

$$N_\tau = \int_{-\infty}^{\infty} d\varepsilon \, \frac{(\varepsilon - \bar{\lambda}_\tau)^2 \bar{D}_\tau(\varepsilon)}{\sqrt{(\varepsilon - \bar{\lambda}_\tau)^2 + f^2(\varepsilon)\bar{\Delta}^2}} \ , \tag{3.4}$$

$$\bar{\Delta} = \frac{g_\tau}{2} \bar{\Delta} \int_{-\infty}^{\infty} d\varepsilon \, \frac{f^2(\varepsilon) \bar{D}_\tau(\varepsilon)}{\sqrt{(\varepsilon - \bar{\lambda}_\tau)^2 + f^2(\varepsilon)\bar{\Delta}^2}} \ , \tag{3.5}$$

where $\bar{D}_\tau(\varepsilon)$ is single-particle level density obtained in the Thomas-Fermi approximation and index τ means neutron and proton system. $\bar{D}_\tau(\varepsilon)$ forms

$$\bar{D}_\tau(\varepsilon) = \frac{1}{2\pi^2} \int dr \left(\frac{2m^*_\tau(r)}{\hbar^2} \right)^{3/2} (\varepsilon - V_\tau(r))^{1/2} \Theta(\varepsilon - V_\tau), \tag{3.6}$$

where m^*_τ is effective mass and V_τ means the central potential of ph-part. Eq.(3.4) determines the Fermi level $\bar{\lambda}_\tau$ for the density of state $\bar{D}_\tau$, while Eq.(3.5) decide the strength g_τ with the empirical formula for pairing gap $\bar{\Delta} = 12A^{-1/2}$MeV in each nucleon system. For light nuclei($A < 50$), and when the calculated value exceeds 0.6 MeV, we replace g_τ with 0.6 MeV because the resulting g_τ becomes apparently too strong. This value also obey the Ref.[60]. The pairing force strengths G_{kl} are calculated for the ground state and kept constant during the time evolution. We define the state-independent pairing gap as follows:

$$\Delta(t) \equiv g \sum_{k>0} \kappa_k(t) f(\epsilon^0_k). \tag{3.7}$$

The gap parameter for each canonical pair of states, k and $\bar{k}$, can be written as $\Delta_k(t) = \Delta(t) f(\epsilon^0_k)$.

3.2 Linear-response calculation in real-time

The canonical states in the ground state define the initial state for time evolution. In order to study the linear response, we use an weak instantaneous external field of $V_{\text{ext}}(\vec{r}, t) = -\eta F(\vec{r})\delta(t)$ to start the time evolution. Here, $F(\vec{r})$ is a one-body field, such as $E1$ operator with recoil charges,

$$F_i(\vec{r}) = \begin{cases} (Ne/A) r_i & \text{for protons} \\ -(Ze/A) r_i & \text{for neutrons} \end{cases} , \tag{3.8}$$

where $i = (x, y, z)$. We also study the isoscalar quadrupole (Q_{2K}) response with

$$F(\vec{r}) = Q_{2K} = \frac{1}{\sqrt{2(1+\delta_{K0})}} \left\{ r^2 Y_{2K}(\hat{\mathbf{r}}) + r^2 Y_{2-K}(\hat{\mathbf{r}}) \right\}, \quad K = 0 \text{ and } 2, \tag{3.9}$$

where Q_{20} and Q_{22} modes are sometimes called β- and γ-vibration in low-energy part. Then, at time $t = 0+$, the canonical states are given by

$$\phi_k(\vec{r}, \sigma; t = 0+) = e^{i\eta F(\vec{r})} \phi^0_k(\vec{r}, \sigma), \quad \phi_{\bar{k}}(\vec{r}, \sigma; t = 0+) = e^{i\eta F(\vec{r})} \phi^0_{\bar{k}}(\vec{r}, \sigma), \tag{3.10}$$

and the BCS factors by

$$\rho_k(t=0+) = \rho_k^0, \quad \kappa_k(t=0+) = \kappa_k^0. \tag{3.11}$$

The parameter η controls the strength of the external field. In this paper, since we calculate the linear response, it should be small enough to validate the linearity.

The strength function with respect to the operator F is calculated with the followings. We set $|\Phi_0\rangle, |\Phi_n\rangle$ as a many-body ground state and excited state which are assumed eigenstate of a Hamiltonian H. If we add an external field which is weak enough to regard as perturbation to $|\Phi_0\rangle$ at $t = 0+$, we can expand $|\Phi_0\rangle$ with $|\Phi_n\rangle$ as like,

$$|\Phi(0+)\rangle \equiv e^{i\eta F}|\Phi_0\rangle \simeq |\Phi_0\rangle + i\eta\sum_n |\Phi_n\rangle\langle\Phi_n|F|\Phi_0\rangle.$$

And, we can consider a time-evolution of many-body state $|\Phi(t)\rangle$ from $|\Phi(0+)\rangle$ with H,

$$|\Phi(t)\rangle = e^{-iHt}|\Phi(0_+)\rangle = e^{-iE_0t}|\Phi_0\rangle + i\eta\sum_n e^{-iE_nt}|\Phi_n\rangle\langle\Phi_n|F|\Phi_0\rangle,$$

where E_0, E_n are eigenvalue of H. Next, we can calculate the time-dependent expectation value$f(t)$ with F and $|\Phi(t)\rangle$ as,

$$f(t) = \langle\Phi(t)|F|\Phi(t)\rangle = f(0) + i\eta\sum_n |\langle\Phi_n|F|\Phi_0\rangle|^2\Big(e^{-i\tilde{E}_nt} - e^{i\tilde{E}_nt}\Big),$$

where $\tilde{E}_n = E_n - E_0$. Then, we get $f(E)$ in the energy representation through the Fourier transformation with a smoothing parameter $\Gamma/2$,

$$\begin{aligned} f(E) &= \int_0^\infty dt\ e^{(iE-\Gamma/2)t}(f(t) - f(0)) \\ &= i\eta\sum_n |\langle\Phi_n|F|\Phi_0\rangle|^2\Big(\frac{i}{\tilde{E}_n - E - i\Gamma/2} + \frac{i}{\tilde{E}_n + E + i\Gamma/2}\Big), \end{aligned}$$

where $\Gamma/2$ needs for this integration in general. In a limit of $\Gamma = 0$, the relation between $f(E)$ and the strength function of F can be describe with using Cauchy principal value $\mathcal{P}$,

$$\lim_{\Gamma\to 0} f(E) = -\eta\sum_n |\langle\Phi_n|F|\Phi_0\rangle|^2 \left\{\frac{\mathcal{P}}{\tilde{E}_n - E} + \frac{\mathcal{P}}{\tilde{E}_n + E} + i\pi\big(\delta(\tilde{E}_n - E) - \delta(\tilde{E}_n + E)\big)\right\} \tag{3.12}$$

Finally, we can get a formula of the strength function with respect to the operator F [24].

$$S(E;F) \equiv \sum_n |\langle\Phi_n|F|\Phi_0\rangle|^2\delta(E - \tilde{E}_n) = -\frac{1}{\pi\eta}\mathrm{Im}f(E), \quad \tilde{E}_n > 0\ , \tag{3.13}$$

In practical, we have introduced a smoothing parameter Γ which is set to 1 MeV throughout the calculations in Sec.4.1, 4.3, 4.6. The formula can be obtained from the time-dependent perturbation theory in the first order with respect to η [24]. Note that the strength function $S(E;F)$ is independent from magnitude of the parameter η as far as the linear approximation is

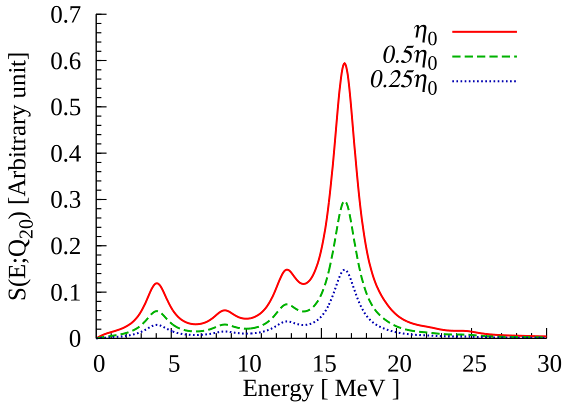

Figure 3.1: The isoscalar quadrupole strength distributions for prolate deformed nucleus ^{20}Ne with using Cb-TDHFB in BKN interaction. Solid line shows the result in η_0, dashed line shows the result in a half of η_0 and dotted line shows the result in a quarter of η_0. The smoothing parameter of $\Gamma = 1$ MeV is used.

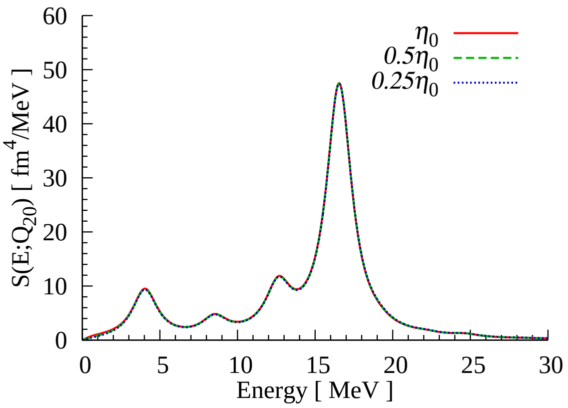

Figure 3.2: Same as Fig. 3.1 but they are normalized with respect to the amplitude η_0. The smoothing parameter of $\Gamma = 1$ MeV is used.

valid. Figure 3.1 and 3.2 show examples of the strength function when the linear approximation is valid. Figure 3.1 shows the results of Q_{20} vibration of ^{20}Ne in BKN interaction[1] given in Ref.[13, 15]. Lines in figure 3.1 correspond with results of several η, solid line shows the result in η_0, dashed line shows the result in a half of η_0 and dotted line shows the result in a quarter of η_0. They have not been normalized with the amplitude η_0. Figure 3.2 shows the normalized results. We can see that they give same results with valid amplitude. In the present study, we adopt the value of $\eta = 10^{-4}$ fm^{-1} for the $E1$ operator, and $\eta = 10^{-3}$ fm^{-2} for the quadrupole operator.

3.3 Details of numerical calculations

3.3.1 Three-dimensional coordinate space representation

We use the Cartesian coordinate-space representation for the canonical states, $\phi_k(\vec{r}, \sigma; t) = \langle \vec{r}, \sigma | \phi_k(t) \rangle$ with $\sigma = \pm 1/2$. In this present study, the three-dimensional (3D) coordinate space is discretized in square mesh of $\Delta x = \Delta y = \Delta z = 0.8$ fm in a sphere with radius of 12 fm when the mass number of nucleus is less than 70, in the case of over 70 mass number, the 3D coordinate space has the mesh of $\Delta x = \Delta y = \Delta z = 1.0$ fm in a sphere with radius of 15 fm. Thus, each canonical state is represented by $\phi_k(i, j, k, \sigma; t)$ with three discrete indexes for the 3D space.

---

[1] The effective interaction of Bonche, Koonin and Negele (BKN) had been originally proposed for analyzing the dynamics of spin and isospin saturated nuclei. This effective interaction is compose of δ-type two-body and three-body terms, but it does not have spin-orbit interaction. So, BKN interaction is sometimes called simplified Skyrme interaction.

3.3.2 Calculation for ground state

First, we need to obtain a static solution to construct an initial state for the time-dependent calculation. The numerical procedure is as follows:

1. Solve Eq.(2.49) for occupied canonical states ($|k| \leq N/2$) with $\rho_k = 1$, and construct the HF Hamiltonian $h_0[\rho]$, using the imaginary-time method [62] (See Appendix B for more detail).

2. Calculate unoccupied canonical states $\phi_k^0(\vec{r}, \sigma)$ ($|k| > N/2$) below the energy cut-off $e_{\rm c}$, using the imaginary-time method with h_0.

3. Solve the BCS equations [3] to obtain ρ_k and κ_k (See Appendix C B for more detail).

4. Update $h_0[\rho]$ with new ρ_k, then solve Eq.(2.49) again with the imaginary-time method, to calculate canonical states with $\epsilon_k^0 < e_{\rm c}$.

5. Back to 3. and repeat until convergence.

To solve Eq.(2.49), the imaginary-time-evolution operator for a small time interval Δt is repeatedly operated on each single-particle wave function. After each evolution, the single-particle wave functions are orthonormalized with the Gram-Schmidt method from low- to high-energy states. We add the constraints for the center of mass, $\int \vec{r}\rho(\vec{r}) = 0$, and the principal axis, $\int r_i r_j \rho(\vec{r}) = 0$ ($i \neq j$) for deformed nuclei (See Appendix B for more detail).

3.3.3 Energy density functional

In the present calculations, we adopt a Skyrme energy functional, $E_{\rm Sky}[\rho]$, with the parameter set of SkM* [63] which can reproduce experimental data of ground-state radii and multipole moments. The functional contains both time-even and time-odd densities same as Ref.[64]. The form of this energy density functional is,

$$\begin{aligned}
E_{\rm Sky}[\rho] &= \int d\vec{r}\; \mathcal{H}(\vec{r}), \\
\mathcal{H}(\boldsymbol{r}) &= \frac{\hbar^2}{2m}\tau + B_1\rho^2 + B_2(\rho_n^2 + \rho_p^2) + B_3(\rho\tau - \boldsymbol{j}^2) + B_4(\rho_n\tau_n - \boldsymbol{j}_n^2 + \rho_p\tau_p - \boldsymbol{j}_p^2) \\
&\quad + B_5\rho\nabla^2\rho + B_6(\rho_n\nabla^2\rho_n + \rho_p\nabla^2\rho_p) + B_7\rho^{2+\alpha} + B_8\rho^\alpha(\rho_n^2 + \rho_p^2) \\
&\quad + B_9(\rho\boldsymbol{\nabla}\cdot\boldsymbol{J} + \boldsymbol{j}\cdot\boldsymbol{\nabla}\times\boldsymbol{\rho} + \rho_n\boldsymbol{\nabla}\cdot\boldsymbol{J}_n + \boldsymbol{j}_n\cdot\boldsymbol{\nabla}\times\boldsymbol{\rho}_n + \rho_p\boldsymbol{\nabla}\cdot\boldsymbol{J}_p + \boldsymbol{j}_p\cdot\boldsymbol{\nabla}\times\boldsymbol{\rho}_p) \\
&\quad + B_{10}\boldsymbol{\rho}^2 + B_{11}(\boldsymbol{\rho}_n^2 + \boldsymbol{\rho}_p^2) + B_{12}\rho^\alpha + B_{13}\rho^\alpha(\boldsymbol{\rho}_n^2 + \boldsymbol{\rho}_p^2), \qquad (3.14)
\end{aligned}$$

where the densities which have a isospin index n or p defined by each single-particle wave functions with isospin, and the density without isospin index means that of total ($\rho \equiv \rho_n + \rho_p$).

The densities are defined as,

$$
\begin{aligned}
\rho_\tau(\vec{r}) &= \sum_{k,\sigma} |v_{k,\tau}|^2 |\phi_{k,\tau}(\vec{r},\sigma)|^2, \\
\tau_\tau(\vec{r}) &= \sum_{k,\sigma} |v_{k,\tau}|^2 |\boldsymbol{\nabla}\phi_{k,\tau}(\vec{r},\sigma)|^2, \\
\boldsymbol{j}_\tau(\vec{r}) &= \frac{1}{2i}\sum_{k,\sigma} |v_{k,\tau}|^2 (\phi^*_{k,\tau}(\vec{r},\sigma)\boldsymbol{\nabla}\phi_{k,\tau}(\vec{r},\sigma) - \phi_{k,\tau}(\vec{r},\sigma)\boldsymbol{\nabla}\phi^*_{k,\tau}(\vec{r},\sigma)), \\
\boldsymbol{\nabla}\cdot\boldsymbol{J}_\tau(\vec{r}) &= -i\sum_{k,\sigma,\sigma'} |v_{k,\tau}|^2 (\boldsymbol{\nabla}\phi^*_{k,\tau}(\vec{r},\sigma)\times\boldsymbol{\nabla}\phi_{k,\tau}(\vec{r},\sigma'))\cdot\langle\sigma|\boldsymbol{\sigma}|\sigma'\rangle, \\
\boldsymbol{\rho}_\tau(\vec{r}) &= \sum_{k,\sigma,\sigma'} |v_{k,\tau}|^2 \phi^*_{k,\tau}(\vec{r},\sigma)\phi_{k,\tau}(\vec{r},\sigma')\langle\sigma|\boldsymbol{\sigma}|\sigma'\rangle, \qquad (3.15)
\end{aligned}
$$

where $\boldsymbol{\sigma}$ means Pauli spin matrices. Using a generalized Skyrme effective interaction v_{Skyrme} is composed of density- and momentum-dependent two-body interaction with parameters $t_0, x_0, t_1, x_1, t_2, x_2, t_3, x_3, \alpha$ and W :

$$
\begin{aligned}
v_{\text{Skyrme}}(\vec{r}_1,\vec{r}_2) = t_0(1+x_0P_\sigma)\delta(\vec{r}_1-\vec{r}_2) &+ \frac{1}{2}t_1(1+x_1P_\sigma)(\boldsymbol{k'}^2+\boldsymbol{k}^2)\delta(\vec{r}_1-\vec{r}_2) \\
&+ t_2(1+x_2P_\sigma)\boldsymbol{k'}\cdot\delta(\vec{r}_1-\vec{r}_2)\boldsymbol{k} + \frac{1}{6}t_3(1+x_3P_\sigma)\rho^\alpha\delta(\vec{r}_1-\vec{r}_2) \\
&+ iW(\boldsymbol{\sigma}_1+\boldsymbol{\sigma}_2)\cdot\boldsymbol{k'}\times\delta(\vec{r}_1-\vec{r}_2)\boldsymbol{k}, \qquad (3.16)
\end{aligned}
$$

here P_σ is the spin exchange operator and $\boldsymbol{k}$ is the operator $(1/2i)(\boldsymbol{\nabla}_1-\boldsymbol{\nabla}_2)$ acting on ket state and $\boldsymbol{k'}$ is the operator $(-1/2i)(\boldsymbol{\nabla}_1-\boldsymbol{\nabla}_2)$ acting on bra state, we can express the coefficients B_i as:

$$
\begin{aligned}
B_1 &= \frac{1}{2}t_0(1+x_0/2),\ B_2 = -\frac{1}{2}t_0(1/2+x_0),\ B_3 = \frac{1}{4}(t_1(1+x_1/2)+t_2(1+x_2/2)), \\
B_4 &= -\frac{1}{4}(t_1(1/2+x_1)-t_2(1/2+x_2)),\ B_5 = -\frac{1}{16}(3t_1(1+x_1/2)-t_2(1+x_2/2)), \\
B_6 &= \frac{1}{16}(3t_1(1/2+x_1)+t_2(1/2+x_2)),\ B_7 = \frac{1}{12}t_3(1+x_3/2), B_8 = -\frac{1}{12}t_3(1/2+x_3), \\
B_9 &= -\frac{1}{2}W,\ B_{10} = \frac{1}{4}t_0x_0,\ B_{11} = -\frac{1}{4}t_0,\ B_{12} = \frac{1}{24}t_3x_3,\ B_{13} = -\frac{1}{24}t_3. \qquad (3.17)
\end{aligned}
$$

The parameters of SkM* are $t_0 = -2645.0, t_1 = 410.0, t_2 = -135.0, t_3 = 15595.0, x_0 = 0.09$, $x_1 = x_2 = x_3 = 0.0, \alpha = 1/6, W = 130.0$. And the $\frac{\hbar^2}{2m} = 20.73398$ with using the nucleon mass = 938.91897 MeV, $\hbar c = 197.32705$ MeV fm and $e^2/\hbar c = 1/137.03604$, these parameters are obeyed Ref.[65]. The pairing energy functional is added to this, to give the total energy functional, $E[\rho,\kappa] = E_{\text{Sky}}[\rho] + E_g[\kappa]$.

3.3.4 Calculation of time propagation

To solve the Cb-TDHFB equations in real time, we use the simple Euler's algorithm.

$$
\begin{aligned}
i\phi_k(t+2dt) &= i\phi_k(t) + \{h(t+dt) - \epsilon_k(t+dt)\}\phi_k(t+dt) \times 2dt, &(3.18)\\
i\rho_k(t+2dt) &= i\rho_k(t) + \{\kappa_k(t+dt)\Delta_k^*(t+dt) - \text{c.c.}\} \times 2dt, &(3.19)\\
i\kappa_k(t+2dt) &= i\kappa_k(t) + [\kappa_k(t+dt)\{\epsilon_k(t+dt) + \epsilon_{\bar{k}}(t+dt) - 2\lambda\} \\
&\quad +\Delta_k(t+dt)\{2\rho_k(t+dt) - 1\}] \times 2dt. &(3.20)
\end{aligned}
$$

Here, we insert the chemical potential in Eq.(2.39) which cancels a global time-dependent phase at the ground state, $e^{-2i\lambda t}$, for κ_k and Δ_k. To construct the states at the first step of $t = dt$, we use the fourth-order Taylor expansion of the time-evolution operator for the canonical states [24] and use the Euler's method for $\rho_k(dt)$ and $\kappa_k(dt)$. The time step dt is 0.0005 MeV^{-1}. The time evolution is calculated up to $T = 10$ MeV^{-1}.

Chapter 4

Results and Discussion

In this chapter, we show many linear-response calculations with Cb-TDHFB. We apply the Cb-TDHFB method to calculation of the strength functions for Carbon (C), Oxygen (O), Neon (Ne), Magnesium (Mg), Silicon (Si), Sulfur (S), Argon (Ar) and Calcium (Ca) isotopes and several heavy nuclei.

At first, Section 4.1 shows comparison with QRPA calculations in order to confirm that Cb-TDHFB is correct or not, as a time-dependent scheme including pairing correlation. Section 4.2 shows the effect of spin-orbit and Coulomb residual interaction for light deformed nucleus (^{24}Mg) and heavy nucleus (^{208}Pb and ^{154}Sm). Section 4.3 shows typical strength functions for spherical, prolate and oblate nucleus in isovector dipole and isoscalar quadrupole excitations, and effects of pairing correlations in each excitation states. Section 4.4 shows the computational cost of small-amplitude Cb-TDHFB calculation comparing with a recent deformed QRPA calculation for ^{172}Yb. We show also the results of $^{236-240}$U which are heaviest isotopes in our results. Section 4.5 shows comparisons our results with experimental data. There are results of light nuclei (^{16}O, ^{24,26}Mg and ^{40}Ca) and heavy nuclei (^{90}Zr, ^{208}Pb and Sm isotopes) for photo-nuclear reaction cross sections. We mention an one of properties of $E1$ strength distributions with Skyrme interaction. The ground-state data of nuclei presented in above sections are printed in Table 4.1. Table 4.1 shows ground-state properties; total energy, numbers of canonical orbitals for neutron and proton, deformations, chemical potentials, and gap energies defined by Eq. (3.7). These nuclei show a variety of shapes (spherical, prolate and oblate), with and without superfluidity. For nuclei in the superfluid phase with $\Delta \neq 0$, the numbers of canonical orbitals, M_τ are larger than neutron or proton number, but not significantly different. In the case with $\Delta = 0$, of course, we only calculate the occupied orbitals ($M_n = N$ and $M_p = Z$). Therefore, the numerical task of the Cb-TDHFB is in the same order as that of the TDHF. Note that, in the real-time calculation, the numerical cost is proportional to $M_n + M_p$. Section 4.6 shows examples for systematic calculation with Cb-TDHFB. The number of nuclei presented in this section is large (~ 80), so their ground state data are printed in Appendix A we discuss the appearance of low-energy $E1$ strength which is often called “pygmy resonance”, and the effects of pairing correlation for this strength.

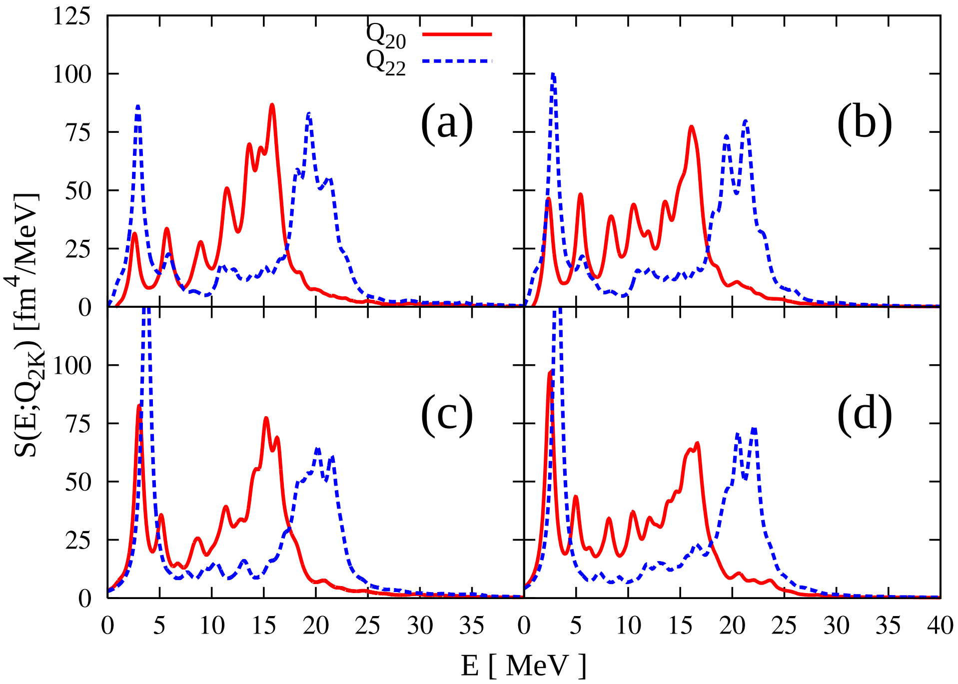

Figure 4.1: Calculated isoscalar quadrupole strength distribution for ^{34}Mg: (a) Cb-TDHFB with time-independent spin-orbit and Coulomb potentials, (b) Cb-TDHFB, (c) Deformed QRPA without the residual spin-orbit and Coulomb interactions[55]. and (d) Deformed QRPA calculation[56]. The smoothing parameter of $\Gamma = 1$ MeV is used.

4.1 Comparison with QRPA calculations

We expect that the strength functions calculated in the present real-time approaches reproduce those in the QRPA. This is strictly true if we solve the full TDHFB equations, however, since we solve the Cb-TDHFB equations with the schematic pairing functional of Eq. (2.72) with (3.1), let us first show the comparison between our result and the HFB+QRPA calculations. The QRPA calculations have been done with a computer program for axially deformed nuclei developed in Ref. [55, 56], which diagonalizes the QRPA matrix of large dimensions in the quasi-particle basis. This is based on the HFB ground state calculated in the two-dimensional coordinate-space representation with the Skyrme functional SkM* but with the density-dependent contact interaction for the pairing channel. The space is truncated by the quasi-particle energy cut-off of $E_{\mathrm{cut}} = 60$ MeV and also by the cut-off for the magnetic quantum number of the quasi-particle angular momentum, $\Omega_{\mathrm{c}} = 19/2$. In this QRPA calculation, the residual spin-orbit and Coulomb interactions are neglected. Thus, in order to make a comparison more meaningful, we also neglect the time-dependence of these potentials in the Hamiltonian $h(t)$, during the time evolution.

In panels (a) and (c) of Fig. 4.1, we show the isoscalar quadrupole strength distributions ($K = 0$ and 2) for ^{34}Mg, calculated with (a) Cb-TDHFB and (c) QRPA calculation of K.Yoshida based on [55]. The ground state has an axially symmetric prolate shape with finite pairing gaps for neutrons (Table 4.1). The HFB calculation with the contact pairing interaction for the panel (c) produces a deformation and average neutron pairing gap of $\beta = 0.37$ and $\Delta_n = 1.7$ MeV, respectively. Note that a renormalization factor, which was used in Ref. [55], is set to be unity in the present QRPA calculation. The peak energies in these calculations are approximately identical, however, the height of the lowest peak is noticeably different. We suppose that this is due to the difference in the pairing energy functionals.

In panels (b) and (d) of Fig. 4.1, we show another comparison between the Cb-TDHFB calculation and the QRPA calculation of Losa *et al.*[56] using the transformed harmonic oscillator basis. Since this QRPA calculation includes all the residual interactions, it is compared with the Cb-TDHFB calculation with the fully self-consistent time dependence. It turns out that the residual spin-orbit and Coulomb interactions slightly shift the giant quadrupole resonance higher in energy, while they shift the lowest peak lower in energy. Actually, these shifts are mainly attributed to the residual spin-orbit interaction and the effect of the residual Coulomb is very small. The results in panels (b) and (d) well agree with each other, except for the height of the lowest peak. We mention these effects of spin-orbit and Coulomb residual interaction in next section. Again, this may be due to the different treatment of the pairing, because Ref. [55, 56] also uses the contact pairing interaction. These comparisons indicate that the small-amplitude Cb-TDHFB calculation well reproduces a fully self-consistent QRPA calculations. We would like to mention that, for the isovector dipole excitations, the agreement is even better than the isoscalar quadrupole cases.

4.2 Full self-consistent calculation

Here, we mention effects of spin-orbit and Coulomb residual interaction in the isovector dipole and isoscalar quadrupole excitations. Sometimes, there are the RPA or QRPA calculations which neglect or do not deal with directly these residual interaction. It is not often reasonable for numerical performance to include directly the effects of these residual interaction with considering the physical meanings caused by these residual interaction. Several (Q)RPA calculations include the effects of these residual interaction with a reasonable approximation, but in some case, these approximation is not good. We report about the “some case” which should need these residual interaction, namely need fully self-consistent calculation.

First, let us show in Fig. 4.2 that the comparison results of the present Cb-TDHFB calculation with those of the RPA calculation. The fully self-consistent RPA calculation has been done with the finite amplitude method (FAM) developed in Refs. [59, 66]. The same Skyrme functional (SkM*) and the same model space have been used in these calculations. Since the ground state of the ^{24}Mg nucleus is in the normal phase ($\Delta = 0$), these two results should be identical. This can be confirmed in Fig. 4.2, which clearly demonstrates the accuracy of our real-time method. From here, we mention the concrete effects of spin-orbit and Coulomb residual interaction. First, we show the effects for isovector dipole mode of ^{24}Mg. In Fig. 4.3, upper panel shows the result of fully self-consistent calculation (solid line labeled “Full”) and the result without both spin-orbit and Coulomb residual interaction (dashed line labeled “Full-(SO,C)”). Under panel show the comparison the result of Full-(SO,C) with the result without only Coulomb residual interaction (dotted line labeled “Full-C”). We can see the effects of

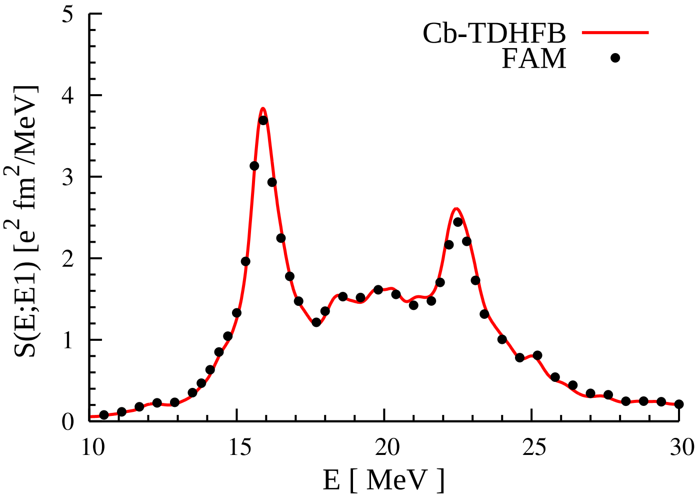

Figure 4.2: $E1$ strength distribution for ^{24}Mg calculated with the Cb-TDHFB (solid line) and with the FAM[59, 66] (symbols). The smoothing parameter of $\Gamma = 1$ MeV is used.

these residual interaction. Upper panel shows that spin-orbit and Coulomb residual interaction shift the peak position of GDR to higher energy only with 80 keV, and under panel shows that the effects of Coulomb residual interaction is almost nothing. This effects of Coulomb residual interaction can be expected that ^{24}Mg is a light nucleus, so the effects is small. At later, we mention the effects of Coulomb part for heavy nucleus.

Next, we mention the effects of residual interactions for isoscalar quadrupole mode for ^{24}Mg. Fig. 4.4 shows the results for Q_{20}-vibration mode of ^{24}Mg, and Fig. 4.5 shows the results for Q_{22}-vibration mode of ^{24}Mg. In the both Fig. 4.4 and Fig. 4.5, Solid line labeled “Full” means the result of fully self-consistent calculation, in (b)-panel, dashed line labeled “Full-SO” means the result without only spin-orbit residual interaction, in (c)-panel, dashed line labeled “Full-C” means the result without only Coulomb residual interaction and in (d)-panel, dashed line labeled “Full-(SO,C)” means the result without both spin-orbit and Coulomb residual interaction. In the both Q_{20}- and Q_{22} modes, we can see the significantly effects of spin-orbit residual interaction and the effects of Coulomb part is very small. The effects of spin-orbit residual interaction in isoscalar quadrupole mode shift the low-energy strength to lower energy region and giant resonance to higher energy region at same time. The effects of spin-orbit residual interaction for isoscalar quadrupole mode are much stronger than those for isovector dipole mode in ^{24}Mg. From these results (isovector dipole mode and isoscalar quadrupole mode), we can consider that the spin-orbit residual interaction has a dependence on an excitation mode.

Next, we show the effects of residual interactions for heavy nucleus case. For example, we mention the effects for isovector dipole mode of the heavy spherical nucleus ^{208}Pb and the heavy prolate deformed nucleus ^{154}Sm. First, we mention the effects of spin-orbit residual interaction for isovector dipole mode of heavy nucleus. Fig. 4.6 shows photo-nuclear reaction cross sections of ^{208}Pb computed from isovector dipole mode results. This value can be compared with experimental values and at later we show the comparison in Section 4.5. The ground state of ^{208}Pb is spherical with $\beta = 0.0$ and HF state with $\Delta_{\rm n} = \Delta_{\rm p} = 0$. Solid line labeled “Full” means

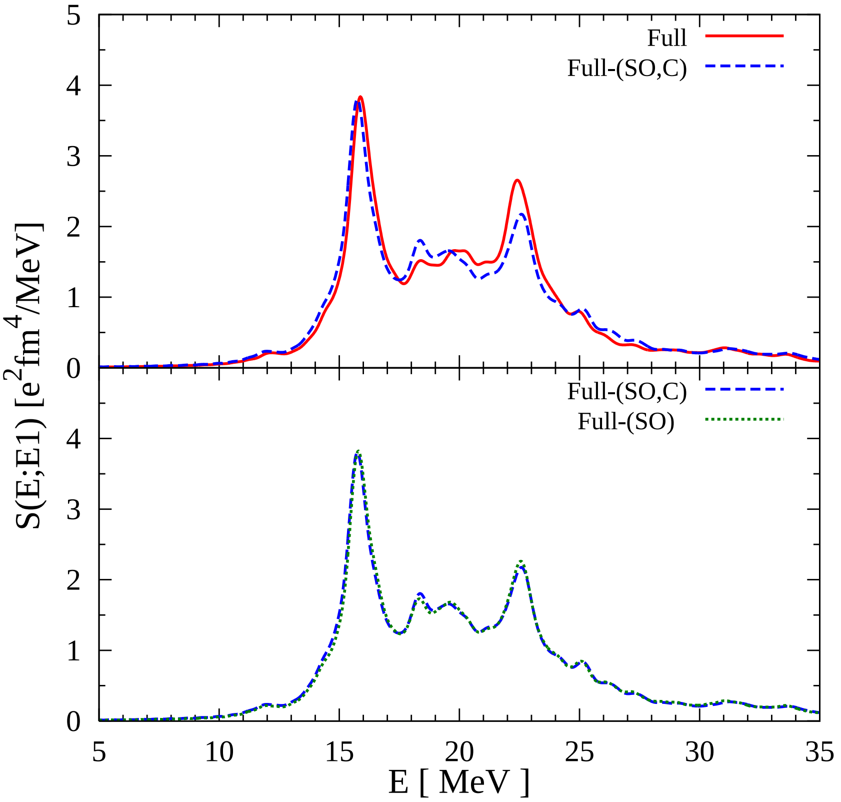

Figure 4.3: Comparison the fully self-consistent calculation with the calculation neglected residual interactions for isovector dipole mode of ^{24}Mg. Solid line means the fully self-consistent calculation, dashed line means the calculation without spin-orbit and Coulomb residual interaction and dotted line means the calculation without only Coulomb residual interaction.

fully self-consistent calculation and dashed line labeled "Full-SO" means the result without spin-orbit residual interaction. From Fig. 4.6, spin-orbit residual interaction moves the peak position of GDR to higher region with 400 keV. This effects is bigger than that of ^{24}Mg.

Next, we mention the effects of Coulomb residual interaction for isovector dipole mode of heavy deformed nucleus. Fig. 4.7 shows photo-nuclear reaction cross sections of ^{154}Sm computed from isovector dipole mode results. The ground state of ^{154}Sm is prolate deformed with deformation parameter $\gamma = 0°$ and $\beta = 0.32$, and HF+BCS state with $\Delta_{\rm n} = 0.87,\ \Delta_{\rm p} = 0.99$MeV. In the Fig. 4.7, we compare fully self-consistent calculation (solid line labeled "Full") with the results neglected Coulomb residual interaction (dashed line labeled "Full-C"). We can see the effects of Coulomb residual interaction in the both $K = 0, 1$ vibration modes. Coulomb residual interaction shifts the peak position of GDR to higher energy. The effects of Coulomb part for isovector dipole modes in heavy nuclear system is much bigger than those in light nuclear system as like ^{24}Mg.

Above discussions can be summarized two things. One is that spin-orbit residual interaction

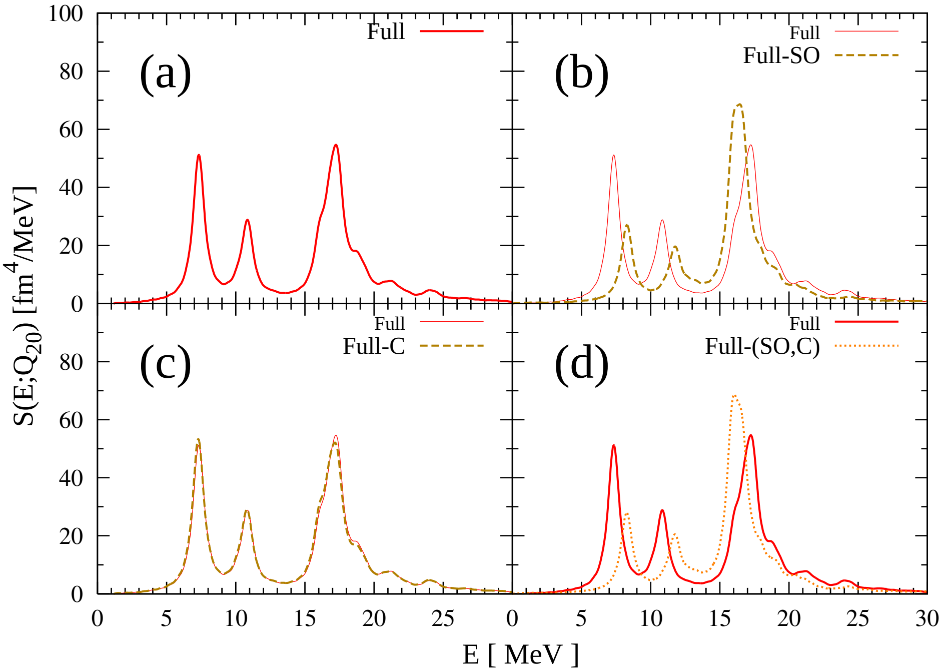

Figure 4.4: Fully self-consistent calculation and the calculations without spin-orbit or Coulomb or both residual interaction for isoscalar quadrupole mode ($K = 0$ channel) of ^{24}Mg. (a)-panel shows only the result of fully self-consistent calculation (solid line labeled “Full”). (b)-panel shows the comparison “Full” with the result without only spin-orbit residual interaction (dashed line labeled “Full-SO”). (c)-panel shows the comparison “Full” with the result without only Coulomb residual interaction (dashed line labeled “Full-C”). (d)-panel shows the comparison “Full” with the result without both spin-orbit and Coulomb residual interaction (dotted line labeled “Full-(SO,C)”).

has dependence on excitation modes and the dependence is not small. The other is that the effects of Coulomb residual interaction are negligible in light nuclear system, but in heavy nuclear system the effects become much bigger. In this section, we discuss the effects of residual interaction for giant resonance mainly. The discussion about low-energy part has remained yet, and about the effects for isoscalar quadrupole mode of heavy nucleus has also remained yet. In future work for this part, we want to suggest the auxiliary measures which can be able to include the effects of residual interaction to (Q)RPA calculation easily. Lastly of this section, we mention the “some case” which needs fully self-consistent calculation. At least, we need fully self-consistent calculation for isoscalar quadrupole mode of deformed nuclei, because there are the effects of spin-orbit residual interaction for both low-energy and giant resonance parts.

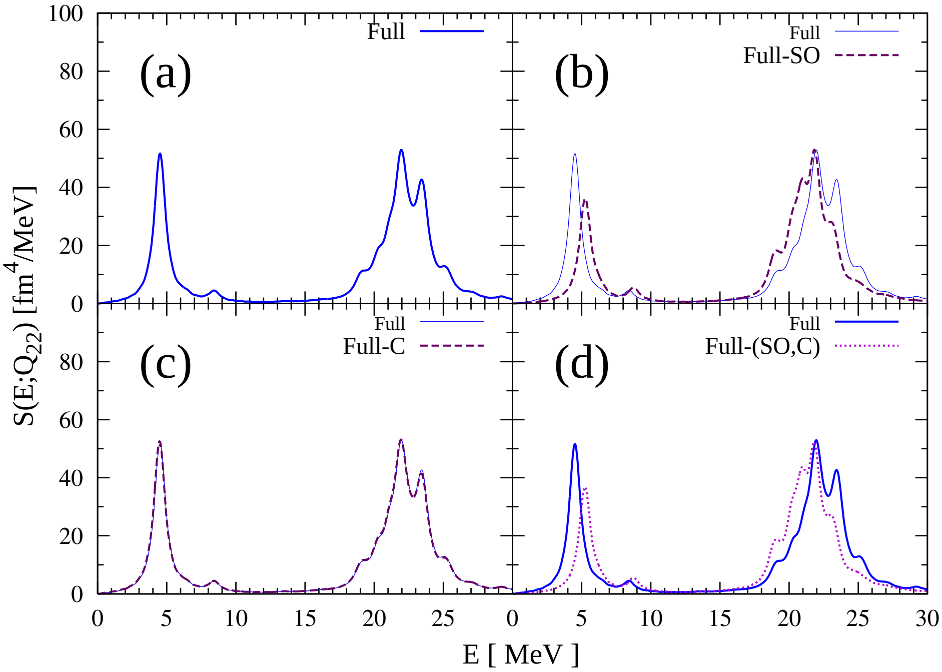

Figure 4.5: Fully self-consistent calculation and the calculations without spin-orbit or Coulomb or both residual interaction for isoscalar quadrupole mode ($K = 2$ channel) of ^{24}Mg. The meanings of the lines are same as Fig. 4.4

4.3 Typical strength functions for spherical, prolate and oblate nucleus

In this chapter, we show many and various strength functions. But these strength functions can be categorized with some characters. We categorize these strength functions on their shape; spherical, prolate and oblate shapes. Following sections, we mention the typical strength functions of spherical, prolate and oblate nucleus for isovector dipole and isoscalar quadrupole excitations, and effects of pairing correlation in each excitations. We consider low- and high-energy parts of strength functions. The low-energy (< 10 MeV) strength are important parts to investigate especially the structure of single-particle levels and effects of pairing correlation. The high-energy (∼ 20 MeV) strength are important to investigate collective motion of a nucleus. This part is often called giant resonance (GR) part, for example, isovector dipole case is called giant dipole resonance (GDR). GR are produced by nuclear-surface vibration basically.

4.3.1 Example of spherical nucleus (^{34}Si)

Here, we show the results of ^{34}Si which is spherical nucleus. For spherical nuclei case, the angular momentum is a good quantum number. This means that we cannot distinguish the rotational axis. Namely, spherical system has isotropic strength functions in dipole external fields for all axes.

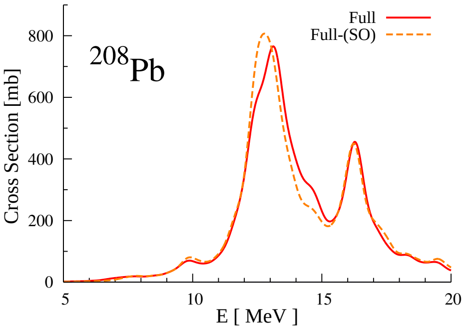

Figure 4.6: Isovector dipole strength distributions produced by the fully self-consistent calculation and the calculation without spin-orbit residual interaction, for spherical nucleus ^{208}Pb. Solid line shows fully self-consistent result, dashed line shows the result without spin-orbit residual interaction.

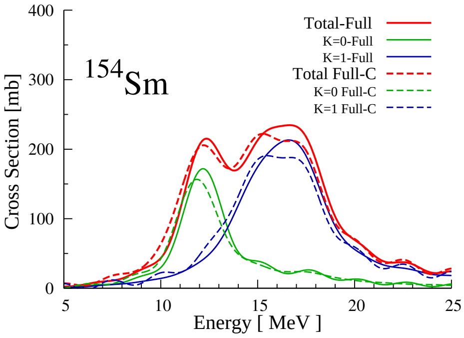

Figure 4.7: Isovector dipole strength distributions produced by the fully self-consistent calculation and the calculation without Coulomb residual interaction, for prolate deformed nucleus ^{154}Sm. Solid line shows fully self-consistent result, dashed line shows the result without Coulomb residual interaction.

As a concrete example, we show the result of ^{34}Si which has spherical ground state in both cases with and without pairing correlation. Fig. 4.8 shows the isovector dipole strength distributions $S(E;E1)$ for ^{34}Si with while the pairing correlation. The solid line shows the result with pairing correlation, dashed line shows the result without pairing correlation. Here, $S(E;E1)$ is defined as

$$S(E;E1) = \sum_{i=x,y,z} S_i(E;E1) = \sum_{i=x,y,z} \sum_n |\langle n|F_i|0\rangle|^2 \delta(E - \tilde{E}_n), \tag{4.1}$$

where the one-body operator F_i is given by Eq. (3.8). The $K = 0$ strength is $S_z(E;E1)$ and $K = 1$ corresponds to $S_x(E;E1) + S_y(E;E1)$.

The dipole strength is concentrated in a single peak at giant resonance in the both results TDHF and Cb-TDHFB. There is little effects of pairing correlation for GDR.

Next, we show the strength functions of isoscalar quadrupole mode for spherical nuclei. Fig. 4.9 shows results of TDHF with the ground state written by HF approximation, and Fig. 4.10 shows results of Cb-TDHFB with the ground state written by HF+BCS approximation. The difference of total energy between HF+BCS and HF ground state is about 200 keV, the HF+BCS ground state is more stable than HF one of ^{34}Si. In the each figures, solid line means the result of Q_{20}-vibration and dashed line means the result of Q_{22}-vibration. These figures show same strength distributions for Q_{20}- and Q_{22}-vibration in both Cb-TDHFB and TDHF. For spherical nuclei case, they do not have the distinguishable axes, so the external field of Q_{20} is equivalent to Q_{22} in this system. Spherical nuclei should have same strength distributions for Q_{20} and Q_{22} modes. In the results of Cb-TDHFB, the strength distributions for Q_{20} and Q_{22} modes in low-energy have some difference. This reason is that the initial state of Cb-TDHFB has some expectation value of Q_{22}. The order of "some" value is 10^{-5} fm^2. For the linear-response results with real-time scheme, it is very important the accuracy of a ground state. In spherical

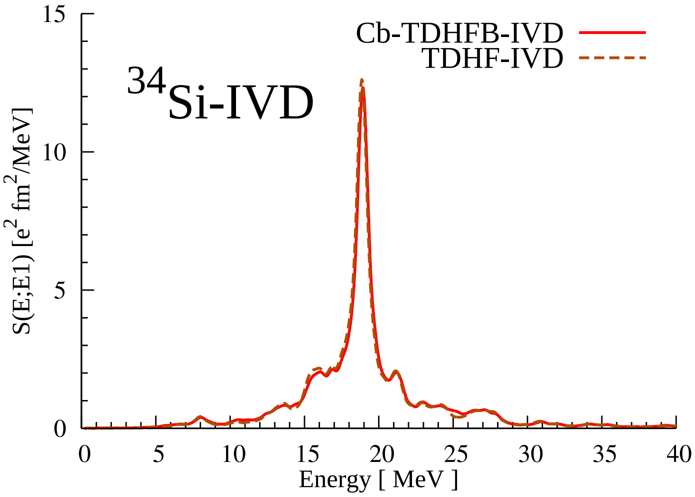

Figure 4.8: Calculated isovector dipole strength distributions for ^{34}Si. Solid line shows a result of Cb-TDHFB calculation with pairing correlation, $\Delta_n = 1.63$ MeV. Dashed line shows a result of TDHF calculation without pairing correlation. The smoothing parameter of $\Gamma = 1$ MeV is used on each calculations.

nuclei, the effects of pairing correlation are small for the giant isoscalar quadrupole resonance. A low-energy strength shifts to lower energy with 200 keV, but it is not so big change.

4.3.2 Example of prolate nucleus (^{34}Mg)

Here, we show the results of ^{34}Mg as an example of prolate deformed nuclei. ^{34}Mg has the HF and HF+BCS ground state of prolate shape. The deformation parameter of both ground states are $\gamma = 0°$, and HF state has $\beta_{\mathrm{HF}} = 0.41$ and HF+BCS state has $\beta_{\mathrm{BCS}} = 0.37$. Generally, pairing correlation influences the shape of nuclei to become close to spherical. This ^{34}Mg case has also this tendency. The difference of total energy between HF+BCS and HF ground state is about 400 keV. HF+BCS ground state is more stable than HF one. First, we show the results of isovector dipole mode for ^{34}Mg. Fig. 4.11 shows the results of TDHF with HF ground state and Fig. 4.12 shows the results of Cb-TDHFB with HF+BCS ground state. Basically, the isovector giant dipole resonance of axial symmetric deformed nuclei has separated peaks. The vibrations along major and minor axes generate two giant resonances. We usually regard that prolate deformed (axial-deformed) nuclei have two axes which a major axis is rotational symmetric one and a minor axes is vertical to the major axis. Axial symmetric deformed nuclei have K-quantum number in stead of angular momentum. K-quantum number is a projected angular momentum to rotational symmetric axis. In the both Fig. 4.11 and Fig. 4.12, solid lines mean the sum of strength distributions for major and minor axes, dashed lines labeled $K = 0$ mean the distribution produced by the vibration along major axis and dot lines labeled $K = 1$ mean that along minor axis. The energy peak of giant resonance of $K = 0$ is lower energy than that of $K = 1$. When we can regard these giant resonance produced by surface vibration, the circumference of ellipsoid for major axis direction is longer than that for minor axis direction, the vibrational cycle on the circumference for major axis is longer than that for minor axis. From

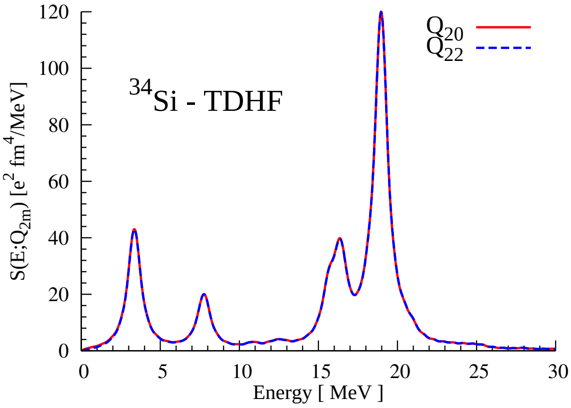

Figure 4.9: The isoscalar quadrupole strength distributions for spherical nucleus ^{34}Si with using TDHF. Solid line shows result of Q_{20} vibration, dashed line shows result of Q_{22} vibration. The smoothing parameter of $\Gamma = 1$ MeV is used.

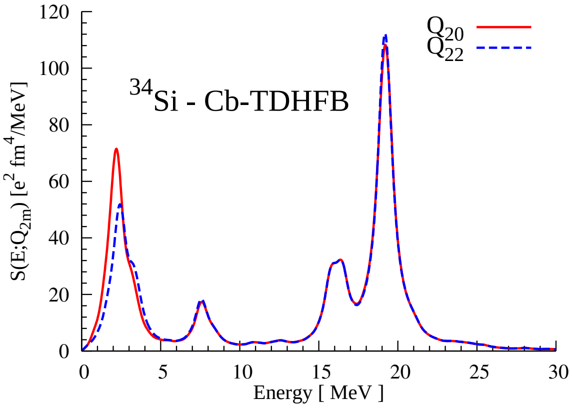

Figure 4.10: The isoscalar quadrupole strength distributions for spherical nucleus ^{34}Si with using Cb-TDHFB. The meanings of the lines are same as Fig. 4.9. The smoothing parameter of $\Gamma = 1$ MeV is used.

this reason, the energy peak of giant resonance of $K = 0$ is lower energy than that of $K = 1$. This relation is one of character for prolate deformed nuclei. The effects of paring correlation for isovector dipole mode of prolate deformed nuclei are also small, but we can see that the peaks of two giant resonances become slightly close, and the low-energy strengths extend slightly to lower energy region.

Next, we show results of isoscalar quadrupole excitation for prolate deformed nucleus ^{34}Mg. Fig. 4.13 shows the results of TDHF with HF ground state and Fig. 4.14 shows the result of Cb-TDHFB with HF+BCS ground state. In the case of axial symmetric quadrupole deformed nuclei, there is the relation for between the modes produced by external field Q_{20} and Q_{22} which are sometimes called Q_{20}- and Q_{22}-vibration. In the both Fig. 4.13 and Fig. 4.14, solid lines mean result of Q_{20}-vibration and dashed lines mean result of Q_{22}-vibration. In prolate nuclei case, the giant resonance of isoscalar quadrupole vibration are also two part as like the case of isovector dipole mode, and the peak position of giant resonance produced by Q_{20}-vibration is lower than that produced by Q_{22}-vibration. The effects of pairing correlation for isoscalar quadrupole mode of deformed nuclei appears in low-energy region. Form comparison Fig. 4.13 with Fig. 4.14, we can see that solid line has the new mode in lower than 3 MeV obviously. There is no significantly difference in the dashed line. This new mode can be expected pairing vibration. Axial symmetric deformed nuclei have K-quantum number that we already have mentioned, so in this axial symmetric deformed system, external field Q_{20} can induce $K = 0$ states of nuclear system. The pair of nucleons with total angular momentum zero can be induced by the external field Q_{20}, but it is not induced by the external field Q_{22}. The pairing vibration mode appear in the energy less than a breaking energy of nucleon pair. This breaking energy of pair is characterized by gap energy as 2Δ. Actually, the breaking energy of pair can be evaluated with gap energy in ^{34}Mg to $2\Delta_{\rm n} \simeq 3$ MeV. In adding, the external fields of Q_{20} and Q_{22} for spherical system only induce $L = 2$ state, so the pair vibration mode with $K = 0$ does not appear.

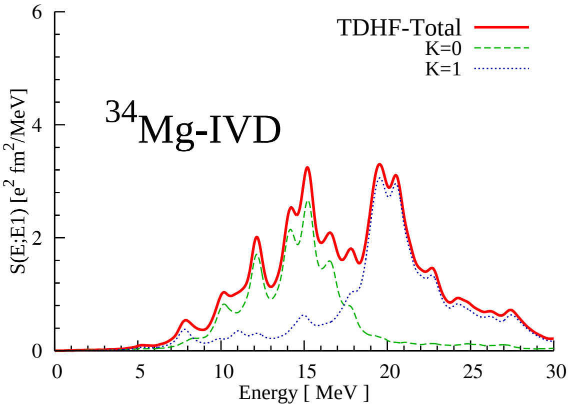

Figure 4.11: The isovector dipole strength distribution for ^{34}Mg with HF ground state which does not include pairing correlation. HF ground state of ^{34}Mg is prolate deformed shape with $\beta = 0.41$. Solid line means the sum of strengths for $K = 0$ and $K = 1$ channels. Dashed line indicates the strength of $K = 0$ channel and dotted line indicates the strength of $K = 1$ channel. The smoothing parameter of $\Gamma = 1$ MeV is used.

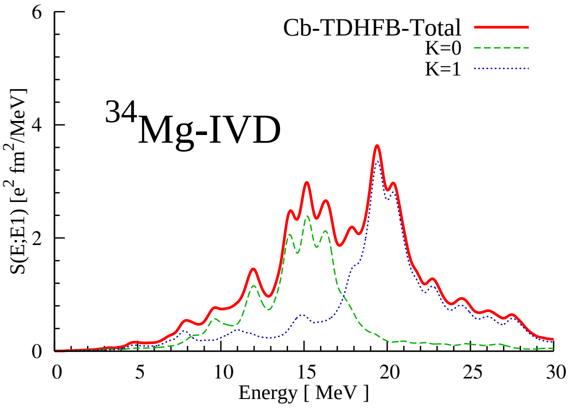

Figure 4.12: The isovector dipole strength distribution for ^{34}Mg with HF+BCS ground state which includes pairing correlation, $\Delta_{\rm n} = 1.45$ MeV. HF+BCS ground state of ^{34}Mg is prolate deformed shape with $\beta = 0.37$. The meanings of the lines are same as Fig. 4.11. The smoothing parameter of $\Gamma = 1$ MeV is used.

4.3.3 Example of oblate nucleus (^{24}Ne)

Here, we show the results of ^{24}Ne as an example of oblate deformed nuclei. ^{24}Ne has the HF and HF+BCS ground state of oblate shape. The deformation parameter of both ground states are $\gamma = 60°$, and HF state has $\beta_{\rm HF} = 0.20$ and HF+BCS state has $\beta_{\rm BCS} = 0.17$. The shape of nuclei closes to spherical by pairing correlation in this oblate shape case also. The difference of total energy between HF+BCS and HF ground state is about 300 keV. HF+BCS ground state is more stable than HF one. First, we show the results of isovector dipole mode for ^{24}Ne. Fig. 4.15 shows the results of TDHF with HF ground state and Fig. 4.16 shows the results of Cb-TDHFB with HF+BCS ground state. In the case of oblate deformed nuclei, the isovector giant dipole resonance has also separated peaks. The vibrations along major and minor axes generate two giant resonances. In this case also, we regard usually that oblate deformed nuclei have two axes which a minor axis is rotational symmetric one and a major axes is vertical to the minor axis. In the case of ^{24}Ne, however the peaks do not obvious separate ones, because its deformation parameter is relatively small. In the both Fig. 4.15 and Fig. 4.16, solid lines mean the sum of strength distributions for major and minor axes, dashed lines labeled $K = 0$ mean the distribution produced by the vibration along minor axis and dot lines labeled $K = 1$ mean that along major axis. The energy peak of giant resonance of $K = 0$ is higher energy than that of $K = 1$. This character of GDR is opposite in prolate deformed nuclei. The effects of paring correlation for isovector dipole mode of oblate deformed nuclei are also small.

Next, we show results of isoscalar quadrupole excitation for oblate deformed nucleus ^{24}Ne. Fig. 4.17 shows the results of TDHF with HF ground state and Fig. 4.18 shows the results of Cb-TDHFB with HF+BCS ground state. In the both Fig. 4.17 and Fig. 4.18, solid lines mean

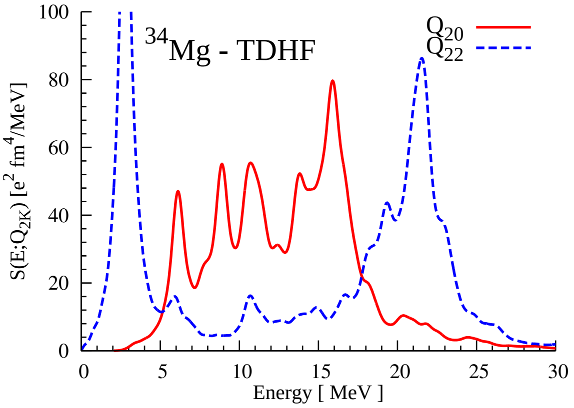

Figure 4.13: The isoscalar quadrupole strength distributions for ^{34}Mg with using TDHF. The meanings of the lines are same as Fig. 4.9. The smoothing parameter of $\Gamma = 1$ MeV is used.

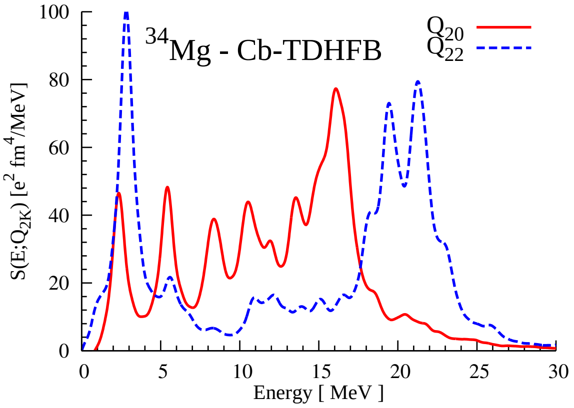

Figure 4.14: The isoscalar quadrupole strength distribution for ^{34}Mg with using Cb-TDHFB. The meanings of the lines are same as Fig. 4.9. The smoothing parameter of $\Gamma = 1$ MeV is used.

result of Q_{20}-vibration and dashed lines mean result of Q_{22}-vibration. In oblate nuclei case, the peak position of giant resonance produced by Q_{20}-vibration is higher than that produced by Q_{22}-vibration. There appear the effects of pairing correlation for isoscalar quadrupole mode in low-energy region. Form comparison Fig. 4.17 with Fig. 4.18, we can see that solid line has the new mode in lower than 1.5 MeV obviously. This new mode can be expected pairing vibration also as like prolate case. There is no significantly difference of peak position in the dashed line. K-quantum number is also good quantum number in oblate deformed nuclei, so the external field Q_{20} can induce the pair of nucleons with $K = 0$ but, the external field Q_{22} does not. The breaking energy of pair can be evaluated with gap energy in ^{24}Ne to $2\Delta_{\rm n} \simeq 1.5$ MeV. The character of this pairing vibration mode is consistent with prolate results.

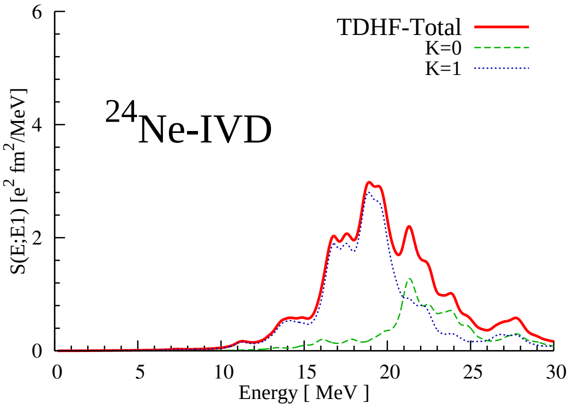

Figure 4.15: The isovector dipole strength distribution for ^{24}Ne with HF ground state which does not include pairing correlation. HF ground state of ^{24}Ne is oblate deformed shape with $\gamma = 60°$ and $\beta = 0.20$. The meanings of the lines are same as Fig. 4.11. The smoothing parameter of $\Gamma = 1$ MeV is used.

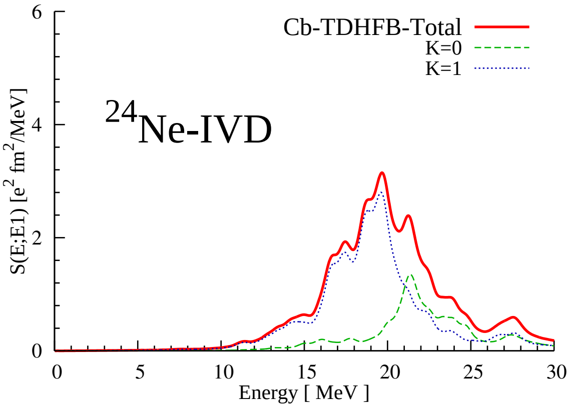

Figure 4.16: The isovector dipole strength distribution for ^{24}Ne with HF+BCS ground state which includes pairing correlation, $\Delta_{\mathrm{p}} = 0.74$. HF+BCS ground state of ^{24}Ne is oblate deformed shape with $\gamma = 60°$ and $\beta = 0.17$. The meanings of the lines are same as Fig. 4.11. The smoothing parameter of $\Gamma = 1$ MeV is used.

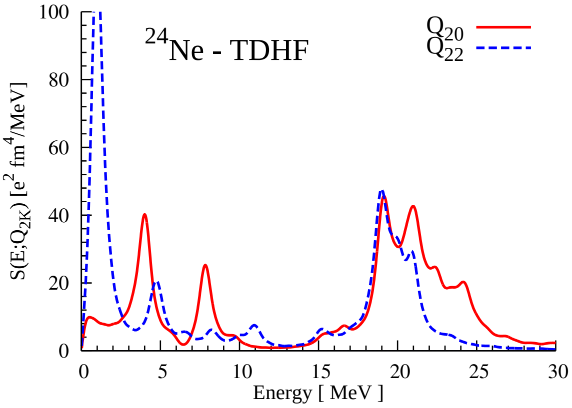

Figure 4.17: The isoscalar quadrupole strength distributions for oblate deformed nucleus ^{24}Ne with using TDHF. The meanings of the lines are same as Fig. 4.9. The smoothing parameter of $\Gamma = 1$ MeV is used.

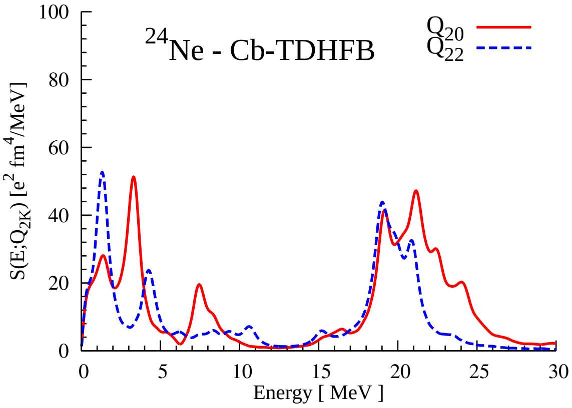

Figure 4.18: The isoscalar quadrupole strength distributions for oblate deformed nucleus ^{24}Ne with using Cb-TDHFB. The meanings of the lines are same as Fig. 4.9. The smoothing parameter of $\Gamma = 1$ MeV is used.

Table 4.1: Calculated ground-state properties of the nuclei presented in this chapter; total energy E_{Total}, numbers of canonical orbitals for neutrons and protons Orbitals(n, p) which are chosen in our energy cutoff given in Chapter 3, quadrupole deformation parameters (β, γ) which are given in Appendix D, pairing gaps (3.7) for neutrons and protons (Δ_n, Δ_p), chemical potentials for neutrons and protons (λ_n, λ_p). In the case of normal phase $(\Delta = 0)$, we define the chemical potential as the single-particle energy of the highest occupied orbital, $\lambda_n = \epsilon^0_N$ and $\lambda_p = \epsilon^0_Z$. In the cases of ^{24}Ne,^{34} Mg and ^{34}Si, both situations whose ground states are written HF or HF+BCS approximation, are presented for comparison between results of normal and superfluid phase. When pairing gap energy is zero (normal phase), the number of used orbitals is equivalent to that of HF single-particle state. The total energy, pairing gaps and chemical potentials are given in units of MeV.

	$-\mathrm{E}_{\text{Total}}$	Orbitals (n, p)	β	γ	Δ_n	Δ_p	$-\lambda_n$	$-\lambda_p$
^{16}O	127.798	(16, 16)	0.0	–	0.0	0.0	13.53	10.25
^{24}Ne-$_{\text{BCS}}$	195.051	(20, 16)	0.17	60°	0.0	0.74	10.57	13.03
^{24}Ne-$_{\text{HF}}$	194.870	(14, 10)	0.20	60°	0.0	0.0	10.62	13.50
^{24}Mg	197.299	(12, 12)	0.39	0°	0.0	0.0	14.11	9.50
^{34}Mg-$_{\text{BCS}}$	264.071	(28, 20)	0.37	0°	1.45	0.0	4.11	20.17
^{34}Mg-$_{\text{HF}}$	263.658	(22, 12)	0.41	0°	0.0	0.0	5.10	20.31
^{34}Si-$_{\text{BCS}}$	287.935	(32, 20)	0.0	–	1.63	0.0	6.56	16.94
^{34}Si-$_{\text{HF}}$	287.486	(20, 14)	0.0	–	0.0	0.0	7.87	16.99
^{40}Ca	341.559	(32, 28)	0.0	–	0.0	0.0	14.31	7.47
^{90}Zr	790.943	(82, 50)	0.0	–	0.0	1.75	12.75	7.18
$^{144}_{62}$Sm	1202.517	(126, 82)	0.0	–	0.0	1.97	12.26	4.41
$^{146}_{62}$Sm	1217.104	(126, 82)	0.0	–	0.93	1.94	7.18	4.96
$^{148}_{62}$Sm	1230.314	(128, 82)	0.12	0°	0.90	1.62	7.21	5.41
$^{150}_{62}$Sm	1244.523	(128, 84)	0.20	0°	0.94	1.45	7.30	6.01
$^{152}_{62}$Sm	1259.717	(126, 90)	0.29	0°	1.04	1.08	7.63	6.62
$^{154}_{62}$Sm	1274.550	(130, 92)	0.32	0°	0.87	0.99	7.23	7.15
$^{172}_{70}$Yb	1398.567	(146, 98)	0.32	0°	0.76	0.55	7.60	5.62
$^{236}_{92}$U	1796.988	(200,132)	0.267	0°	0.59	0.47	6.19	5.20
$^{238}_{92}$U	1809.022	(200,130)	0.273	0°	0.52	0.58	5.91	5.64
$^{240}_{92}$U	1820.381	(202,130)	0.274	0°	0.46	0.70	5.53	6.04

4.4 Computational cost (^{172}Yb, ^{236,238,240}U)

In this section, we show the computational costs of Cb-TDHFB calculation for linear response of several heavy nuclei. We have already mentioned that the computational cost of Cb-TDHFB calculation will be much smaller than that of TDHFB calculation. But, there are no results of TDHFB with modern effective interaction in three-dimensional coordinate space representation. So first, we compare with fully self-consistent HFB+QRPA calculation for axially deformed nucleus ^{172}Yb [57] in order to show that Cb-TDHFB can reduce the computational costs.

Fig. 4.19 shows the calculation result of isovector dipole mode of ^{172}Yb. Left panel shows the result of J.Terasaki and J.Engel [57], and right panel shows the result of Cb-TDHFB calculation. In our calculation, the ground state of ^{172}Yb is prolate deformed with the deformation parameters $\gamma = 0°$ and $\beta = 0.32$, and HF+BCS state with $\Delta_{\rm n} = 0.76,\ \Delta_{\rm p} = 0.55$ MeV. In their calculation, the ground state of ^{172}Yb is prolate deformed with the deformation parameters $\gamma = 0°$ and $\beta = 0.34$, and axially deformed HFB state with $\Delta_{\rm n} = 0.77,\ \Delta_{\rm p} = 1.25$ MeV. In each panels, solid line means a sum of results along a rotational axis ($K = 0$) and vertical to axial symmetric direction axes ($K = 1$). Our Cb-TDHFB calculation produce almost same result with one of Terasaki and Engel, except for width of total strength distribution. We mention the each computational costs. The result (A) needs about 136,000 CPU hours in the parallel computation with 10,000 CPU. Our result (B) needs only about 300 CPU hours in a single processor.

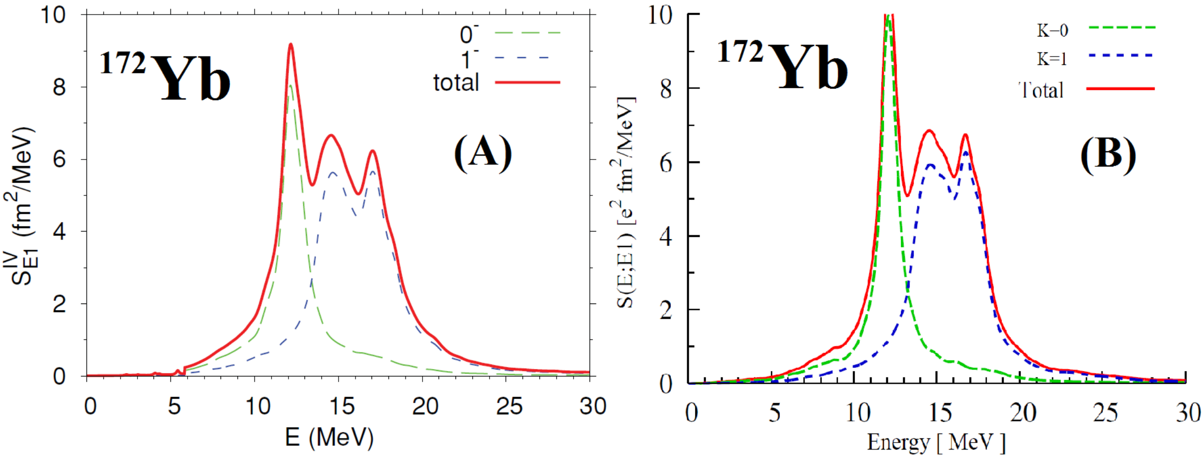

Figure 4.19: Isovector dipole strength distributions calculated by (A) axially deformed HFB+QRPA of J.Terasaki and J.Engel [57] and by (B) our Cb-TDHFB, for prolate deformed nucleus ^{172}Yb. The meanings of the lines are same as Fig. 4.11.

In addition, we show, as examples of other heavy nuclei, results of uranium isotopes. Fig. 4.20 show the photo-nuclear reaction cross section computed with isovector dipole modes of ^{236,238,240}U. Dashed line means the result of $K = 0$ channel, dotted line means the result of $K = 1$ channel and solid line means the sum of those. Black points and error bar show the experimental data taken from [67]. These ground states of $^{236-240}$U are all HF+BCS state and all prolate deformed. The calculation result of ^{238}U well agree with experimental data. The computational costs of each result need about 400 CPU hours, and if we mention only real-time part, the costs are only about 40 CPU hours in a single processor. We can say with above results, that Cb-TDHFB significantly reduces the computational costs at least for linear response, can produce reasonable results with the practical costs.

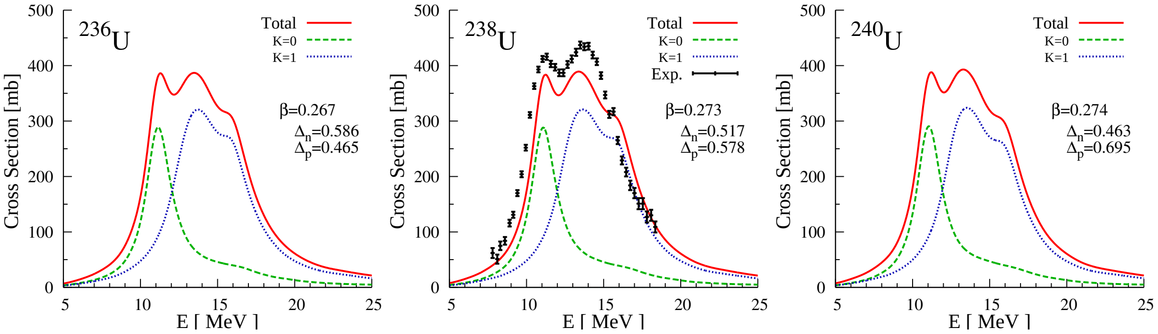

Figure 4.20: Photo-nuclear reaction cross section for uranium isotopes with $N = 144$,146 and 148. Their ground states are prolate deformed ($\gamma = 0°$) and HF+BCS states. The each deformation parameters (β) and gap energies ($\Delta_{\rm n}, \Delta_{\rm p}$) are printed in each panels. The meanings of the lines are same as 4.11, the black points and error bar mean experimental data taken from [67]. The smoothing parameter of $\Gamma = 2$ MeV is used for the calculations.

4.5 Comparison with experiments (^{16}O, $^{24-26}$Mg, ^{40}Ca, ^{90}Zr, $^{144-154}$Sm, ^{208}Pb)

This section, let us present photo-absorption cross sections in the GDR energy region ($E = 10 \sim 30$ MeV) for ^{16}O, $^{24-26}$Mg, ^{40}Ca, ^{90}Zr, $^{144-154}$Sm and ^{208}Pb together with experimental data[68, 69, 70, 71, 72, 73]. We can calculate photo-absorption cross section σ easily from isovector dipole (IVD) strength function $S(E; E1)$, as like

$$\sigma_n(\varepsilon) = \frac{4\pi^2 e^2}{\hbar c}\tilde{E}|\langle\Phi_n|F_{\rm IVD}|\Phi_0\rangle|^2\delta(\varepsilon - \tilde{E}), \tag{4.2}$$

where F_{IVD} is $E1$ operator given by (3.8) and $\tilde{E}$ means excited energy given in Section 3.2. We can namely get the photo-absorption cross section with only to time excited energy $\tilde{E}$ and some coefficient to $S(E; E1)$. For ^{24}Mg, the peak energies of the GDR are underestimated by about 3 MeV. This disagreement has been already found in Ref.[66] for ^{24}Mg. The present calculation also indicates that this underestimation of the GDR peak energy is also true for ^{26}Mg. The $E1$ strength distribution for ^{26}Mg is very similar to that in Fig.12 (bottom panel) in Ref. [56]. In light nuclei (^{16}O and $^{24-26}$Mg), the GDR energy is systematically underestimated in most of the Skyrme functionals[66], that seems to be true for nuclei with superfluidity. This underestimations on the calculations with Skyrme functional has an alleviated tendency in heavier nuclei. The GDR of ^{40}Ca become close to experimental data, and the mean energy of GDR for ^{90}Zr and ^{208}Pb well agree with experimental data. Next, we show the shape transition with respect

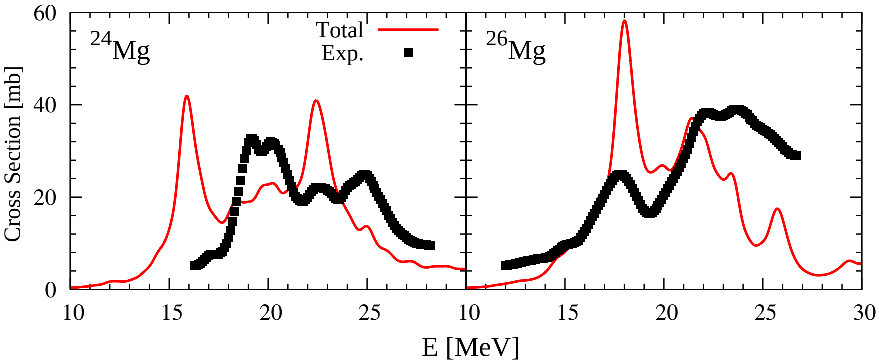

Figure 4.21: Photoabsorption cross sections for ^{24,26}Mg. Experimental data (symbols) are taken from Ref. [68]. The smoothing parameter of $\Gamma = 1$ MeV is used for the calculations.

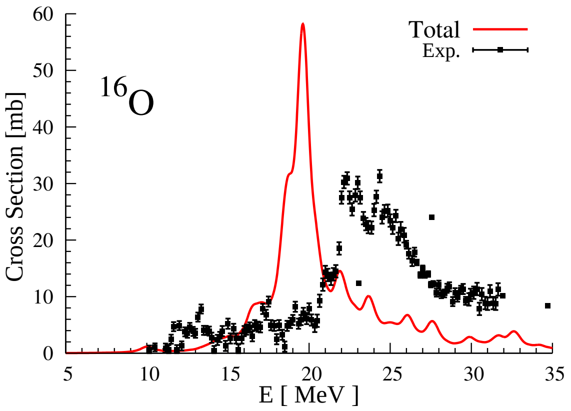

Figure 4.22: Photoabsorption cross sections for ^{16}O. Experimental data (symbols) are taken from Ref. [69]. The smoothing parameter of $\Gamma = 1$ MeV is used for the calculations.

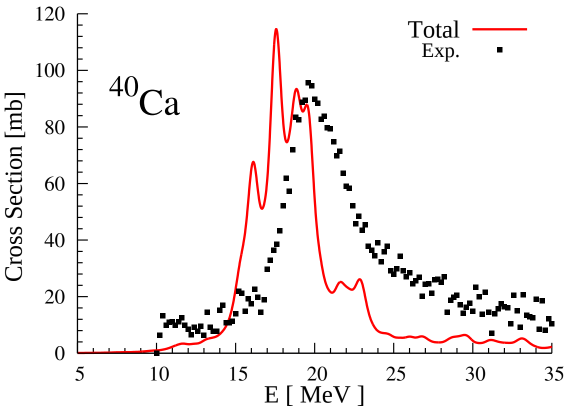

Figure 4.23: Photoabsorption cross sections for ^{40}Ca. Experimental data (symbols) are taken from Ref. [68]. The smoothing parameter of $\Gamma = 1$ MeV is used for the calculations.

to neutron number and experimental data for lanthanide isotopes. There are many deformed nuclei in lanthanide isotopes, and we can see the aspects of shape transition with respect to neutron number in this isotopes. As an example of the shape transition, we show the photo-nuclear reaction cross section of samarium isotopes from $N = 82$ to $N = 92$, samarium is an one of lanthanide elements. ^{144,146}Sm has $N = 82, 84$ and they are spherical. $N = 82$ is a magic number. The photo-nuclear reaction cross sections of ^{144,146}Sm are in a single peak concentrated at giant resonance. The experimental data of ^{144}Sm also indicate spherical shape. This reason has been also mentioned in Section 4.3. $^{148-154}$Sm have prolate shape for their ground state. Their characters of prolate shape become clear gradually in photo-nuclear reaction cross section with increasing neutron number. This character also appears in other lanthanide isotopes (neodymium etc.)[2, 74]. The experimental data have also same character that the GDR is not separated peak but the width of GDR becomes wide in ^{148,150}Sm, and the GDR

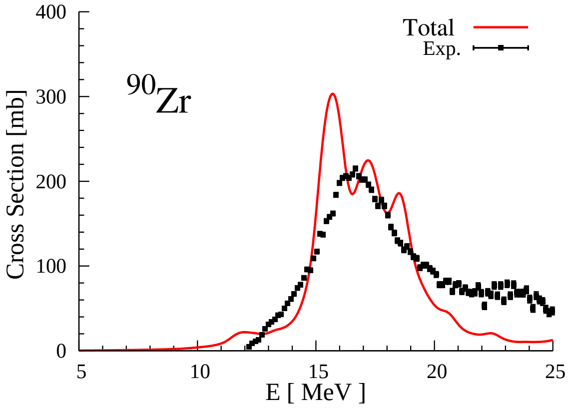

Figure 4.24: Photo-nuclear reaction cross sections for ^{90}Zr. Experimental data (symbols) are taken from Ref. [71]. The smoothing parameter of $\Gamma = 1$ MeV is used for the calculations.

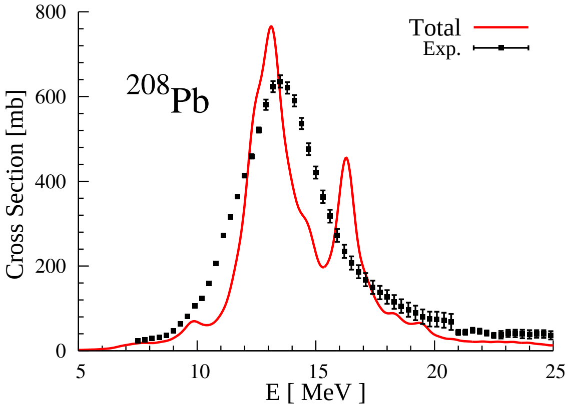

Figure 4.25: Photo-nuclear reaction cross sections for ^{208}Pb. Experimental data (symbols) are taken from Ref. [72]. The smoothing parameter of $\Gamma = 1$ MeV is used for the calculations.

is separated peak in ^{152,154}Sm. We must note that the results of ^{148,150}Sm do not have high accuracy in low-energy region. This is because it is very difficult with high accuracy to solve the real-time calculation for ^{148,150}Sm which have some local minimums around true ground state. In future work, we need to improve solving a true ground state in any case.

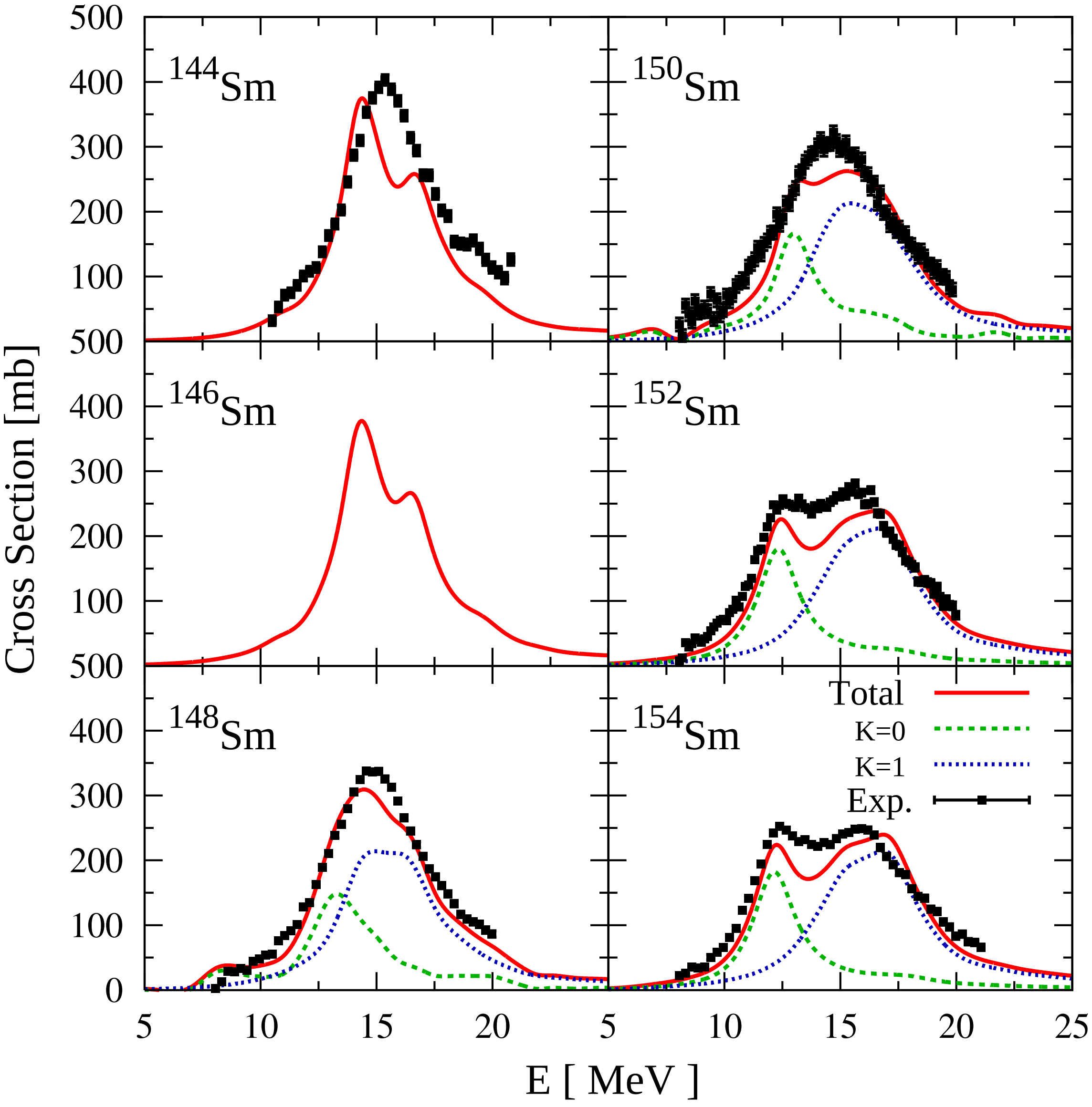

Figure 4.26: Photo-nuclear reaction cross sections for $^{144-154}$Sm. In each panels, solid, dashed and dotted lines indicate Cb-TDHFB calculation results with smoothing parameter $\Gamma = 2$ MeV, and black points and error bar indicate experimental data taken from [73].

4.6 Pygmy resonance (C,O,Ne,Mg,Si,S,Ar,Ca isotopes)

In this section, we focus on the low-energy $E1$ strength which is often called pygmy dipole resonance (PDR). The PDR is the one of hot topics in nuclear physics. There are two major reasons on the PDR. One of the reason is a special structure of PDR which is indicated as a new collective motion in neutron-rich nuclei, but has not been clarified. The other reasons is the role of PDR for nucleosynthesis. The PDR has big effects for (γ, n) cross section which is important for r-process [42, 43]. So, we discuss the appearance of the low-energy $E1$ strengths with using the data of our systematic calculations. The ground state information and total $E1$ strength distribution [1] of nuclei presented in this section, print to Appendix A, because a number of the nuclei is near 80, it is so large. In order to investigate how the low-energy pygmy strength changes with increasing the neutron number, we define the low-energy $E1$ ratio by $m_1(E_c)/m_1$ with $E_c = 10$ MeV, where

$$m_1(E) \equiv \int_0^E E' S(E'; E1) dE', \tag{4.3}$$

and $m_1 \equiv m_1(\infty)$. Fig. 4.27 shows the part of strength related with this ratio for ^{26}Ne. The filled part is defined as "low-energy" part in this study of course, we need to confirm the justification of this definition, but this definition gives us reasonable aspects of systematic low-energy $E1$ strength at later reader can see[2]. This low-energy peak structure has been recently measured at RIKEN [76]. The calculated pygmy position is around $8 - 9$ MeV, which agrees with experimental data[76] and with the other QRPA calculations[77, 55]. The ratio is shown for calculated even-even C, O, Ne, Mg, Si, S, Ar and Ca isotopes on some figures in this section.

First, we mention the ratio defined by (4.3) for C and O isotopes. Fig. 4.28 shows the ratios for C and O isotopes as function of neutron number, and Fig. 4.30 shows the ratio for C and O isotopes as function of the difference between root mean square radii ($R_{\mathrm{r.m.s}}$) of neutron and proton density distribution. In order to evaluate the width of neutron-skin, we use the difference of $R_{\mathrm{r.m.s}}$ in Fig. 4.30. In each Fig. 4.28 and 4.30, solid lines indicate the results of Cb-TDHFB calculation and dotted lines indicate the results of HF+RPA calculation produced by FAM [59, 66]. Cross symbols show the results for C isotopes and filled circle symbols show the results for O isotopes. These all HF+RPA calculations in this section are results of T.Inakura. We must note that a computational space of this HF+RPA is lager than our space, they use also the spherical box represented three-dimensional coordinate but their radius of the box is 15 fm. Some effects from this difference of space-size occur in the case of heavier nuclei. If we meet the effect, we mention it. We discuss Fig. 4.28. We can see in both the ratio of C and O isotopes, abrupt jumps between $N = 14$ and 16. This jump between $N = 14$ and 16 seems to be due to occupation of neutron $s_{1/2}$ orbital. In the poor-neutron region, the ratio is also increasing, it indicates the pygmy resonance produced by proton-rich nuclei, but we do not mention the detail of the appearance because our results for proton-rich side are not enough to discuss the dependence on proton number. So, we only mention that there is the appearance

---

[1] $E1$ strength distribution is equivalent to the strength function of isovector dipole mode.

[2] Basically, we know that PDR appears around a separation energy [76], then we expect that the strengths appear around a separation energy which can be evaluate with Bethe-Weisäcker mass formula [25, 75], so the average of separation energy is around 8.5 MeV. We do not have other significant reason for this 10 MeV choice.

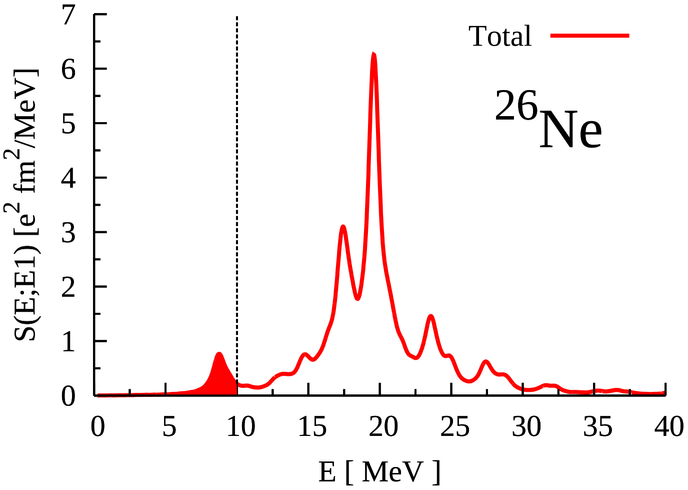

Figure 4.27: $E1$ strength distribution for ^{26}Ne, the ground state of ^{26}Ne is spherical and HF+BCS state with Δ_p =0.0 and Δ_p =1.0 MeV. The black dotted line indicates the threshold defined as "low-energy" in this study.

of low-energy $E1$ strength in proton-rich nuclei also. There is a jump between $N = 6$ and 8 on only C isotopes. We can expect that the reason for the jump is occupation of $p_{1/2}$ orbital. We can see the almost constant ratio in $N = 10 - 14$. This slow down of a increasing the ratio is caused by start to occupy $d_{3/2}$ orbital. We can interpret the effect of $d_{3/2}$ orbital for the ratio, as that the occupation of $d_{3/2}$ orbital increase the total energy weighted sum (EWS), but does not contribute for the low-energy $E1$ strength. We have discussed the ratio of pygmy resonance with the orbitals defined in spherical mean field, however C isotopes of $N = 10 - 14$ are all deformed nucleus and it is difficult to separate GDR and PDR, so we can not confirm that it is enough or not to explain the pygmy resonance with the orbitals. Fig. 4.30 is also a trial in order to interpret the appearance of PDR as function of neutron-skin width, this trial is similar to [78]. Actually, the ratio is in proportion to the width of neutron-skin has linear relation roughly. We can see the relation between the constant ratio of C isotopes and the changes of the neutron-skin width. In $N = 10 - 14$, the changes of the width are less than other neutron number. From comparison with HF+RPA calculations, There is no remarkable effects of the pairing correlation on the low-energy $E1$ strength for C and O isotopes.

Next, we show the ratios for Ne and Mg isotopes with Fig. 4.29 and 4.31. Fig. 4.29 shows the ratio as function of neutron number and Fig. 4.31 shows that as function of difference between $R_{\mathrm{r.m.s}}$ of neutron and proton. In each Fig. 4.29 and 4.31, solid lines indicate the results of Cb-TDHFB calculation and dotted lines indicate the results of HF+RPA calculation produced by FAM [59, 66]. Filled triangle symbols show the results for Ne isotopes and filled square symbols show the results for Mg isotopes. In Fig. 4.29, we can see abrupt jumps between $N = 14$ and 16, and between $N = 20$ and 22 on Ne and Mg isotopes. The first jump between $N = 14$ and 16 seems to be due to occupation of neutron $s_{1/2}$ orbital. In contrast, the second jump between $N = 20$ and 22 may be due to the onset of the deformation and the neutron pairing. The second jump can not be seen in HF+RPA calculations. The ground states of Ne and Mg isotopes with $N = 16, 18, 20$ are spherical and then, those with $N = 22, 24, 26, 28$ are deformed in our HF+BCS calculation. But, HF calculation yields the ground state with some deformation for Ne and Mg isotopes in $N = 16, 18, 20$. The pairing correlation affects the ratio of the low-energy $E1$ strength through the properties of ground state. In Fig. 4.31, we can not see the effects of pairing correlation for the ratio. The picture of the ratio with the difference of $R_{\mathrm{r.m.s}}$ masks a information of nuclear shape, but we can see the same proportional relation on the results of Ne and Mg isotopes with this picture.

Next, we show the ratios for Si and S isotopes with Fig. 4.32 and 4.34. Fig. 4.32 shows the ratio as function of neutron number and Fig. 4.34 shows that as function of difference between $R_{\mathrm{r.m.s}}$ of neutron and proton. In each Fig. 4.32 and 4.34, solid lines indicate the results of Cb-TDHFB calculation and dotted lines indicate the results of HF+RPA calculation presented by FAM. Filled diamond symbols show the results for Si isotopes and filled pentagon symbols show the results for S isotopes. The pairing correlation affects strongly the behavior of the ratio of Si and S isotopes. In the Fig. 4.32, the ratio of Si isotopes increase gently from $N = 14$ to 30 in both HF+RPA and Cb-TDHFB calculations. There is a small jump between $N = 28$ and 30 in Cb-TDHFB calculation. This small jump is caused by changing the shape of Si isotope of $N = 30$ to spherical. In contrary on the S isotopes, there is a big difference between the results of HF+RPA and Cb-TDHFB calculation. The HF+RPA calculation indicates an abrupt jump between $N = 28$ and 30, but the Cb-TDHFB calculation shows the smooth increase of the ratio for S isotopes from $N = 16$ to 34. The jump between $N = 28$ and 30 in HF+RPA calculation seems to be due to occupation of neutron $p_{3/2}$ orbital, the smooth increase in Cb-TDHFB calculation is caused the pairing correlation which can describe the continuous occupation probabilities around $N = 28$. In the Fig. 4.34, the relation between the ratio and difference of $R_{\mathrm{r.m.s}}$ is not proportional but parabolic relation. We can not see the effects of pairing correlation for the ratio in this Fig. 4.34 except for result of magic number.

Next, we show the ratios for Ar and Ca isotopes with Fig. 4.33 and 4.35. Fig. 4.33 shows the ratio as function of neutron number and Fig. 4.35 shows that as function of difference between $R_{\mathrm{r.m.s}}$ of neutron and proton. In each Fig. 4.32 and 4.34, solid lines indicate the results of Cb-TDHFB calculation and dotted lines indicate the results of HF+RPA calculation presented by FAM. Filled anti-triangle symbols show the results for Ar isotopes and star symbols show the results for Ca isotopes. In the Fig. 4.33, there are some effects of pairing correlation in the behavior of the ratio of Ar isotopes. The smooth increase of the ratio appears in Ar isotopes similarly with results of Si and S isotopes. We can expect that the reason is also the continuous occupation probability of orbitals, namely the effects of pairing correlation. For Ca isotopes, there is no remarkable difference between the results of HF+RPA and Cb-TDHFB calculation. There is an abrupt jump between $N = 28$ and 30 in both calculations. This jump between $N = 28$ and 30 seems to be due to occupation of neutron $p_{3/2}$ orbital. The results of Cb-TDHFB calculation behave same as results of HF+RPA calculation around $N = 28$, because the pairing correlation does not work at $N = 28$. There is a slow down of the increase of the ratio of low-energy $E1$ strength from Ca isotope with $N = 34$. This is expected to due to the occupation of $f_{5/2}$ orbitals. These aspects are similar to the case of C isotopes with $N = 10, 12, 14$. In this Ca isotopes case, the occupation of $f_{5/2}$ orbital increase the total EWS, but does not contribute for the low-energy $E1$ strength. Namely, the denominator part of (4.3) become large, but the numerator part of that increase a few, so the ratio does not increase. The space-size effects appear in these Ca isotopes with over $N = 34$. The ratio decrease from $N = 36$ in Cb-TDHFB results but this reason is the space-size effects that become difficult to separate between GDR and PDR. Fig. 4.35 indicates that $f_{5/2}$ orbital does not contribute to $R_{\mathrm{r.m.s}}$, the spacing of the symbols becomes small from $N = 34$. In addition, there is a proportional relation between the ratio and the difference of $R_{\mathrm{r.m.s}}$ only while low angular momentum orbitals are occupied.

We summarize the important things for the appearance of low-energy $E1$ strength from the above discussion about the results of C, O, Ne, Mg, Si, S, Ar and Ca isotopes. When the low angular momentum orbital as like s or p orbital are occupied on the unstable nuclei, the low-energy $E1$ strength appears. The ratio defined by (4.3) is sensitive to the neutron number especially around magic number, and the behavior of the ratio reflects the properties of nuclear shape. The most effect of pairing correlation for the appearance is continuous occupation probabilities of orbitals around magic number, and there is the effect of paring for the appearance through the change of ground state. Pairing is also important to define the shape of nucleus. In addition, we proposed the ratio of low-energy $E1$ strength, and try to investigate the appearance with neutron number and difference between the $R_{\mathrm{r.m.s}}$ of neutron and proton density. The picture of the ratio with neutron number is good for reflection of orbital and nuclear shape properties. In contrary, the picture with the difference of $R_{\mathrm{r.m.s}}$ gives simple aspects for a relation between the appearance and nucleon-skin width, but only when around magic number.

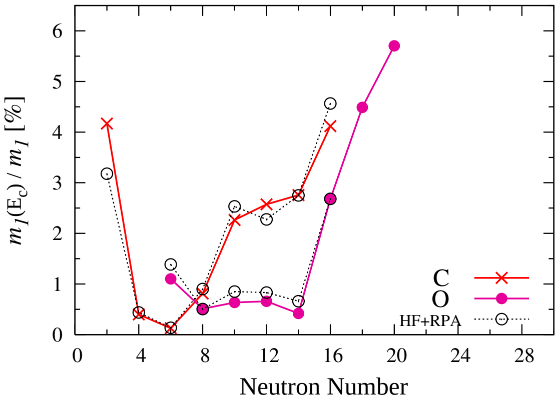

Figure 4.28: The ratio defined as Eq.(4.3) as function of neutron number for C and O isotopes. Solid line indicates the results of Cb-TDHFB calculation, dotted line indicates the results of HF+RPA calculation produced by FAM based on [59, 66]. Cross symbols show the results for C isotopes and filled circle symbols show the results for O isotopes.

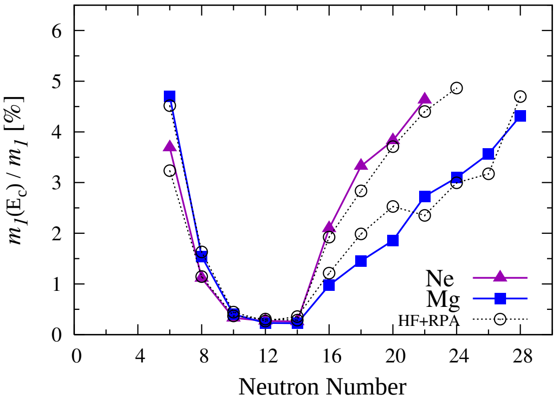

Figure 4.29: The ratio defined as Eq.(4.3) as function of neutron number for Ne and Mg isotopes. The meanings of the lines are same as Fig. 4.28. Filled triangle symbols show the results for Ne isotopes and filled square symbols show the results for Mg isotopes.

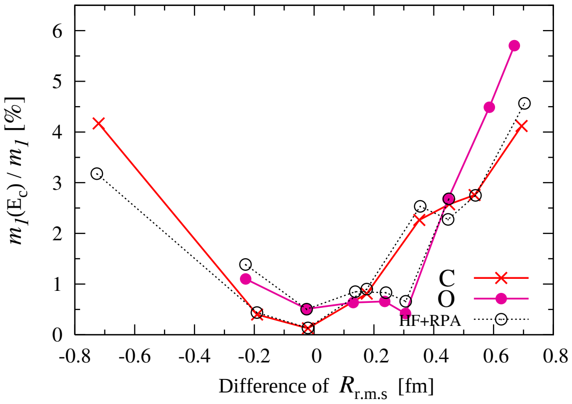

Figure 4.30: The ratio defined as Eq.(4.3) as function of difference between $R_{\text{r.m.s}}$ of neutron and proton density for C and O isotopes. The meanings of the lines are same as Fig. 4.28. Cross symbols show the results for C isotopes and filled circle symbols show the results for O isotopes.

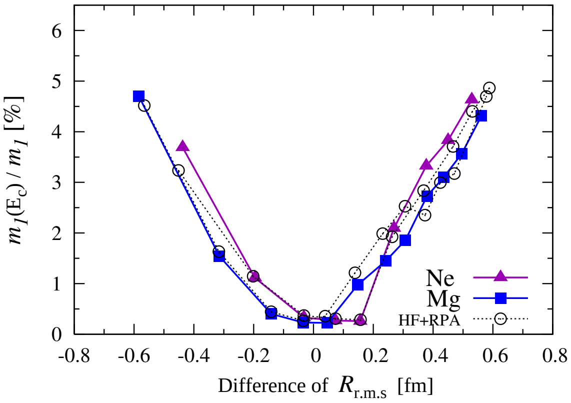

Figure 4.31: The ratio defined as Eq.(4.3) as function of difference between $R_{\text{r.m.s}}$ of neutron and proton density for Ne and Mg isotopes. The meanings of the lines are same as Fig. 4.28. Filled triangle symbols show the results for Ne isotopes and filled square symbols show the results for Mg isotopes.

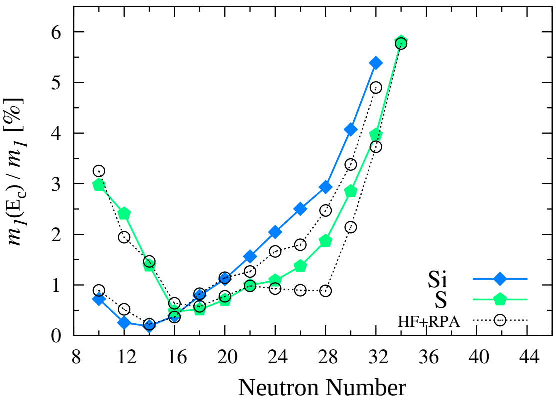

Figure 4.32: The ratio defined as Eq.(4.3) as function of neutron number for Si and S isotopes. The meanings of the lines are same as Fig. 4.28. Filled diamond symbols show the results for Si isotopes and filled pentagon symbols show the results for S isotopes.

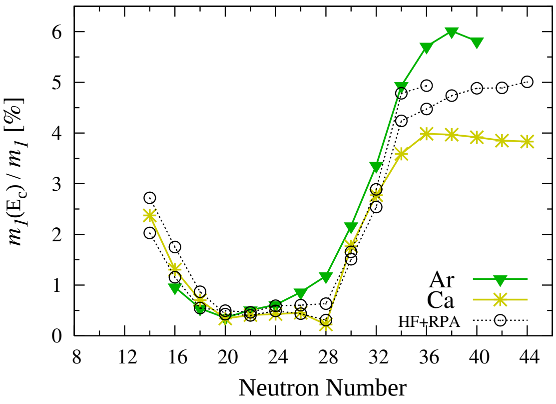

Figure 4.33: The ratio defined as Eq.(4.3) as function of neutron number for Ar and Ca isotopes. The meanings of the lines are same as Fig. 4.28. Filled anti-triangle symbols show the results for Ar isotopes and star symbols show the results for Ca isotopes.

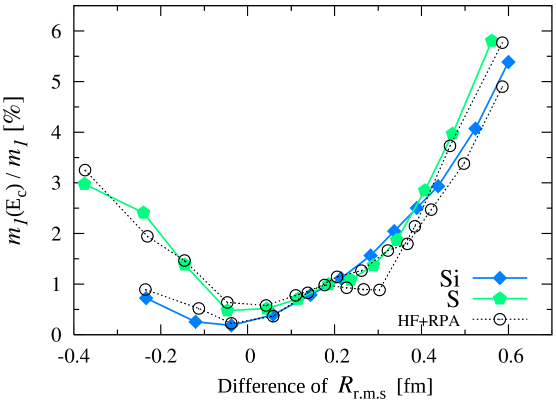

Figure 4.34: The ratio defined as Eq.(4.3) as function of difference between $R_{\mathrm{r.m.s}}$ of neutron and proton density for Si and S isotopes. The meanings of the lines are same as Fig. 4.28. Filled diamond symbols show the results for Si isotopes and filled pentagon symbols show the results for S isotopes.

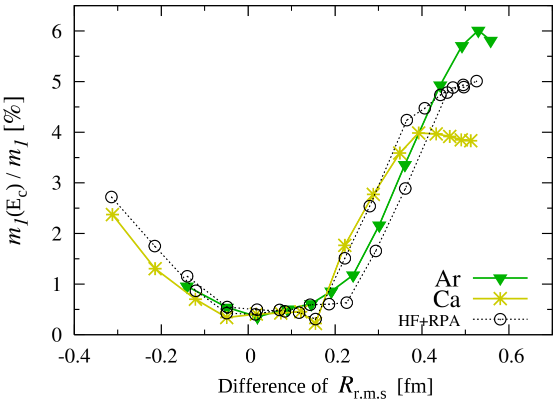

Figure 4.35: The ratio defined as Eq.(4.3) as function of difference between $R_{\mathrm{r.m.s}}$ of neutron and proton density for Ar and Ca isotopes. The meanings of the lines are same as Fig. 4.28. Filled anti-triangle symbols show the results for Ar isotopes and star symbols show the results for Ca isotopes.

Chapter 5

Summary and Future work

We have developed a new theory to study excited states and dynamics of atomic nuclei, which we call the Canonical-basis time-dependent Hartree-Fock-Bogoliubov (Cb-TDHFB). The Cb-TDHFB is a simplified theory of the full TDHFB theory, treating pairing energy functional with a BCS-like approximation. Implementing the theory with a real-space and real-time method, we can describe nuclear excitations and dynamics taking account of deformation effects and pairing correlations, even for heavy nuclei with a reasonable computational costs. In the thesis, we first presented a derivation of the Cb-TDHFB theory and its practical implementation. We then presented examples of the linear response calculations using the Cb-TDHFB theory.

In Chapter 2, we derived the Cb-TDHFB equations starting with the full TDHFB equations, introducing a simplified form for the pairing energy functional. In the derivation, we start with the ordinary TDHFB equation written in the time-dependent normal density matrix $\rho(t)$ and the pairing tensor $\kappa(t)$. We then rewrite the equation in the canonical basis, which diagonalize $\rho(t)$. The derived TDHFB equation in the canonical basis has a very simple form. However, it is not useful practically for a general case since it costs much to obtain the canonical basis itself at each time. Solving the time-dependent equation for the canonical basis is as difficult as solving the full TDHFB equation. This difficulty disappears if we employ a simplified pairing energy density functional, which is equivalent to that employed in the BCS approximation for ground state calculations. With the simplified pairing functional, the evolution equation for the time-dependent canonical-basis function becomes nothing but that of time-dependent Hartree-Fock (TDHF) so that the computational cost of Cb-TDHFB is almost the same as that of TDHF calculation.

In Chapter 3, we shown the concrete form of pairing functional, the relation strength function with linear response and the procedure of linear-response calculation with time-dependent scheme. We explained also the detail and setup of numerical calculation in present study.

In Chapter 4, we presented results of the Cb-TDHFB calculations for excited states of some spherical and deformed nuclei to show performance of the method.

In Section 4.3, we showed strength functions of isovector dipole and isoscalar quadrupole excitations for some spherical and deformed nuclei. In the isoscalar quadrupole response, there appear Q_{20}- and Q_{22}-vibrational modes which converge into a single identical mode in the spherical limit. In prolate nuclei, the excitation energy of the Q_{20}-vibration is lower than that of

Q_{22}-vibration, while opposite in the oblate nuclei. The pairing correlation effect is rather weak for the isoscalar quadrupole excitations in spherical nuclei. In deformed superfluid nuclei, the Q_{20}-vibrational mode induces the pair vibrational mode, while the Q_{22}-vibrational mode does not. This is because the K-quantum number is a good quantum number in axially symmetric nuclei and the pairing correlation is coupled with $K = 0$ mode of isoscalar quadrupole model.

In Section 4.1, we next compared results of Cb-TDHFB calculation with those of HFB+QRPA which is equivalent to the small amplitude limit of the full TDHFB. We compared our results with axially-symmetric deformed HFB+QRPA calculations for isoscalar quadrupole excitations of neutron-rich magnesium isotope ^{34}Mg. Our calculation show a good agreement with existing HFB+QRPA calculations. However, we observed a substantial difference for the height of lowest peak. We consider that this difference for the lowest peak is caused by the difference of the pairing energy functionals.

In Section 4.2, our calculation is achieved fully self-consistent, employing the same energy functional as that in the ground state. We mentioned the importance of the self-consistency in our Cb-TDHFB calculation. We confirm the accuracy of our time-dependent scheme by comparing our results with other fully self-consistent calculation performed with the finite amplitude method (FAM) for isovector dipole excitation of ^{24}Mg. Furthermore, we found that there are some differences in the effects of the spin-orbit and Coulomb residual interactions for each excitation mode. These residual interactions are found to shift the peak energies of isoscalar giant quadrupole resonance to higher energy region and to move low-energy peaks to lower energy region simultaneously. The effect of Coulomb residual interaction is rather weak for the isoscalar quadrupole strength distribution. In isovector dipole excitation, the spin-orbit residual interaction shifts the peak position of the isovector giant dipole response to higher energy region. However, the effect is much weaker than that in the isoscalar quadrupole case. The effect of residual Coulomb force is again very small for isovector dipole excitation of ^{24}Mg. We also examined the significance of the full self-consistency for the isovector dipole strength functions of heavy nuclei taking ^{208}Pb and ^{154}Sm nuclei as examples. The effect of the spin-orbit residual interaction was found to be significant for ^{208}Pb as in the case of ^{24}Mg. The effect of Coulomb residual interaction is found to be much larger in the heavy nuclei.

In Section 4.4, in order to assess the computational cost of our Cb-TDHFB approach, we achieved calculations of ^{172}Yb and compared our computational costs with those by J. Terasaki and J. Engel who achieved a fully self-consistent HFB+QRPA calculations for axially deformed nuclei. The calculated isovector dipole strengths for ^{172}Yb coincide each other with high accuracy. Terasaki and Engel reported that their computational cost was about 136,000 CPU hours in the parallel computation with 10,000 CPU. In our calculation, we need only 300 CPU hours in a single processor. We also achieved calculations for $^{236-240}$U. It costs 400 CPU hours, showing approximately linear scaling for the mass number. We also note that the calculated spectra agree well with measurements. Thus, we may conclude that the Cb-TDHFB method shows a quite nice aspect in the computational costs and in the feasibility for large nuclei.

In Section 4.5, we next compared results of Cb-TDHFB calculation with experimental data for photo-nuclear reaction cross section. We calculated the photo-nuclear reaction cross section of ^{16}O, ^{24,26}Mg, ^{40}Ca, ^{90}Zr, ^{208}Pb and Sm isotopes. From the results of ^{16}O, ^{24,26}Mg, and ^{40}Ca, we saw that our results underestimate the experimental data. This is a properties of the calculation with Skyrme interaction which has been also reported by T.Inakura. But in heavy nuclei (^{90}Zr, ^{208}Pb), the calculation results become to agree well with the experimental data for the centroid energy. In Sm isotopes, we could see the shape transitional properties with increasing neutron number from 82 to 92 in both experimental data and calculation results. ^{144,146}Sm are spherical, but from ^{148}Sm, the isotopes are gradually becoming prolate shape with respect to neutron number. Then, experimental data has one concentrated giant resonance peak in ^{144,146}Sm, but from ^{148}Sm, the peak are becoming wide and at last becomes separated one at ^{152,154}Sm.

In Section 4.6, we presented an application of our approach for low-energy isovector dipole ($E1$) strength distribution below 10 MeV. In the low-energy $E1$ response, it has been well known that there appears the so-called pygmy resonance. There are two major interests on the pygmy resonance. It may be regarded as a new kind of collective excitations which appear in neutron-rich nuclei. It may also affect the (n, γ) cross section which is important in nucleosynthesis.

Recently, systematic calculations of the $E1$ strength function has been achieved in the Hartree-Fock plus RPA (HF+RPA) approach. Although the HF+RPA approach does not include pairing correlation effect, it has brought an interesting result for the systematic behavior of the low-energy $E1$ strength distribution. Namely, the appearance of the low-energy $E1$ strength is intimately related to the occupation of the low partial wave orbitals such as s and p orbitals. We have made a similar systematic calculation and investigated the effect of the pairing correlation.

In Carbon ($Z = 6$) and Oxygen ($Z = 8$) isotopes, the low-energy $E1$ strengths are found to increase in the neutron-rich isotopes when the neutron number exceeds $N = 16$. Since neutron occupies $s_{1/2}$ orbital for $N = 16$ and more nuclei, it is considered that the occupation of the $s_{1/2}$ orbital is the origin of the low-energy $E1$ strength. This result suggests that the appearance of the pygmy resonance is intimately related to the occupation of low angular momentum orbitals. We also find a rise of the low-energy $E1$ strength at $N = 8$ for Carbon isotopes while it is almost constant for isotopes in $N = 10 - 14$. The increase at $N = 8$ is considered to be caused by the occupation of $p_{1/2}$ orbital. In Neon ($N = 10$) and Magnesium ($Z = 12$) isotopes, we again find that the low-energy $E1$ strengths increase beyond $N = 16$. We consider that it originates from the occupation of $s_{1/2}$ orbital, as in the Carbon and Oxygen isotopes. For these isotopes, we find a significant effect of the pairing correlation through the change of the ground state deformation. In our approach, the ground state calculation is achieved by the HF+BCS theory. In the HF+BCS theory, the ground state of Ne and Mg isotopes with neutron number $N = 16 - 20$ are all spherical. The ground states are deformed for neutron number $N \geq 22$. However, in the previous HF+RPA calculation, isotopes with $N = 16 - 20$ are deformed since the pairing correlation is not included. Our calculation shows a small but abrupt increase of the low-energy $E1$ strength at $N = 22$ reflecting the appearance of the deformation, which the previous HF+RPA calculation does not. For Silicon ($Z = 14$) and Sulfur ($Z = 16$) isotopes, the pairing effect on the low-energy $E1$ strength becomes more appreciable. In the HF+RPA calculation showed an abrupt increase of the low-energy $E1$ strength at $N = 30$, which is caused by the occupation of the $p_{3/2}$ orbital. However, in our Cb-TDHFB calculation, the change is rather smooth reflecting a continuous change of the $p_{3/2}$ occupation. In the cases of Argon ($Z = 18$), the change of low-energy $E1$ strength is also rather smooth reflecting a continuous change of the $p_{3/2}$ occupation. But in Calcium ($Z = 20$) isotopes, an abrupt increase of the low-energy $E1$ strength appeared at $N = 30$ in our Cb-TDHFB calculation also, because the pairing does not work for ^{48}Ca which is a double magic nucleus. The low-energy $E1$ strength of calcium isotopes show a special character from $N = 36$ which can be expected effects of $f_{5/2}$ orbital. The increase of the low-energy $E1$ strength becomes slow down. It is supposed that the $f_{5/2}$ orbital does not contribute to the low-energy $E1$ strength.

Finally, we mention a future direction of the present work. We consider that there are two directions which the present Cb-TDHFB approach will be of significance. One is the systematic investigation of the nuclear response properties for a whole mass region. The other is an application towards large amplitude collective motion such as fusion and fission dynamics.

In the present thesis, we have reported an investigation of the photo-nuclear reactions of neutron-rich nuclei up to $Z = 20$. The photo-nuclear reaction cross sections of nuclei heavier than Iron ($Z = 26$) are significant since they are crucial to understand the nucleosynthesis in the r-process.

Regarding the large amplitude collective motion, the present Cb-TDHFB approach will allow us to investigate the effect of pairing correlation. Microscopic descriptions of the large amplitude collective motion such as fusion and fission phenomena have been a long-standing issue in nuclear theory. The fusion and fission dynamics are important not only in fundamental sciences but also applications such as nuclear energy generation and transmutation of radioactivity. In order to execute these studies, we consider the present Cb-TDHFB theory provides a promising starting point. In view of rapid development of computational techniques, parallel computations with massively parallel supercomputer will be a key issue to realize the above mentioned studies.

Acknowledgement

I would like to express my gratitude to Prof. T.Nakatsukasa and Prof. K.Yabana for patient guidance, encouragements and supports during my study. I would like to express my acknowledgments to Prof. Y.Hashimoto for his continuous discussion as one of my collaborators. I would like to thank Dr. T.Inakura and Dr. K.Yoshida for their useful advice as my collaborators.

I am also grateful to Prof. K.Matsuyanagi, Prof. J.A.Maruhn, Prof. D.Lacroix, Prof. J.Dobaczewski and Prof. V.Oberacker for their encouragements for my study. I want to express my deep appreciation to my colleagues in Theoretical Nuclear Group in University of Tsukuba, and my colleagues in Theoretical Nuclear Physics Laboratory RIKEN Nishina Center.

The numerical calculations were performed on the computers in Theoretical Nuclear Group of University of Tsukuba.

Finally but not least, I would like to express to thank my families for their understanding, supports and encouragements to me in all time.

Appendixes

A Data Table and $E1$ strength distributions

This section presents the ground state data and $E1$ strength distributions in this study. Following tables show data of ground state: total energy E_{Total}, numbers of canonical orbitals for neutrons and protons Orbitals (n, p), quadrupole deformation parameters (β, γ), pairing gaps (3.7) for neutrons and protons (Δ_n, Δ_p), chemical potentials for neutrons and protons (λ_n, λ_p). In the case of normal phase $(\Delta = 0)$, we define the chemical potential as the single-particle energy of the highest occupied orbital, $\lambda_n = \epsilon^0_N$ and $\lambda_p = \epsilon^0_Z$, and the number of used orbitals is the same of particle number for instance that in the case of ^{16}C, it has $(16, 10)$ canonical orbitals but with no pairing gap of neutron, practically, we use $(16, 6)$ orbitals in which proton orbitals are equivalent to HF single-particle states. The $(16, 10)$ orbitals are obtained only in our cut-off energies Eq.(3.3). The total energy E_{Total}, pairing gap energy Δ and chemical potential λ are given in units of MeV.

A.1 Ground state of Carbon $(Z = 6)$ isotopes

	$-\mathrm{E}_{\mathrm{Total}}$	Orbitals (n, p)	β	γ	Δ_n	Δ_p	$-\lambda_n$	$-\lambda_p$
^{8}C	31.153	(6, 6)	0.0	–	0.0	0.0	31.21	2.96
^{10}C	62.339	(10, 6)	0.22	0°	0.0	0.0	17.00	7.85
^{12}C	93.567	(8, 8)	0.0	–	0.0	0.0	16.81	14.07
^{14}C	108.606	(16, 8)	0.0	–	0.0	0.0	8.94	18.23
^{16}C	115.600	(16, 10)	0.14	0°	0.99	0.0	4.55	21.22
^{18}C	122.596	(16, 10)	0.27	0°	0.57	0.0	3.90	23.70
^{20}C	128.954	(16, 8)	0.23	60°	0.0	0.0	4.84	27.53
^{22}C	133.426	(16, 8)	0.0	–	0.0	0.0	3.41	30.24

A.2 Ground state of Oxygen ($Z = 8$) isotopes

	$-\mathrm{E}_{\mathrm{Total}}$	Orbitals (n, p)	β	γ	Δ_n	Δ_p	$-\lambda_n$	$-\lambda_p$
^{14}O	102.805	(8, 14)	0.0	–	0.0	0.0	20.81	5.68
^{16}O	127.942	(16, 14)	0.0	–	0.0	0.0	13.53	10.25
^{18}O	142.569	(16, 14)	0.0	–	1.05	0.0	7.94	13.90
^{20}O	156.168	(16, 14)	0.0	–	1.10	0.0	7.45	17.34
^{22}O	169.172	(16, 14)	0.0	–	0.0	0.0	8.06	20.65
^{24}O	178.613	(20, 14)	0.0	–	0.0	0.0	5.17	22.62
^{26}O	179.703	(20, 14)	0.0	–	0.8	0.0	1.13	24.87
^{28}O	180.673	(20, 14)	0.0	–	0.0	0.0	1.78	27.05

A.3 Ground state of Neon ($Z = 10$) isotopes

	$-\mathrm{E}_{\mathrm{Total}}$	Orbitals (n, p)	β	γ	Δ_n	Δ_p	$-\lambda_n$	$-\lambda_p$
^{16}Ne	102.421	(10, 12)	0.25	0°	0.0	0.54	23.05	0.91
^{18}Ne	135.283	(14, 16)	0.22	0°	0.0	1.07	17.15	4.00
^{20}Ne	157.672	(16, 16)	0.37	0°	0.0	0.0	13.07	9.18
^{22}Ne	178.516	(20, 16)	0.37	0°	0.0	0.0	11.03	12.38
^{24}Ne	195.051	(20, 16)	0.17	60°	0.0	0.74	10.57	13.03
^{26}Ne	208.529	(20, 16)	0.0	–	0.0	1.00	7.17	14.92
^{28}Ne	213.884	(20, 16)	0.0	–	0.79	1.01	3.21	17.05
^{30}Ne	219.303	(20, 20)	0.0	–	1.37	1.01	2.40	19.08
^{32}Ne	222.944	(24, 16)	0.36	0°	0.95	0.0	2.15	23.60

A.4 Ground state of Magnesium ($Z = 12$) isotopes

In ^{26}Mg, the ground state of HF and HF+BCS are indicated in order to express the remarkable effect of pairing. Pairing changes the shape of ^{26}Mg from prolate to oblate.

	$-\mathrm{E}_{\mathrm{Total}}$	Orbitals (n, p)	β	γ	Δ_n	Δ_p	$-\lambda_n$	$-\lambda_p$
^{18}Mg	101.562	(10, 16)	0.31	0°	0.0	0.0	25.59	0.20
^{20}Mg	140.702	(14, 16)	0.0	–	0.0	1.13	20.53	2.83
^{22}Mg	169.987	(16, 20)	0.38	0°	0.0	0.0	16.305	6.42
^{24}Mg	197.299	(20, 20)	0.39	0°	0.0	0.0	14.11	9.50
^{26}Mg-$_{\mathrm{HF}}$	217.879	(14, 12)	0.24	8°	0.0	0.0	11.37	11.67
^{26}Mg-$_{\mathrm{BCS}}$	217.945	(22, 16)	0.20	54°	0.0	0.86	13.08	11.27
^{28}Mg	235.542	(28, 16)	0.0	–	0.0	1.03	9.21	13.29
^{30}Mg	246.237	(28, 16)	0.0	–	1.31	1.03	5.48	15.48
^{32}Mg	255.205	(28, 16)	0.0	–	0.0	1.03	5.82	17.54
^{34}Mg	264.071	(28, 20)	0.37	0°	1.45	0.0	4.11	20.17
^{36}Mg	270.395	(28, 20)	0.33	0°	1.43	0.0	3.21	21.95
^{38}Mg	275.459	(30, 20)	0.30	0°	1.47	0.0	2.37	23.68
^{40}Mg	278.420	(30, 20)	0.29	0°	0.91	0.0	1.31	35.27

A.5 Ground state of Silicon ($Z = 14$) isotopes

	$-\mathrm{E}_{\mathrm{Total}}$	Orbitals (n, p)	β	γ	Δ_n	Δ_p	$-\lambda_n$	$-\lambda_p$
^{24}Si	176.693	(16, 18)	0.182	60°	0.71	0.0	16.93	5.25
^{26}Si	208.177	(16, 24)	0.20	52°	0.85	0.0	15.88	7.68
^{28}Si	237.846	(18, 20)	0.23	60°	0.0	0.0	15.71	10.35
^{30}Si	259.619	(28, 20)	0.0	–	0.0	0.0	11.25	12.74
^{32}Si	274.482	(32, 20)	0.0	–	1.31	0.0	7.63	14.91
^{34}Si	287.935	(32, 20)	0.0	–	1.63	0.0	6.56	16.94
^{36}Si	299.363	(32, 20)	0.0	–	2.15	0.0	5.61	18.81
^{38}Si	309.073	(32, 20)	0.09	8°	2.217	0.0	4.95	19.82
^{38}Si	309.122	(32, 22)	0.12	60°	2.23	0.0	5.00	20.16
^{40}Si	317.662	(32, 22)	0.17	60°	2.03	0.0	4.34	21.82
^{42}Si	324.681	(32, 22)	0.19	60°	1.55	0.0	3.39	23.40
^{44}Si	330.254	(32, 20)	0.0	–	1.86	0.0	2.60	24.98
^{46}Si	333.798	(34, 20)	0.0	–	1.28	0.0	1.64	26.15

A.6 Ground state of Sulfur ($Z = 16$) isotopes

	$-\mathrm{E}_{\mathrm{Total}}$	Orbitals (n, p)	β	γ	Δ_n	Δ_p	$-\lambda_n$	$-\lambda_p$
^{26}S	179.410	(16, 18)	0.0	–	1.01	0.0	18.62	1.63
^{28}S	214.730	(16, 24)	0.0	–	1.03	0.0	17.84	3.49
^{30}S	248.398	(20, 28)	0.0	–	0.0	0.0	18.06	5.39
^{32}S	275.059	(28, 28)	0.0	–	0.0	0.0	13.16	7.30
^{34}S	294.106	(32, 28)	0.0	–	1.28	0.0	9.61	9.25
^{36}S	311.394	(34, 28)	0.0	–	1.50	0.0	8.35	11.08
^{38}S	326.339	(34, 28)	0.0	–	2.15	0.0	7.34	12.76
^{40}S	339.607	(34, 26)	0.145	0°	2.08	0.0	6.73	14.94
^{42}S	351.682	(34, 26)	0.150	0°	2.07	0.0	5.82	16.65
^{44}S	361.733	(34, 28)	0.11	0°	1.97	0.0	4.87	18.00
^{46}S	369.791	(34, 26)	0.0	–	1.71	0.0	3.97	18.97
^{48}S	375.996	(34, 28)	0.0	–	0.93	0.0	2.77	20.24
^{50}S	380.092	(34, 28)	0.0	–	0.0	1.70	2.21	20.98

A.7 Ground state of Argon ($Z = 18$) isotopes

	$-\mathrm{E}_{\mathrm{Total}}$	Orbitals (n, p)	β	γ	Δ_n	Δ_p	$-\lambda_n$	$-\lambda_p$
^{34}Ar	281.631	(28, 20)	0.0	–	0.0	0.80	15.11	3.25
^{36}Ar	306.247	(28, 28)	0.0	–	1.22	1.26	2.03	5.77
^{38}Ar	328.262	(32, 28)	0.0	–	1.11	1.24	0.48	8.02
^{40}Ar	347.083	(34, 28)	0.0	–	1.99	1.22	9.27	9.93
^{42}Ar	364.247	(34, 28)	0.0	–	2.16	1.20	8.43	11.79
^{44}Ar	379.713	(34, 28)	0.0	–	2.01	1.18	7.61	13.57
^{46}Ar	393.338	(34, 28)	0.0	–	1.78	1.17	6.49	15.19
^{48}Ar	404.114	(36, 28)	0.0	–	1.41	1.15	5.31	16.55
^{50}Ar	414.205	(38, 28)	0.0	–	0.83	2.04	3.95	17.61
^{52}Ar	419.686	(40, 28)	0.0	–	1.20	1.96	2.36	18.75
^{54}Ar	422.555	(40, 28)	0.0	–	1.41	1.85	1.57	20.12

A.8 Ground state of Calcium ($Z = 20$) isotopes

	$-\mathrm{E}_{\mathrm{Total}}$	Orbitals (n, p)	β	γ	Δ_n	Δ_p	$-\lambda_n$	$-\lambda_p$
^{34}Ca	251.438	(20, 20)	0.0	–	0.0	0.0	21.99	1.13
^{36}Ca	286.034	(28, 20)	0.0	–	0.0	0.0	16.91	2.92
^{38}Ca	315.095	(28, 28)	0.0	–	1.19	1.10	14.29	3.64
^{40}Ca	341.559	(32, 28)	0.0	–	0.0	0.0	14.31	7.47
^{42}Ca	364.455	(34, 32)	0.0	–	1.92	0.82	11.09	7.45
^{44}Ca	385.027	(34, 30)	0.0	–	2.05	0.0	10.21	11.12
^{46}Ca	404.074	(34, 30)	0.0	–	1.83	0.0	9.35	12.88
^{48}Ca	420.771	(28, 20)	0.0	–	0.0	0.0	10.41	14.68
^{50}Ca	435.251	(40, 28)	0.0	–	1.46	1.90	6.53	13.76
^{52}Ca	446.220	(50, 28)	0.0	–	1.49	0.0	5.18	16.99
^{54}Ca	455.556	(50, 28)	0.0	–	2.28	0.0	4.26	18.36
^{56}Ca	462.589	(50, 28)	0.0	–	2.45	1.41	3.53	17.49
^{58}Ca	468.144	(50, 30)	0.0	–	2.52	0.0	3.00	21.12
^{60}Ca	473.074	(50, 28)	0.0	–	2.53	0.0	2.54	22.48
^{62}Ca	477.383	(50, 28)	0.0	–	2.52	0.0	2.09	23.81
^{64}Ca	481.223	(50, 28)	0.0	–	2.51	0.75	1.61	22.44

A.9 $E1$ strength distributions of Carbon $(Z = 6)$ isotopes $(N = 2 - 16)$

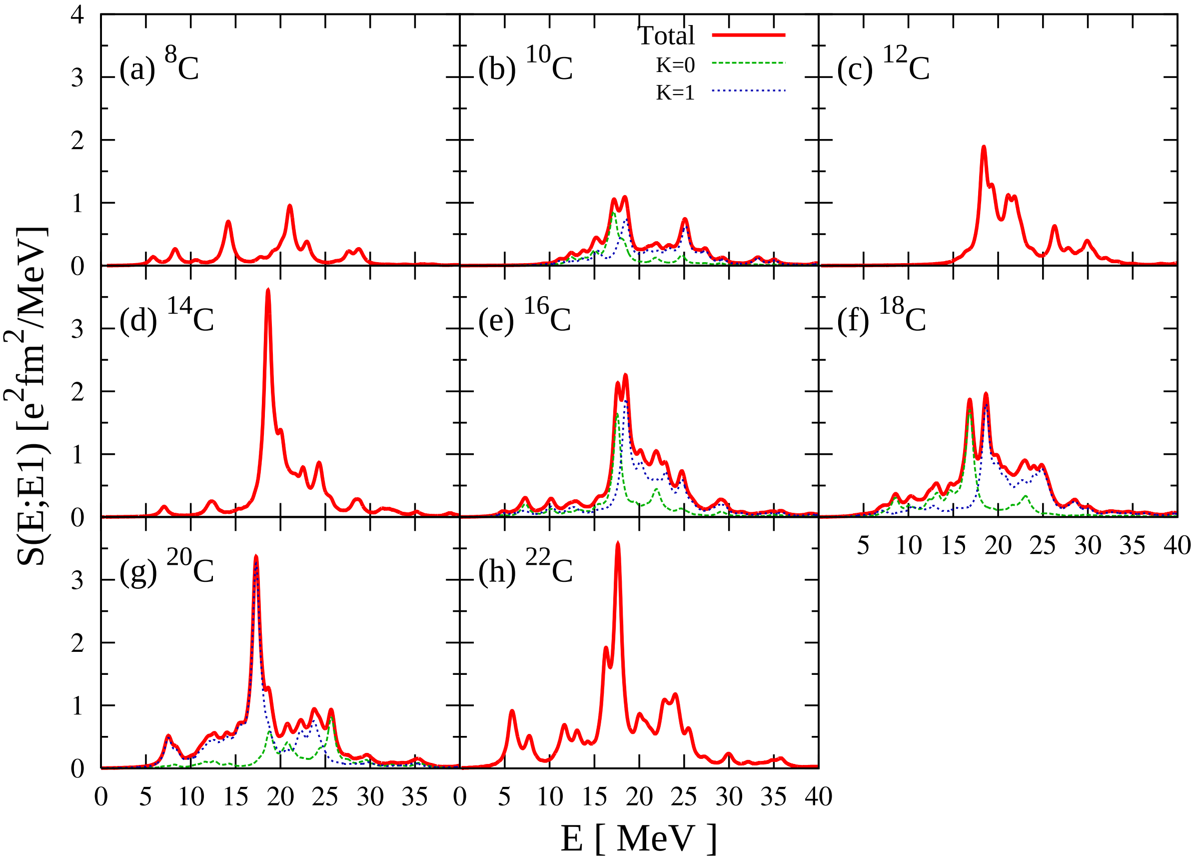

Figure A.1: $E1$ strength distributions of carbon isotopes. Solid line means the sum of strengths for $K = 0$ and $K = 1$ channels. Dashed line indicates the strength of $K = 0$ channel and dotted line indicates the strength of $K = 1$ channel. The smoothing parameter of $\Gamma = 1$ MeV is used.

A.10 $E1$ strength distributions of Oxygen ($Z = 8$) isotopes ($N = 6 - 20$)

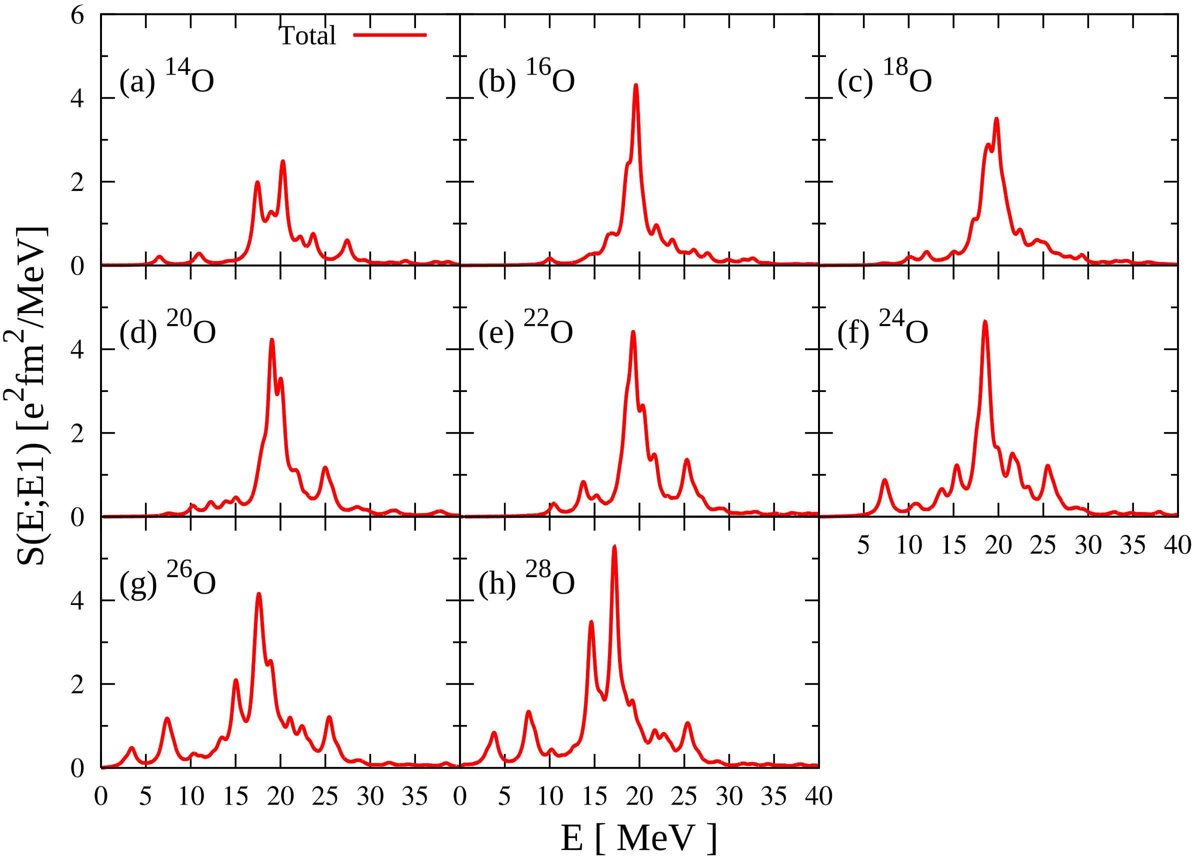

Figure A.2: $E1$ strength distributions of oxygen isotopes. The meanings of the lines are same as figure A.1. The smoothing parameter of $\Gamma = 1$ MeV is used.

A.11 $E1$ strength distributions of Neon ($Z = 10$) isotopes ($N = 6 - 22$)

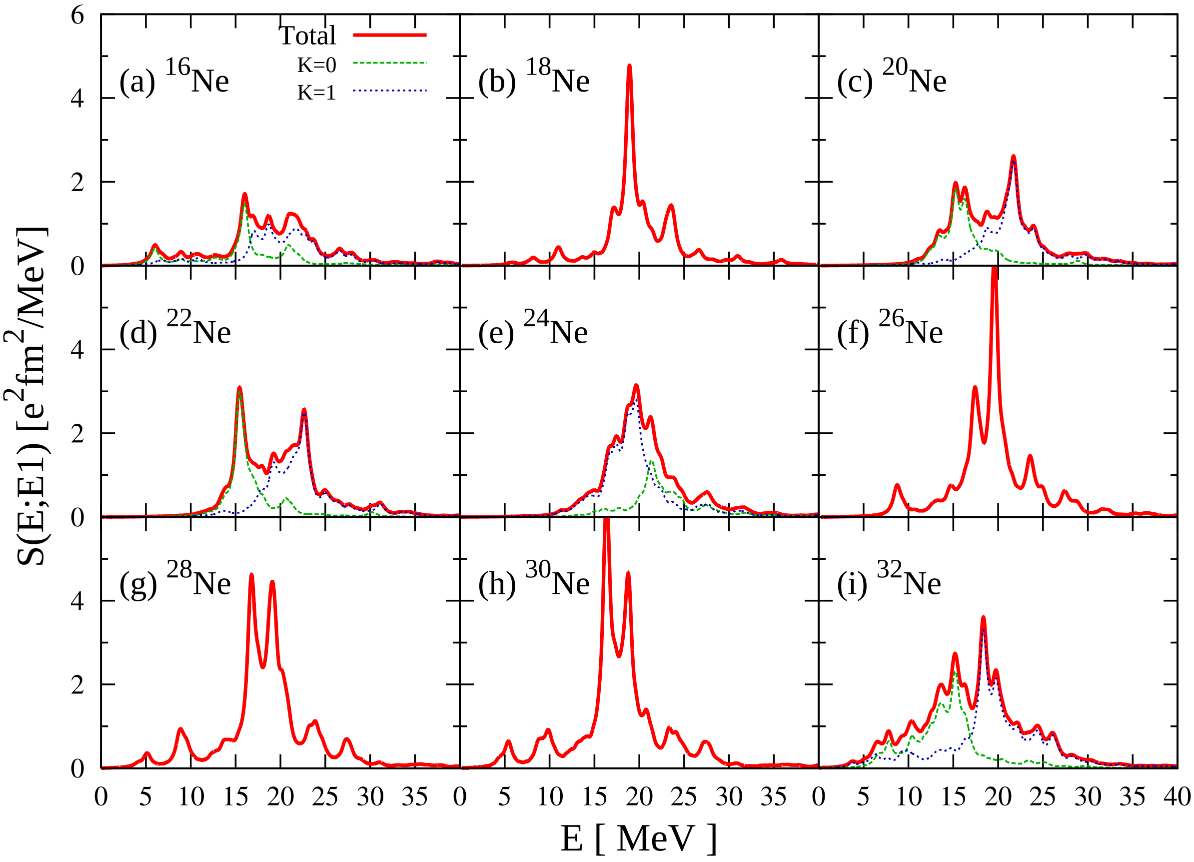

Figure A.3: $E1$ strength distributions of neon isotopes. The meanings of the lines are same as figure A.1. The smoothing parameter of $\Gamma = 1$ MeV is used.

A.12 $E1$ strength distributions of Magnesium ($Z = 12$) isotopes ($N = 6 - 28$)

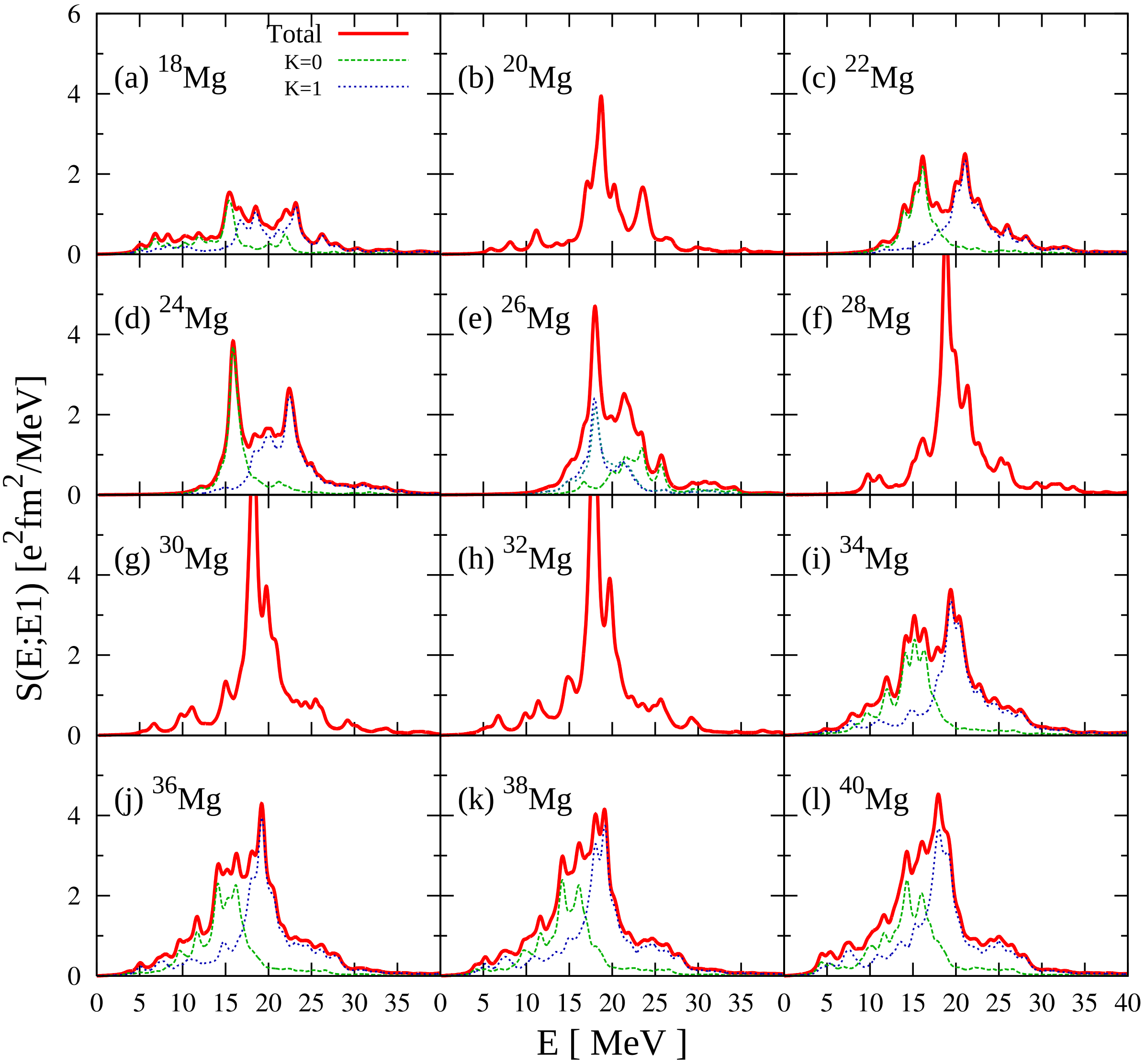

Figure A.4: $E1$ strength distributions of magnesium isotopes. The meanings of the lines are same as figure A.1. The smoothing parameter of $\Gamma = 1$ MeV is used.

A.13 $E1$ strength distributions of Silicon ($Z = 14$) isotopes ($N = 10 - 32$)

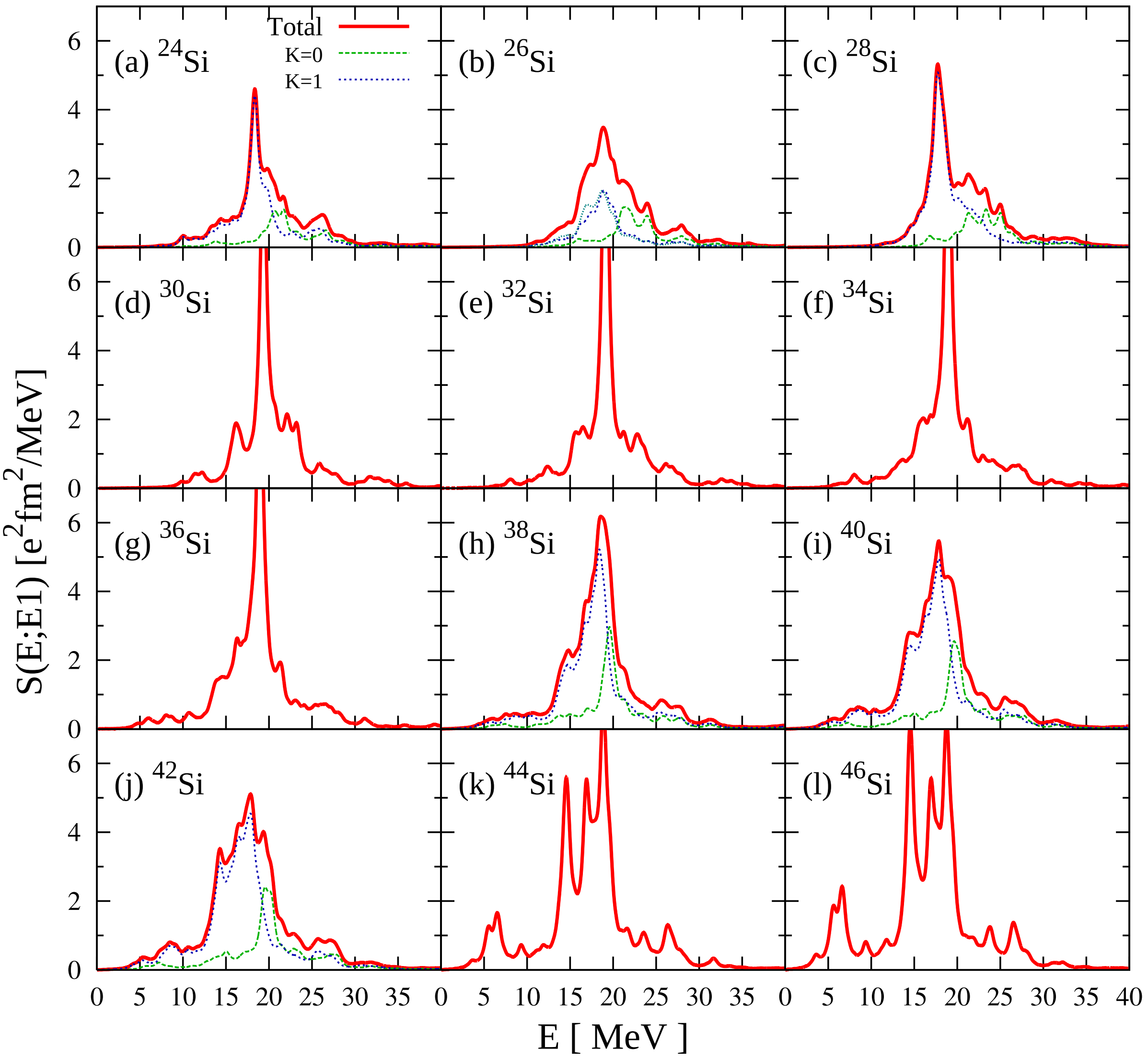

Figure A.5: $E1$ strength distributions of silicon isotopes. The meanings of the lines are same as figure A.1. The smoothing parameter of $\Gamma = 1$ MeV is used.

A.14 $E1$ strength distributions of Sulfur ($Z = 16$) isotopes ($N = 10 - 32$)

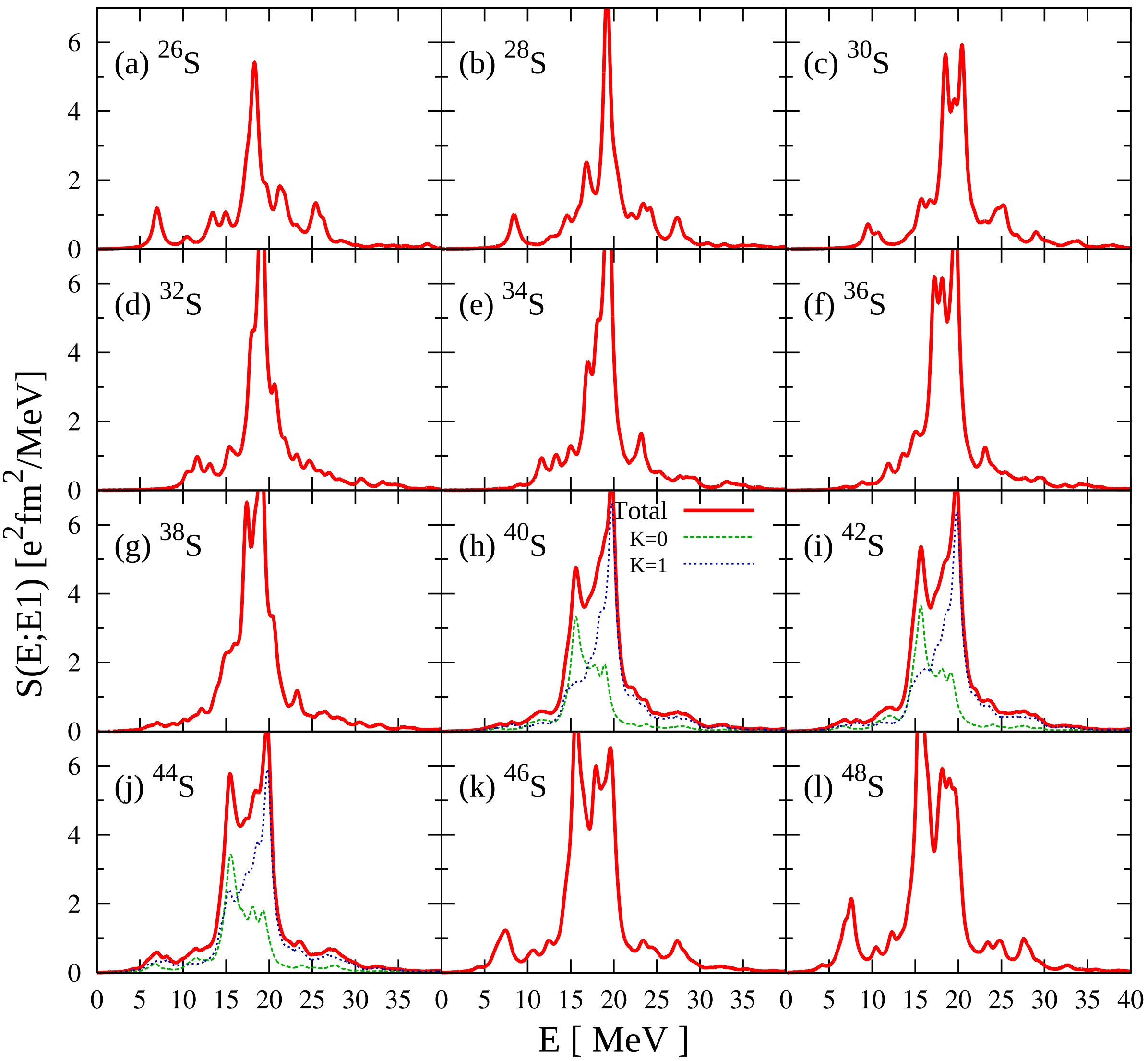

Figure A.6: $E1$ strength distributions of sulfur isotopes. The meanings of the lines are same as figure A.1. The smoothing parameter of $\Gamma = 1$ MeV is used.

A.15 $E1$ strength distributions of Argon $(Z = 18)$ isotopes $(N = 16 - 36)$

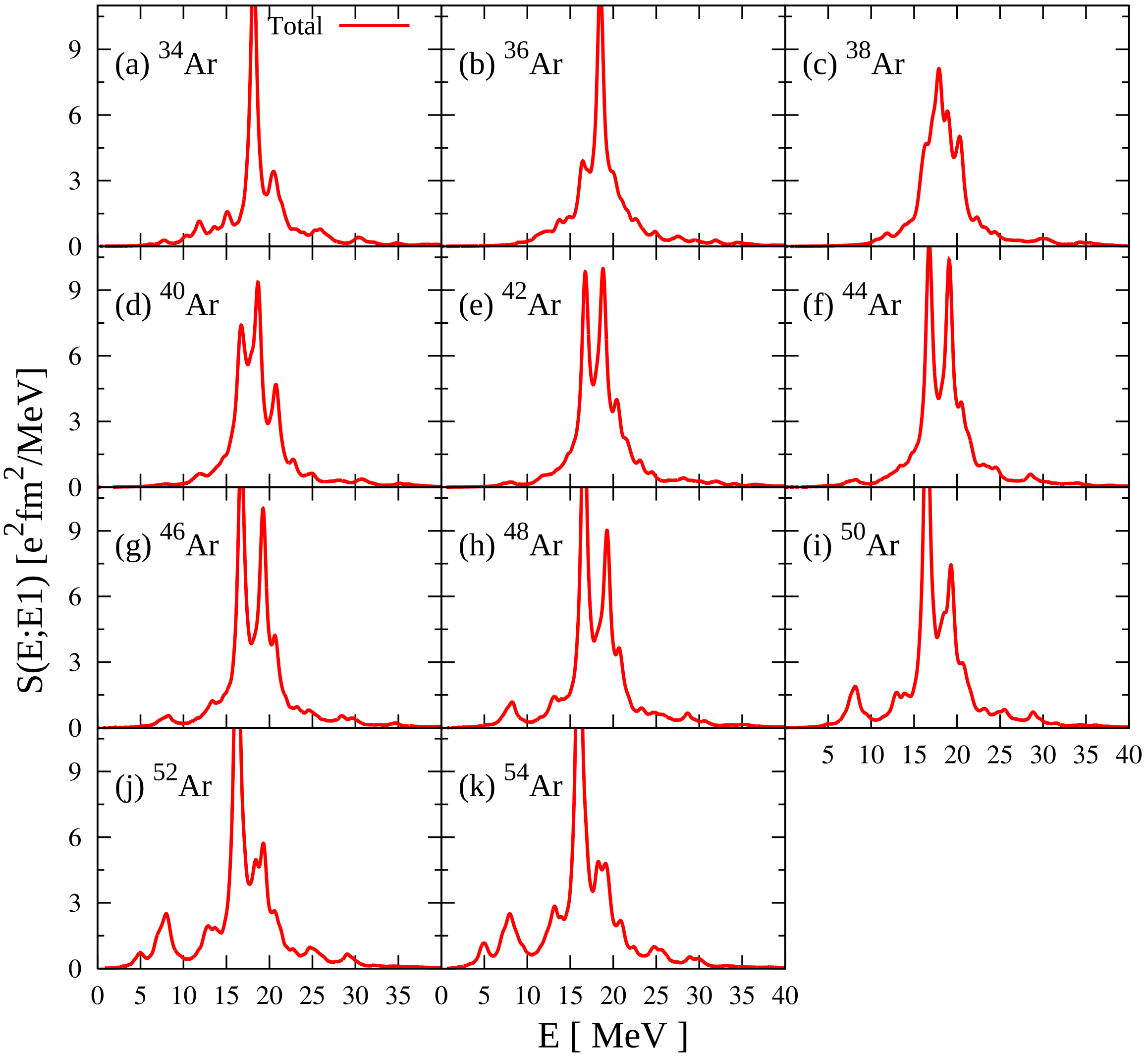

Figure A.7: $E1$ strength distributions of argon isotopes. The meanings of the lines are same as figure A.1. The smoothing parameter of $\Gamma = 1$ MeV is used.

A.16 $E1$ strength distributions of Calcium ($Z = 20$) isotopes ($N = 14 - 44$)

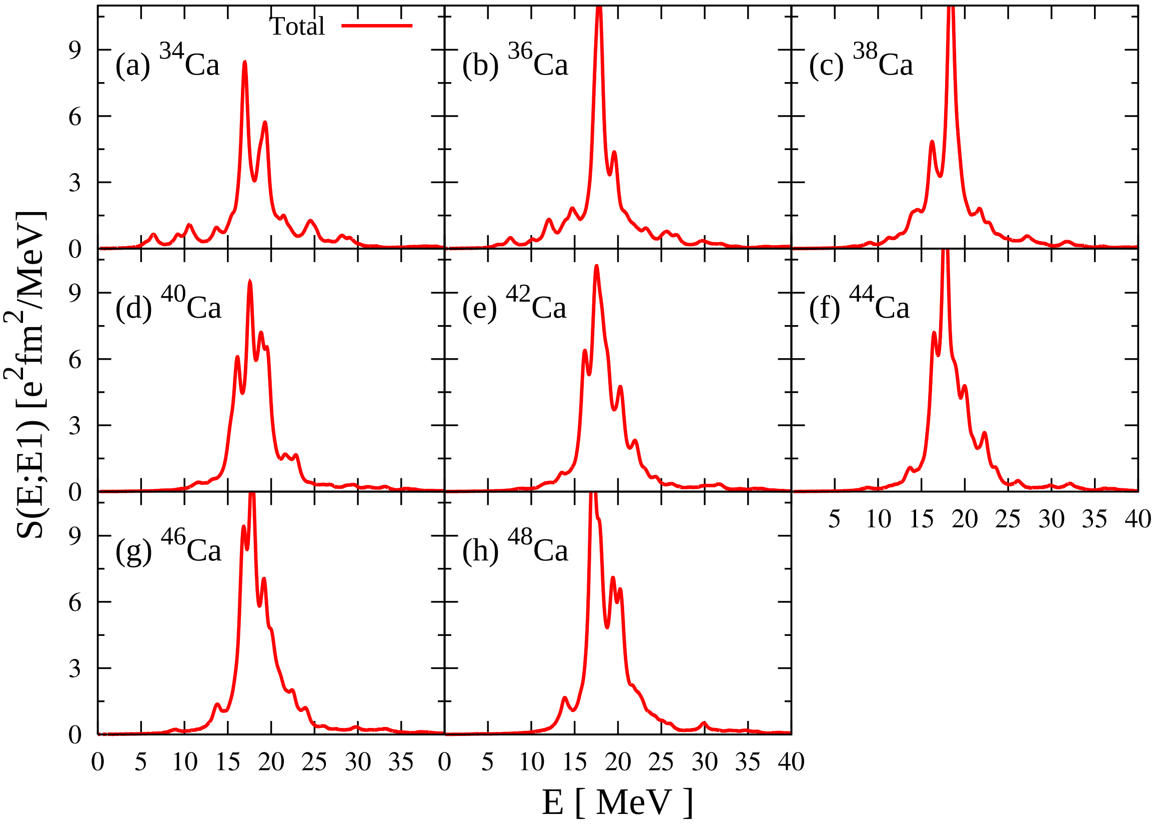

Figure A.8: $E1$ strength distributions of calcium isotopes ($N = 14 - 28$). The meanings of the lines are same as figure A.1. The smoothing parameter of $\Gamma = 1$ MeV is used.

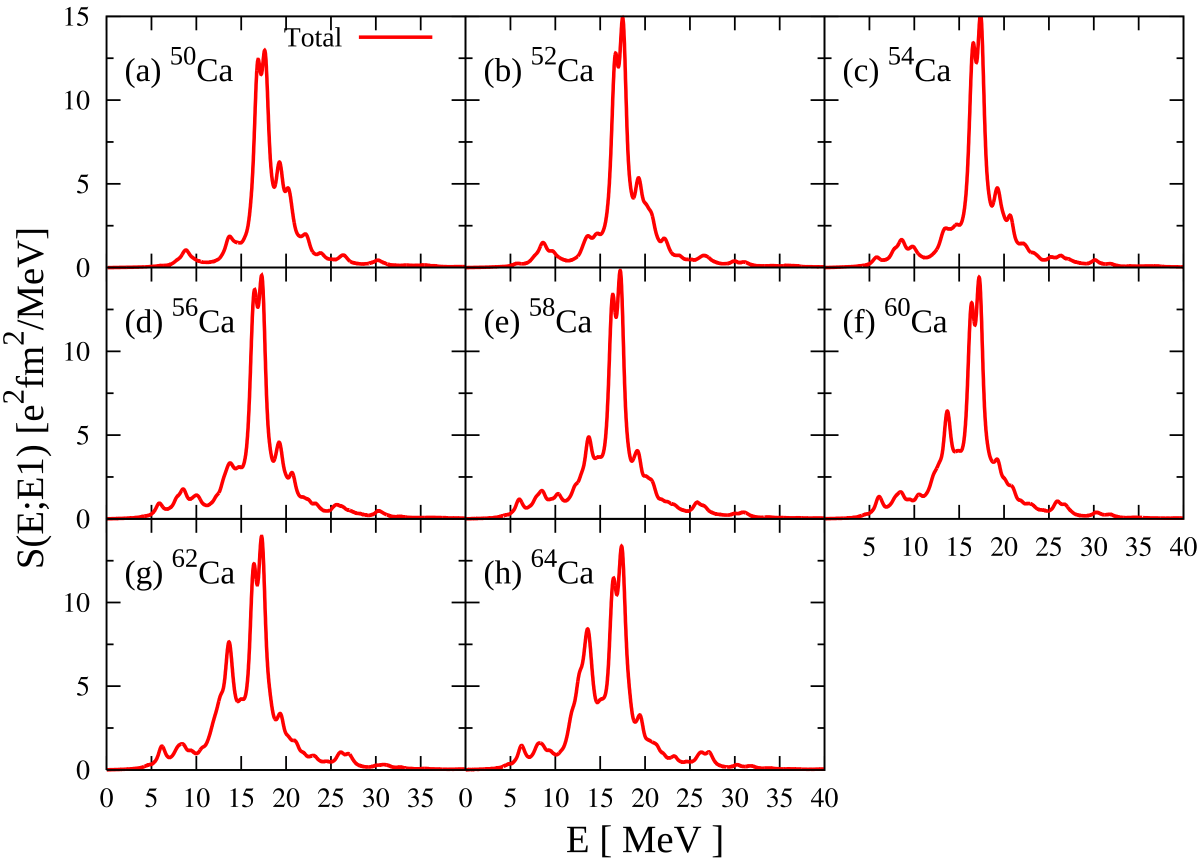

Figure A.9: $E1$ strength distributions of calcium isotopes ($N = 30 - 44$). The meanings of the lines are same as figure A.1. The smoothing parameter of $\Gamma = 1$ MeV is used.

B Imaginary-Time method

In this section, we show the Gradient Method which is used in the present study for calculation of ground state. And we use also constraint imaginary-time method. We introduce the relation between gradient method and imaginary-time method, and then show the constraints in imaginary-time method

B.1 Gradient method and Imaginary-time method

We consider the gradient method for an energy functional E of a system with respect to ϕ, ϕ^*, v, v^*. The variation of the E is written by

$$\delta E = \frac{\delta E}{\delta \phi}\delta\phi + \frac{\delta E}{\delta \phi^*}\delta\phi^* + \frac{\delta E}{\delta v}\delta v + \frac{\delta E}{\delta v^*}\delta v^*. \tag{B-1}$$

When the parameters ϕ, ϕ^*, v, v^* have some indexes($\vec{r}$ or l), δE is sum for the space expressed each index. Next, we consider forms of $\delta\phi, \delta v$ as

$$\delta\phi \equiv -\eta\frac{\delta E}{\delta\phi^*} \quad , \quad \delta v \equiv -\eta\frac{\delta E}{\delta v^*}, \tag{B-2}$$

where η is assumed real and positive number. If we can chose $\delta\phi^*, \delta v^*$ as conjugates of $\delta\phi, \delta v$, the variation δE can be written as

$$\delta E = -2\eta\left\{\left|\frac{\delta E}{\delta\phi}\right|^2 + \left|\frac{\delta E}{\delta v}\right|^2\right\} \ < \ 0 \ . \tag{B-3}$$

In this case, δE is always minus number. Then the energy E decreases monotonically in this variation, and finally the E achieves a ground state. If we can get the gradient of $\delta\phi, \delta v$ like above, we obtain the state of ground state. These procedure is called gradient method, but the points of gradient method is the search of good gradient $\delta\phi, \delta v$. In general, the gradient can be found through Hamiltonian of system. The time-evolution of eigenstate $|\phi\rangle$ of Hamiltonian h is described as

$$|\phi(t+\Delta t)\rangle = e^{ih\Delta t}|\phi(t)\rangle \simeq |\phi(t)\rangle + ih\Delta t|\phi(t)\rangle \tag{B-4}$$

where Δt is small value. If we chose the Δt of complex value, the variation of $|\phi\rangle$ with respect to Δt is equivalent to the variation $\delta\phi$ demanded on gradient method. These procedure is called imaginary-time method.

As a concrete example, we show the case of Hartree-Fock calculation. Let us consider two Slater determinants, $|\Phi\rangle$ composed single-particle wave functions ϕ_i $(i = 1, \cdots, A)$, and $|\Phi + \delta\Phi\rangle$ composed $\phi_i + \delta\phi_i$. $\delta\phi_i$ is the variation with respect to Δt. The energy expectation value with $|\Phi + \delta\Phi\rangle$ can be expressed by

$$E[\Phi + \delta\Phi] = E[\Phi] + \sum_{i=1}^{A}\int d\vec{r}\,\frac{\delta E}{\delta\phi_i}\delta\phi_i(\vec{r}) + \sum_{i=1}^{A}\int d\vec{r}\,\frac{\delta E}{\delta\phi_i^*}\delta\phi_i^*(\vec{r}) + O[\delta\phi_i^2, \delta\phi_i^{*2}], \tag{B-5}$$

where $E[\Phi] \equiv \langle\Phi|H|\Phi\rangle$. If we chose $\delta\phi_i$ as $-\Delta\tau\delta E/\delta\phi_i^*$, where $\Delta\tau$ is an infinitesimal positive and real value, (B-5) is rewritten as,

$$E[\Phi+\delta\Phi] = E[\Phi] - 2\Delta\tau\sum_{i=1}^{A}\int d\vec{r}\left|\frac{\delta E}{\delta\phi_i}\right|^2 < E[\Phi]. \tag{B-6}$$

The (B-6) means that this gradient procedure produce the energy minimum state. And note that the variation $\delta E/\delta\phi_i^*$ is a definition of single-particle Hamiltonian, and the coefficient $\Delta\tau$ is equivalent to the time-step Δt replaced complex value in HF equation.

B.2 Constraint imaginary-time method

In present study, we add some constraints to ground state in order to remove a center of mass motion and rotations of principal axes. We show the concrete form of constraint imaginary-time method in present study.

The constraints added by us are
(i) for center of mass,

$$\langle\Psi|\sum_{i=1}^{\mathrm{A}}\vec{r}_i|\Psi\rangle = 0, \qquad \vec{r}_i = \vec{x}_i + \vec{y}_i + \vec{z}_i, \tag{B-7}$$

(ii) for principal axes,

$$\langle\Psi|\sum_{i=1}^{\mathrm{A}}\vec{x}_i\vec{y}_i|\Psi\rangle = \langle\Psi|\sum_{i=1}^{\mathrm{A}}\vec{y}_i\vec{z}_i|\Psi\rangle = \langle\Psi|\sum_{i=1}^{\mathrm{A}}\vec{z}_i\vec{x}_i|\Psi\rangle = 0, \tag{B-8}$$

(iii) for orthogonal-normalization of single-particle states,

$$\langle\phi_k|\phi_l\rangle = \delta_{kl}. \tag{B-9}$$

(iv) for expectation value of particle number,

$$\langle\Psi|\hat{N}|\Psi\rangle = \mathrm{A}, \tag{B-10}$$

We set the Lagrange multipliers for the constraint conditions. ξ_μ, e_{kl} are correspond to each constraints. The variation $\delta\phi_l$ is

$$\begin{aligned} |\phi_l'\rangle =\ & |\phi_l\rangle + |\delta\phi_l\rangle \\ \rightarrow\ & |\phi_l\rangle - \eta\left\{\hat{h}|\phi_l\rangle - \sum_{\mu=1}^{6}\xi_\mu\hat{q}_\mu|\phi_l\rangle - \sum_k e_{lk}|\phi_k\rangle\right\}, \end{aligned} \tag{B-11}$$

where η is infinitesimal positive and real value and $|\phi_l'\rangle$ means the state developed one imaginary-time step. $\hat{q}_\mu$ are corresponding to spatial constraints, μ is index for each centers of mass

$\{\vec{x}_i,\ \vec{y}_i,\ \vec{z}_i\}$ and principal axes $\{\vec{x}_i\vec{y}_i,\ \vec{y}_i\vec{z}_i,\ \vec{z}_i\vec{x}_i\}$ ($\mu = 1 \sim 6$). e_{kl} is correspond to the Lagrange multiplier for orthogonal-normalization of single-particle states. e_{kl} is derived from with $\langle\phi'_k|\phi'_l\rangle = \delta_{kl}$.

$$\begin{aligned}
\langle\phi'_k|\phi'_l\rangle &= \langle\phi_k|\phi_l\rangle - \eta\Bigg\{ \langle\phi_k|\hat{h}|\phi_l\rangle + \langle\phi_k|\hat{h}^\dagger|\phi_l\rangle - \sum_{\mu=1}^{6}\xi_\mu\Big(\langle\phi_k|\hat{q}_\mu|\phi_l\rangle + \langle\phi_k|\hat{q}_\mu|\phi_l\rangle\Big) \\
&\qquad\qquad - \sum_{l,m} e_{ml}\langle\phi_k|\phi_m\rangle - \sum_{k,m} e_{km}\langle\phi_m|\phi_l\rangle \Bigg\} \\
&\Rightarrow\ \delta_{kl} - \eta\left\{ \langle\phi_k|g_l\rangle + \langle g_k|\phi_l\rangle - 2\sum_{\mu=1}^{6}\xi_\mu\langle\phi_k|\hat{q}_\mu|\phi_l\rangle - 2\ e_{kl} \right\}, \qquad \text{(B-12)} \\
&\qquad\qquad |g_l\rangle \equiv \hat{h}|\phi_l\rangle.
\end{aligned}$$

When $\langle\phi'_k|\phi'_l\rangle = \delta_{kl}$, e_{kl} is

$$e_{kl} = \frac{1}{2}\Big(\langle\phi_k|g_l\rangle + \langle g_k|\phi_l\rangle\Big) - \sum_{\mu=1}^{6}\xi_\mu\langle\phi_k|\hat{q}_\mu|\phi_l\rangle. \qquad \text{(B-13)}$$

But e_{kl} needs the value of ξ_μ. For the spatial constraints $\hat{q}_\mu$, the expectation value of ξ_μ with BCS wave function is written by

$$\begin{aligned}
\langle\Psi|\hat{q}_\mu|\Psi\rangle &= \int d\vec{r}\ q_\mu(\vec{r})\rho(\vec{r}) \\
&= \sum_{l>0} v_l^2\Big(\langle\phi_l|\hat{q}_\mu|\phi_l\rangle + \langle\phi_{\bar{l}}|\hat{q}_\mu|\phi_{\bar{l}}\rangle\Big) = 0, \qquad \text{(B-14)}
\end{aligned}$$

here $\hat{q}_\mu$ is one-body operator, the expectation value can be expressed by the density of a system.

We can consider the value of ξ_μ with aboves then.

$$\begin{aligned}
&\sum_{l>0} v_l^2\langle\phi'_l|\hat{q}_\mu|\phi'_l\rangle = 0 \\
&\quad = \sum_{l>0} v_l^2\left\{ \langle\phi_l|\hat{q}_\mu - \eta\left(\langle\phi_l|\hat{h}^\dagger\hat{q}_\mu - \sum_{\nu=1}^{6}\xi_\nu\langle\phi_l|\hat{q}_\nu\hat{q}_\mu - \sum_k e_{kl}\langle\phi_k|\hat{q}_\mu \right)\right\} \\
&\qquad\qquad \times\left\{ |\phi_l\rangle - \eta\left(\hat{h}|\phi_l\rangle - \sum_{\tau=1}^{6}\xi_\tau\hat{q}_\tau|\phi_l\rangle - \sum_m e_{lm}|\phi_m\rangle \right)\right\} \\
&\quad \Rightarrow\ \sum_{l>0} v_l^2\left\{ \langle\phi_l|\hat{q}_\mu|\phi_l\rangle - \eta\left(\langle g_l|\hat{q}_\mu|\phi_l\rangle + \langle\phi_l|\hat{q}_\mu|g_l\rangle - 2\sum_{\nu=1}^{6}\xi_\nu\langle\phi_l|\hat{q}_\nu\hat{q}_\mu|\phi_l\rangle \right.\right. \\
&\qquad\qquad \left.\left. - \sum_k e_{kl}\langle\phi_k|\hat{q}_\mu|\phi_l\rangle - \sum_k e_{lk}\langle\phi_l|\hat{q}_\mu|\phi_k\rangle \right)\right\}. \qquad \text{(B-15)}
\end{aligned}$$

And substitute e_{kl} for (B-15),

$$\begin{aligned}
&\sum_{l>0} v_l^2 \langle \phi_l' | \hat{q}_\mu | \phi_l' \rangle = 0 \\
&\qquad \Rightarrow \sum_{l>0} v_l^2 \Bigg[\langle \phi_l | \hat{q}_\mu | \phi_l \rangle - \eta \Bigg\{ \langle g_l | \hat{q}_\mu | \phi_l \rangle + \langle \phi_l | \hat{q}_\mu | g_l \rangle - 2 \sum_{\nu=1}^{6} \xi_\nu \langle \phi_l | \hat{q}_\nu \hat{q}_\mu | \phi_l \rangle \\
&\qquad \underbrace{- \sum_k \left(\frac{1}{2} \Big(\langle \phi_k | g_l \rangle + \langle g_k | \phi_l \rangle \Big) - \sum_{\mu=1}^{6} \xi_\nu \langle \phi_k | \hat{q}_\nu | \phi_l \rangle \right) \langle \phi_k | \hat{q}_\mu | \phi_l \rangle - h.c.}_{\mathbb{S}} \Bigg\} \Bigg]
\end{aligned} \tag{B-16}$$

For this $\mathbb{S}$, we can use the relation $A + A^* = 2\mathrm{Re}[A]$ in general.

$$\mathbb{S} = -\sum_k \mathrm{Re} \left[\Big(\langle \phi_k | g_l \rangle + \langle g_k | \phi_l \rangle \Big) \langle \phi_k | \hat{q}_\mu | \phi_l \rangle - 2 \sum_k \sum_{\nu=1}^{6} \xi_\nu \langle \phi_k | \hat{q}_\nu | \phi_l \rangle \langle \phi_k | \hat{q}_\mu | \phi_l \rangle \right],$$

The coefficient of ξ_ν can be rewritten to simple one with $A_{\nu\mu}$ as,

$$2\eta \sum_{\nu=1}^{6} \xi_\nu A_{\nu\mu} \equiv 2\eta \sum_{\nu=1}^{6} \xi_\nu \sum_{k,l>0} v_l^2 \Big\{ \langle \phi_l | \hat{q}_\nu \hat{q}_\mu | \phi_l \rangle - \mathrm{Re}\big[\langle \phi_k | \hat{q}_\nu | \phi_l \rangle \langle \phi_k | \hat{q}_\mu | \phi_l \rangle \big] \Big\}. \tag{B-17}$$

The other parameter can be replace to the parameter ζ_μ with one index μ as

$$\tilde{\zeta}_\mu \equiv \sum_{l>0} v_l^2 \left[\langle \phi_l | \hat{q}_\mu | \phi_l \rangle - \eta \left\{ 2\mathrm{Re}[\langle \phi_l | \hat{q}_\mu | g_l \rangle] - \sum_{k>0} \mathrm{Re}\Big[\Big(\langle \phi_k | g_l \rangle + \langle g_k | \phi_l \rangle \Big) \langle \phi_k | \hat{q}_\mu | \phi_l \rangle \Big] \right\} \right] \tag{B-18}$$

Finally, the Lagrange multipliers of spatial constraints ξ_μ, e_{kl} can be obtained from

$$\zeta_\mu = \sum_{\nu=1}^{6} \xi_\nu A_{\nu\mu}, \tag{B-19}$$

where $\zeta_\mu \equiv -\tilde{\zeta}_\mu / 2\eta$. In addition, we can solve these coefficients to need occupation probabilities v_l^2 which does not need to be defined at same time with single-particle state. But they of course, need the information of basis (single-particle state) which is a single-particle energy.

The constraints of particle number is due to the definition of occupation probabilities v^2, a chemical-potential λ and the gap energy Δ. In order to define these parameters, we solve the gap equation and the equation of number which they are written by ε_l, λ and Δ. The parameters are λ and Δ for in these two equations. In present study, we solve simultaneous equations following $\mathcal{F}(\lambda,\Delta)$ and $\mathcal{G}(\lambda,\Delta)$.

$$\mathcal{F}(\lambda,\Delta) \equiv \sum_{k>0}\left\{1-\frac{\varepsilon_k-\lambda}{\sqrt{(\varepsilon_k-\lambda)^2+\Delta^2}}\right\}-N_\tau. \tag{B-20}$$

$$\mathcal{G}(\lambda,\Delta) \equiv \frac{G_\tau}{2}\sum_{k>0}\frac{\Delta}{\sqrt{(\varepsilon_k-\lambda)^2+\Delta^2}}-\Delta. \tag{B-21}$$

where index τ shows isospin. The simultaneous equations for $\mathcal{F}(\lambda,\Delta)=0,\ \mathcal{G}(\lambda,\Delta)=0$ can be solved with two-dimensional Newton-Raphson method. In the calculation, we need following derivative values with respect to λ,Δ.

$$\begin{aligned}
\frac{\partial\mathcal{F}}{\partial\lambda} &= \sum_{k>0}\left\{\frac{1}{\sqrt{(\varepsilon_k-\lambda)^2+\Delta^2}}-\frac{(\varepsilon_k-\lambda)^2}{\{(\varepsilon_k-\lambda)^2+\Delta^2\}^{3/2}}\right\},\quad \frac{\partial\mathcal{F}}{\partial\Delta}=\sum_{k>0}\left\{\frac{\Delta(\varepsilon_k-\lambda)}{\{(\varepsilon_k-\lambda)^2+\Delta^2\}^{3/2}}\right\},\\
\frac{\partial\mathcal{G}}{\partial\lambda} &= \frac{G_\tau}{2}\sum_{k>0}\frac{\Delta(\varepsilon_k-\lambda)}{\{(\varepsilon_k-\lambda)^2+\Delta^2\}^{3/2}},\\
\frac{\partial\mathcal{G}}{\partial\Delta} &= \frac{G_\tau}{2}\sum_{k>0}\left\{\frac{1}{\sqrt{(\varepsilon_k-\lambda)^2+\Delta^2}}-\frac{\Delta^2}{\{(\varepsilon_k-\lambda)^2+\Delta^2\}^{3/2}}\right\}-1.
\end{aligned}$$

The algorithm of two-dimensional Newton-Raphson method for $f(x,y)=0,\ g(x,y)=0$ is

$$\begin{pmatrix} f(x_\mathrm{A},y_\mathrm{A}) \\ g(x_\mathrm{A},y_\mathrm{A}) \end{pmatrix} = \begin{pmatrix} f(x_i,y_i) \\ g(x_i,y_i) \end{pmatrix} + \underbrace{\begin{pmatrix} \partial_x f(x_i,y_i) & \partial_y f(x_i,y_i) \\ \partial_x g(x_i,y_i) & \partial_y g(x_i,y_i) \end{pmatrix}}_{\mathbb{A}} \begin{pmatrix} dx \\ dy \end{pmatrix} = 0$$

where $x_\mathrm{A}, y_\mathrm{A}$ are solutions and $x_{i+1}=x_i+dx$, i shows iteration number. (dx,dy) can be expressed with inversion of $\mathbb{A}$ as,

$$\begin{pmatrix} dx \\ dy \end{pmatrix} = -\frac{1}{\det\mathbb{A}}\begin{pmatrix} -\partial_x f(x_i,y_i) & \partial_x g(x_i,y_i) \\ \partial_y f(x_i,y_i) & -\partial_y g(x_i,y_i) \end{pmatrix}. \tag{B-22}$$

When $(dx,dy)\sim(0,0)$, we can get the solutions.

C BCS equation

This section shows the BCS equations which can describe Gap energy and express occupation probabilities of orbitals in the system interacted pairing correlation. First, we set Hamiltonian H written by the creation and annihilation operators of Fermion as

$$H = \sum_{\alpha,\beta} t_{\alpha\beta} c^{\dagger}_{\alpha} c_{\beta} + \frac{1}{4} \sum_{\alpha,\beta,\gamma,\delta} \bar{\mathcal{V}}_{\alpha\beta\gamma\delta} c^{\dagger}_{\alpha} c^{\dagger}_{\beta} c_{\delta} c_{\gamma}, \tag{C-1}$$

$$\bar{\mathcal{V}}_{\alpha\beta\gamma\delta} \equiv \mathcal{V}_{\alpha\beta\gamma\delta} - \mathcal{V}_{\alpha\beta\delta\gamma}. \tag{C-2}$$

We set the BCS trial wave function $|\Phi_{\mathrm{BCS}}\rangle$ as like,

$$|\Phi_{\mathrm{BCS}}\rangle = \prod_{l>0} (u_l + v_l c^{\dagger}_{l} c^{\dagger}_{\bar{l}}) |0\rangle, \tag{C-3}$$

where $\bar{l}$ means pair of l-state which are usually assumed the time-reversal relation between the pair and v_l can be chosen as real number in static system. The BCS wave function does not an eigenstate of particle number, breaks the number conservation. So, usually we need the number constraint to Hamiltonian in the BCS theory. H is modified as,

$$H' \equiv H - \lambda \hat{N}, \tag{C-4}$$

$$\langle \Phi_{\mathrm{BCS}} | \hat{N} | \Phi_{\mathrm{BCS}} \rangle = 2 \sum_{l>0} v_l^2 \equiv A,$$

where $\hat{N}$ is number operator, λ is a Lagrange multiplier and A is particle number of the system. H' is a standard Hamiltonian in BCS theory. The expectation value of this H' with $|\Phi_{\mathrm{BCS}}\rangle$ is,

$$\begin{aligned}
\langle \Phi_{\mathrm{BCS}} | H' | \Phi_{\mathrm{BCS}} \rangle &= \sum_{k>0} \Bigg\{ \Big(t_{kk} + t_{\bar{k}\bar{k}} - 2\lambda \Big) v_k^2 \\
&\quad + \frac{1}{2} \sum_{k'>0} \left(\bar{\mathcal{V}}_{kk'kk'} + \bar{\mathcal{V}}_{\bar{k}\bar{k}'\bar{k}\bar{k}'} + \bar{\mathcal{V}}_{k\bar{k}'k\bar{k}'} + \bar{\mathcal{V}}_{\bar{k}k'\bar{k}k'} \right) v_k^2 v_{k'}^2 + \sum_{k'>0} \bar{\mathcal{V}}_{k\bar{k}k'\bar{k}'} \; u_k v_k u_{k'} v_{k'} \Bigg\} \\
&= \sum_{k} \left\{ \Big(t_{kk} - \lambda \Big) v_k^2 + \frac{1}{2} \sum_{k'} \bar{\mathcal{V}}_{kk'kk'} \; v_k^2 v_{k'}^2 \right\} + \sum_{k,k'>0} \bar{\mathcal{V}}_{k\bar{k}k'\bar{k}'} \; u_k v_k u_{k'} v_{k'}
\end{aligned} \tag{C-5}$$

The BCS equation can be derived from the variation $\delta \langle \Phi_{\mathrm{BCS}} | H' | \Phi_{\mathrm{BCS}} \rangle = 0$, as like

$$\begin{aligned}
\delta \langle \Phi_{\mathrm{BCS}} | H' | \Phi_{\mathrm{BCS}} \rangle &= \left(\frac{\partial}{\partial v_l} + \frac{\partial u_l}{\partial v_l} \frac{\partial}{\partial u_l} \right) \langle \Phi_{\mathrm{BCS}} | H' | \Phi_{\mathrm{BCS}} \rangle \\
&= 2 v_l \left\{ \Big(t_{ll} + t_{\bar{l}\bar{l}} - 2\lambda \Big) + \sum_{k} \Big(\bar{\mathcal{V}}_{lklk} + \bar{\mathcal{V}}_{\bar{l}k\bar{l}k} \Big) v_k^2 \right\} \\
&\qquad + 2 u_l \sum_{k>0} \bar{\mathcal{V}}_{l\bar{l}k\bar{k}} \; u_k v_k - 2 \frac{v_l}{u_l} v_l \sum_{k>0} \bar{\mathcal{V}}_{l\bar{l}k\bar{k}} \; u_k v_k = 0.
\end{aligned}$$

$$\Rightarrow \; u_l v_l \left\{ \Big(t_{ll} + t_{\bar{l}\bar{l}} - 2\lambda \Big) + \sum_{k} \Big(\bar{\mathcal{V}}_{lklk} + \bar{\mathcal{V}}_{\bar{l}k\bar{l}k} \Big) v_k^2 \right\} + \; (u_l^2 - v_l^2) \sum_{k>0} \bar{\mathcal{V}}_{l\bar{l}k\bar{k}} \; u_k v_k = 0. \tag{C-6}$$

We can rewrite (C-6) to simple one with the following values.

$$\Big(t_{ll} + t_{\bar{l}\bar{l}} - 2\lambda\Big) + \sum_{k} \Big(\bar{\mathcal{V}}_{lklk} + \bar{\mathcal{V}}_{\bar{l}k\bar{l}k}\Big) v_k^2 = \frac{1}{2}\left\{ t_{ll} + t_{\bar{l}\bar{l}} + \sum_{k} \Big(\bar{\mathcal{V}}_{lklk} + \bar{\mathcal{V}}_{\bar{l}k\bar{l}k}\Big) v_{k'}^2 \right\} - \lambda \;\equiv\; \tilde{\varepsilon}_l \quad \text{(C-7)}$$

$$-\sum_{k'>0} \bar{\mathcal{V}}_{l\bar{l}k'\bar{k}'}\; u_{k'} v_{k'} \;\equiv\; \Delta_l \qquad \text{(C-8)}$$

Finally, the BCS equation is described with a normalization condition $u_l^2 + v_l^2 = 1$, as

$$2u_l v_l \tilde{\varepsilon}_l + \Delta_l (2v_l^2 - 1) = 0. \qquad \text{(C-9)}$$

But, we note that this BCS equation is assumed that there is the time-reversal relation between l- and $\bar{l}$-state. If we do not assume the time-reversal relation between the pair, BCS equation is modified as

$$u_l v_l (\bar{\varepsilon}_l + \bar{\varepsilon}_{\bar{l}}) + \Delta_l (2v_l^2 - 1) = 0, \qquad \text{(C-10)}$$

where $\bar{\varepsilon}_l \equiv t_{ll} + \sum_k \mathcal{V}_{lklk} v_k^2 - \lambda$.

v_l^2, u_l^2 can be formed with the normalization condition as,

$$v_l^2 = \frac{1}{2}\left\{ 1 \pm \frac{\tilde{\varepsilon}_l}{\sqrt{\tilde{\varepsilon}_l^2 + \Delta_l^2}} \right\}, \qquad u_l^2 = \frac{1}{2}\left\{ 1 \pm \frac{\tilde{\varepsilon}_l}{\sqrt{\tilde{\varepsilon}_l^2 + \Delta_l^2}} \right\}. \qquad \text{(C-11)}$$

In the case of no pairing correlation, one has $\delta = 0$ and $v_l^2 = 1, u_l^2 = 0$ for occupied orbital ($\tilde{\varepsilon}_l < 0$). The only possible the solutions of (C-11) are therefore:

$$v_l^2 = \frac{1}{2}\left\{ 1 - \frac{\tilde{\varepsilon}_l}{\sqrt{\tilde{\varepsilon}_l^2 + \Delta_l^2}} \right\} \quad , \quad u_l^2 = \frac{1}{2}\left\{ 1 + \frac{\tilde{\varepsilon}_l}{\sqrt{\tilde{\varepsilon}_l^2 + \Delta_l^2}} \right\} \qquad \text{(C-12)}$$

We can obtain the Gap equation with (C-8) and (C-12),

$$\Delta_l = -\frac{1}{2} \sum_{k>0} \bar{\mathcal{V}}_{l\bar{l}k\bar{k}}\; \frac{\Delta_k}{\sqrt{\tilde{\varepsilon}_k^2 + \Delta_k^2}}. \qquad \text{(C-13)}$$

In general, v_l^2, u_l^2, Δ_l are nonlinear equations and have to be solved by iteration.

D Intrinsic frame and Deformation parameters

In this section, we show the deformation parameters β, γ which characterize quadrupole deformation, and the expression for β- and γ-vibration.

D.1 Intrinsic frame

We first define the general deformation parameter with a function described by the length of the radius vector pointing from the origin to the surface. The function is

$$R(\theta, \varphi) = R_0 \left(1 + \sum_{\lambda=0} \sum_{\mu=-\lambda}^{\mu=\lambda} a^*_{\lambda\mu} Y_{\lambda,\mu}(\theta, \varphi) \right). \tag{D-1}$$

$R(\theta, \varphi)$ shows the length of the radius vector pointing from the origin to the surface. R_0 is the radius of the sphere with a same nuclear volume. The residual part means the difference from sphere shape with the spherical harmonic function $Y_{\lambda,\mu}(\theta, \varphi)$. The complex parameter $a^*_{\lambda\mu}$ shows the weight of $Y_{\lambda,\mu}$ in $R(\theta, \varphi)$, so then we can consider the various shape of nucleus with this variation of $a^*_{\lambda\mu}$. These θ, φ has the relation with Cartesian coordinate, as like

$$x = r\ \sin\theta\ \cos\varphi, \quad y = r\ \sin\theta\ \sin\varphi, \quad z = r\ \cos\theta.$$

We redefine θ, φ from z-axis in the Cartesian coordinate whose origin agree with the center of mass of nucleus as like Fig. D.10. The coordinate system redefined from the center of mass is called intrinsic frame or body-fixed frame. In adding, $a^*_{\lambda\mu}$ has a following symmetry,

$$a^*_{\lambda\mu} = (-1)^\mu a_{\lambda-\mu}. \tag{D-2}$$

This is because that $R(\theta, \varphi)$ is real and the spherical harmonic function $Y_{\lambda,\mu}(\theta, \varphi)$ has $Y^*_{\lambda,\mu}(\theta, \varphi) = (-1)^\mu Y_{\lambda,-\mu}(\theta, \varphi)$. The R can express various shape, but $a_{00}, a_{1\mu}$ are excluded from nuclear deformation parameter because nuclear system has the saturation property and the center of mass of nucleus is fixed. We should consider the nuclear deformation from quadrupole case ($\lambda \geq 2$).

D.2 Quadrupole deformation parameter (β, γ)

We consider only the nuclear quadrupole deformation (ellipsoid shape). Now we chose the intrinsic frame as like Fig. D.10. We call this frame K'-frame. In K'-frame, angle parameters is written as θ', φ' and nuclear surface $R(\theta', \varphi')$ is also written by

$$R(\theta', \varphi') = R_0 \left(1 + \sum_{\mu=-2}^{\mu=2} a^*_{2\mu} Y_{2,\mu}(\theta', \varphi') \right). \tag{D-3}$$

This $R(\theta', \varphi')$ is assumed ellipsoid shape, then $R(\theta', \varphi')$ is reflection symmetric about $x'y'$-, $y'z'$- and $z'x'$-plane. In this case, the deformation parameter $a^*_{2\mu}$ are restricted and can be reduced. Now we chose the z'-axis to axial symmetric one. There are some restrictions for $a^*_{2\mu}$, from the reflection symmetry about $x'y'$-plane, $a^*_{21} = a^*_{2-1} = 0$ and from the symmetry about $y'z'$- and

$z'x'$-plane, $a^*_{22} = a^*_{2-2}$. The five coefficients $a_{2\mu}$ reduce to two real independent variables a_{20} and $a_{22} = a_{2-2}$ which together with the three Euler angles, give a complete description of this system. Usually, we introduce instead of a_{20} and a_{22} the so-called Hill-Wheeler coordinates β, γ through the relation

$$\left\{ \begin{array}{l} a_{20} = \beta \ \cos\gamma, \\ a_{22} = a_{2-2} = \frac{1}{\sqrt{2}}\beta \ \sin\gamma, \end{array} \right. \tag{D-4}$$

R can be expressed in the directions of K'-frame as

$$\begin{gathered} R\left(\frac{\pi}{2}, 0\right) \equiv R_1 \ , \ R\left(\frac{\pi}{2}, \frac{\pi}{2}\right) \equiv R_2 \ , \ R(0,0) \equiv R_3, \\ R_k = R_0 \left\{ 1 + \sqrt{\frac{5}{4\pi}} \ \beta \ \cos\left(\gamma - k\frac{2\pi}{3}\right) \right\}. \\ k = 1, 2, 3 \equiv \{x', y', z'\} \end{gathered} \tag{D-5}$$

The variation $\delta R_k (\equiv R_k - R_0)$ can indicate several shapes with Eq.(D-6). In the case of $\beta = 0$, $\delta R_k = 0$ namely the shape of nucleus is spherical. In the case of $\beta > 0$ with $\gamma = 0$, $\delta R_1 = \delta R_2 < 0, R_3 > R_0$ namely the shape is prolate which is shown in the left side of Fig. D.11. In the case of $\beta > 0$ with $\gamma = \pi$, $\delta R_1 = \delta R_2 > 0, R_3 < R_0$ these values indicate the oblate shape which is shown in the right side of Fig. D.11, but there is a same oblate shape in the case of $\beta < 0$ with $\gamma = 0$ namely the case of $\delta R_1 = \delta R_2 > 0, R_3 < R_0$. In general, we can express the axial symmetric deformation in a restricted (β, γ) region. We commonly chose the region of $\beta \geq 0$, $0 \leq \gamma \leq \pi/3$ as (β, γ)-plane in order to express the axial symmetric deformation. In adding, the case of $\beta > 0, \ \gamma > 0$ indicate $R_1 \neq R_2 \neq R_3$, this means this case does not belong to both prolate and oblate case, so we call this case triaxial deformation.

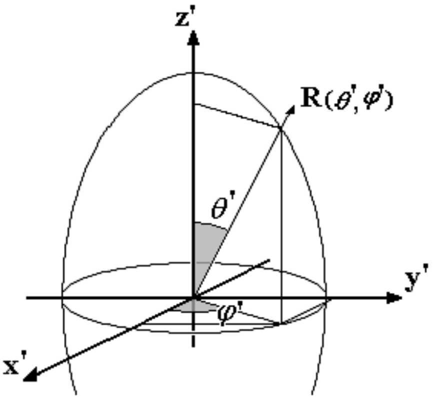

Figure D.10: K'-frame

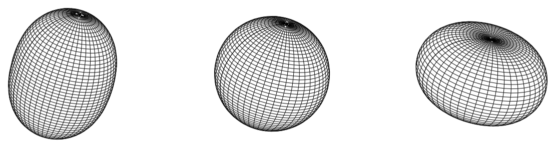

Figure D.11: Nuclear shapes

D.3 β- and γ-vibration

We can consider the vibration of nuclear surface with deformation parameters $\{a_{20}, a_{22}\}$ or $\{\beta, \gamma\}$. This means deformation parameters can describe some nuclear state called collective motion. If we can consider the collective motion in their space, they are often called "collective parameter" also. When a nucleus has deformation with (β_0, γ_0) in the ground state, the nucleus is an equilibrium point on the energy surface expressed (β, γ)-plane. This means that we can consider the nuclear potential surface with respect to (β, γ). So, the vibration of (β, γ) values can be regarded the vibration around the equilibrium point on (β, γ)-plane as like Fig. D.12.

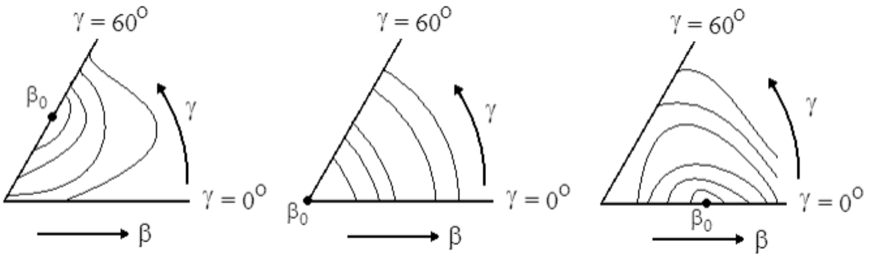

Figure D.12: Aspects of $V(\beta, \gamma)$. From left side, oblate, spherical and prolate cases are shown.

Now we consider some infinitesimal vibration $(\delta\beta, \delta\gamma)$ around (β_0, γ_0). in both expressions $\{\beta, \gamma\}$ and $\{a_{20}, a_{22}\}$. The infinitesimal vibration can be expressed as

$$\begin{aligned} (\beta_0, \gamma_0) \quad &\rightarrow \quad (\ \beta_0 + \delta\beta, \gamma_0 + \delta\gamma\ ), \\ \left(a_{20}^{(0)}, a_{22}^{(0)}\right) \quad &\rightarrow \quad \left((\beta_0 + \delta\beta)\cos(\gamma_0 + \delta\gamma), \frac{1}{\sqrt{2}}(\beta_0 + \delta\beta)\cos(\gamma_0 + \delta\gamma)\right) \\ &\approx \left(\beta_0 + \delta\beta\ , \frac{1}{\sqrt{2}}\beta_0\delta\gamma\right) = (a_{20}, a_{22}), \qquad \delta\beta \cdot \delta\gamma \approx 0, \end{aligned}$$

where $(a_{20}^{(0)}, a_{22}^{(0)})$ is the expression of (β_0, γ_0) in $\{a_{20}, a_{22}\}$ and using Eq.(D-4). And we can see the $R(\theta', \varphi')$ with these values as

$$R(\theta', \varphi') = R_0 \left\{\ 1 + a_{20}^* Y_{2,0}(\theta', \varphi') + a_{22}^* \Big(Y_{2,2}(\theta', \varphi') + Y_{2,-2}(\theta', \varphi')\Big)\ \right\}. \tag{D-6}$$

We can understand the corresponds between $a_{20} \Leftrightarrow Y_{2,0}$ and $a_{22} \Leftrightarrow Y_{2,2}$. The operators,

$$Q_{20} \equiv r^2 Y_{2,0} \quad \text{and} \quad Q_{22} \equiv r^2 \frac{1}{\sqrt{2}}\Big(Y_{2,2} + Y_{2,-2}\Big), \tag{D-7}$$

produce the vibration of $\delta\beta$ and $\delta\gamma$. They are called β-vibration and γ-vibration.

D.4 Definition of quadrupole deformation parameter (β, γ)

In this thesis, we use following quadrupole deformation parameters (β, γ),

$$\beta \equiv \frac{4\pi}{5} \frac{\sqrt{\langle Q_{20}\rangle^2 + \langle Q_{22}\rangle^2}}{A\langle r^2\rangle}, \qquad \gamma \equiv \frac{180^\circ}{\pi}\ \arctan\left(\frac{\langle Q_{22}\rangle}{\langle Q_{20}\rangle}\right), \tag{D-8}$$

where $\sqrt{\langle r^2\rangle}$ is root mean square radius of nucleus. These parameters are given also in [79, 80].

Bibliography

[1] A.Bohr and B.R.Mottelson, "*Nuclear Structure*, Vol.I" (Benjamin, New York,1969)

[2] A.Bohr and B.R.Mottelson, "*Nuclear Structure*, Vol.II" (Benjamin, New York,1975)

[3] P. Ring and P. Schuck, "*The Nuclear Many−Body Problem*" (Springer-Verlag, 1980).

[4] J.-P. Blaizot and G. Ripka, Quantum Theory of Finite Systems(MIT Press, Cambridge, MA, 1986).

[5] S.C.Pieper , Nucl. Phys. **A751**(2005), 516.

[6] M.G.Mayer, Phys. Rev. **75**(1949)1969.

[7] C.H.Townes, H.M.Foley and W.Low, Phys. Rev. **76**(1949)1415.

[8] S.G.Nilsson, Dan. Mat . Fys. Medd. **29**, no.16 (1955).

[9] W.Nazarawicz, J.Dudek, R.Bengtsson, T.Bengtsson and I.Ragnarsson, Nucl. Phys. **A435**(1985), 397.

[10] A.Bohr, Dan. Mat . Fys. Medd. **26**, no.14 (1952).

[11] A.Bohr and B.R.Mottelson, Dan. Mat . Fys. Medd. **27**, no.16 (1953).

[12] J.W.Negele, Rev. Mod. Phys. **54**, 913 (1982).

[13] P.Bonche, S.Koonin and J.W.Negele, Phys. Rev. **C13**, 1226 (1976).

[14] R.Y.Cusson, R.K.Smith and J.A.Maruhn, Phys. Rev. Lett. **36**, 1166 (1976).

[15] H.Flocard, S.E.Koonin and M.S.Weiss, Phys. Rev. **C17**, 1682 (1978).

[16] R.Y.Cusson, J.A.Maruhn and H.W.Meldner, Phys. Rev. **C18**, 2589 (1978).

[17] J.W.Negele, S.E.Koonin, P.Möller, J.R.Nix, and A.J.Sierk, Phys. Rev. **C17**, 1098 (1978).

[18] J.A.Maruhn, P.G.Reinhard, P.D.Stevenson, J. R.Stone, and M.R.Strayer, Phys. Rev. **C71**, 064328 (2005).

[19] A.S.Umar and V.E.Oberacker, Phys. Rev. **C73**, 054607 (2006).

[20] A.S.Umar and V.E.Oberacker, Phys. Rev. **C76**, 014614 (2007).

[21] K.Washiyama and D.Lacroix, Phys. Rev. **C78**, 024610 (2008).

[22] C.Golabek and C.Simenel, Phys. Rev. Lett. **103**, 042701 (2009).

[23] T.Nakatsukasa and K.Yabana, J. Chem. Phys. **114**, 2550 (2001)

[24] T.Nakatsukasa and K.Yabana, Phys. Rev. **C71**, 024301 (2005).

[25] H.A.Bethe and R.F.Bacher, Rev. Mod. Phys. **8**(1936)82.

[26] A.Bohr, B.R.Mottelson and D.Pines, Phys. Rev. **110**, 936 (1958).

[27] J.Bardeen, L.N.Cooper and J.R.Shrieffer, Phys. Rev. **108**, 1175 (1957).

[28] W.J.Swiatecki, Phys. Rev. **100**(1955)937.

[29] Z.Ren and C.Xu, Nucl. Phys. **A759**(2005), 64.

[30] J.H.E.Mattuch, W.Thiele and A.H.Wapstra, Nucl. Phys. **67**(1965), 1.

[31] J.L.Wood, K.Heyde, W.Nazarawicz, M.Huyse and P.Van Duppen, Phys. Rep. **215** (1992) 101.

[32] S.G.Nilsson and O.Prior, Dan. Mat . Fys. Medd. **32**, no.16 (1961).

[33] I.Tanihata, H.Hamagaki, O.Hashimoto, Y.Shida, N.Yoshikawa, K.Sugimoto, O.Yamakawa, T.Kobayashi and N.Takahashi, Phys. Rev. Lett. **55**, 2676 (1985).

[34] I.Tanihata, J. Phys. G **22**, 157 (1996).

[35] A.Ozawa, T.Kobayashi, T.Suzuki, K.Yoshida and I.Yanihata, Phys. Rev. Lett. **84**, 5493 (2000).

[36] T.Otsuka, R.Fujimoto, Y.Utsuno, B.A.Brown,M.Honma and T.Mizusaki, Phys. Rev. Lett. **87**, 082502 (2001).

[37] M.Matsuo, K.Mizuyama and Y.Serizawa, Phys. Rev. **C71**, 046326 (2005).

[38] M.Matsuo, Phys. Rev. **C73**, 044309 (2006).

[39] E.Litvinova, P.Ring and V.Tselyaev, Phys. Rev. **C78**, 014312 (2008).

[40] N.Paar, T.Nikšić, T.Marketin, D.Vretenar and P.Ring, Eur. Phys. J. A **25**, 531 (2006).

[41] D.Vretenar, N.Paar a, P.Ringa, G.A.Lalazissis, Nucl. Phys. **A692**(2001), 496.

[42] S.Goriely, Phys. Lett. B **436**, 10 (1998).

[43] S.Goriely and E.Khan, Nucl. Phys. **A706**(2002), 217.

[44] E.K.Warburton, J.A.Becker and B.A.Brown, Phys. Rev. **C41**, 1147 (1990).

[45] O.Sorlin, C.Donzaud, F.Nowacki, J.C.Angélique, F.Azaiez, C.Bourgeois, V.Chiste, Z.Dlouhy, S.Grévy, D.Guillemaud-Mueller, F.Ibrahim, K.-L Kratz, M.Lewitowicz, S.M.Lukyanov, J.Mrasek, Yu.-E.Penionzhkevich, F.de Oliveira Santos, B.Pfeiffer, F.Pougheon, A.Poves, M.G.Saint-Laurent, M.Stanoiu, Eur. Phys. J. A **16**, 55 (2003).

[46] N.Aoi, E.Takeshita, H.Suzuki, S.Takeuchi, S.Ota, H.Baba, S.Bishop, T.Fukui, Y.Hashimoto, H.J.Ong, E.Ideguchi, K.Ieki, N.Imai, M.Ishihara, H.Iwasaki, S.Kanno, Y.Kondo, T.Kubo, K.Kurita, K.Kusaka, T.Minemura, T.Motobayashi, T.Nakabayashi, T.Nakamura, T.Nakao, M.Niikura, T.Okumura, T.K.Ohnishi, H.Sakurai, S.Shimoura, R.Sugo, D.Suzuki, M.K.Suzuki, M.Tamaki, K.Tanaka, Y.Togano, and K.Yamada, Phys. Rev. Lett. **102**, 012502 (2009).

[47] O.B.Tarasov, D.J.Morrissey, A.M.Amthor, T.Baumann, D.Bazin, A.Gade, T.N.Ginter, M.Hausmann, N.Inabe, T.Kubo, A.Nettleton, J.Pereira, M.Portillo, B.M.Sherrill, A.Stolz, and M.Thoennessen, Phys. Rev. Lett. **102**, 142501 (2009).

[48] M.Stoitsov, J.Dobaczewski, W.Nazarewicz, and P.Ring, Comput. Phys. Commun. **167**, 43 (2005).

[49] B.Avez, C.Simenel and Ph.Chomaz, Phys. Rev. **C78**, 044318 (2008).

[50] Y.Hashimoto and K.Nodeki, arXiv:0707.3083

[51] J.Terasaki and J.Engel, Phys. Rev. **C74**, 044301 (2006).

[52] M.Matsuo, Nucl. Phys. **A696**(2001), 371.

[53] E.Khan, N.Sandulescu, M.Grasso, and Nguyen Van Giai, Phys. Rev. **C66**, 024309 (2006).

[54] M.Bender, J.Dobaczewski, J.Engel, and W.Nazarewicz, Phys. Rev. **C65**, 054322 (2006).

[55] K.Yoshida and Nguyen Van Giai, Phys. Rev. **C78**, 064316 (2008).

[56] C.Losa, A.Pastore, T.Døssing, E.Vigezzi, and R.A.Broglia, Phys. Rev. **C81**, 064307 (2010).

[57] J.Terasaki and J.Engel, Phys. Rev. **C82**, 034326 (2010).

[58] J.Błocki and H.Flocard, Nucl. Phys. **A273**(1976), 45.

[59] T.Nakatsukasa, T.Inakura, and K.Yabana, Phys. Rev. **C76**, 024318 (2007).

[60] N.Tajima, S.Takahara, and N.Onishi, Nucl. Phys. **A603**, 23 (1996).

[61] M.Brack, J.Damgaard, A.S.Jensen, H.C.Pauli, V.M.Strutinsky, and C.Y.Wong, Rev. Mod. Phys. **44**, 320 (1972).

[62] K.T.R.Davies, H.Flocard, S.Krieger, and M.S.Weiss, Nucl. Phys. **A342**, 111 (1980).

[63] J.Bartel, P.Quentin, M.Brack, C.Guet, and H.Håkansson, Nucl. Phys. **A386**, 79 (1982).

[64] P.Bonche, H.Flocard, and P.H.Heenen, Nucl. Phys. **A467**,115 (1987).

[65] E. Chabanat, P.Bonche, P.Haensel, J.Mayer and R.Schaeffer, Nucl. Phys. **A627**,710 (1997).

[66] T.Inakura, T.Nakatsukasa and K.Yabana, Phys. Rev. **C80**, 044301 (2009).

[67] A.Veyssière, H.Beil, R.Bergère, P.Carlos, A.Leprêtre and K.Kernbath, Nucl. Phys. **A199**, 45 (1973).

[68] V.V.Varlamov, M.E.Stepanov, and V.V.Chesnokov, Bull. Rus. Acad. Sci. Phys. **67**, 724 (2003).

[69] J.Ahrens, H.Borchert, K.H.Czock, H.B.Eppler, H.Gimm, H.Gundrum, M.Kröing, P.Riehn, G.Sita Ram, A.Zieger and B.Ziegler, Nucl. Phys. **A251**, 479 (1975).

[70] A.Veyssière, H.Beil, R.Berge, P.Carlos, A.Leprêtre and A.De Miniac, Nucl. Phys. **A227**, 513 (1974).

[71] H.B.A.Leprêtre, R.Bergère, P.Carlos, A.Veyssière and M.Sugawara, Nucl. Phys. **A175**, 609 (1971).

[72] A.Veyssière, H.Beil, R.Berge, P.Carlos and A.Leprêtre, Nucl. Phys. **A159**, 561 (1970).

[73] P.Carlos, H.Beil, R.Berge, A.Leprêtre, A.De Miniac and A.Veyssière, Nucl. Phys. **A225**, 171 (1974).

[74] P.Carlos, H.Beil, R.Berge, A.Leprêtre, A.De Miniac and A.Veyssière, Nucl. Phys. **A172**, 437 (1971).

[75] C.F.von Weizsäcker, Z. Phys. **96**(1935)431.

[76] J.Gibelin, D.Beaumel, T.Motobayashi, Y.Blumenfeld, N.Aoi, H.Baba, Z.Elekes, S.Fortier, N.Frascaria, N.Fukuda, T.Gomi, K.Ishikawa, Y.Kondo, T.Kubo, V.Lima, T.Nakamura, A.Saito, Y.Satou, J.-A.Scarpaci, E.Takeshita, S.Takeuchi, T.Teranishi, Y.Togano, A.M.Vinodkumar, Y.Yanagisawa, and K.Yoshida, Phys. Rev. Lett. **101**, 212503 (2008).

[77] L.-G.Cao and Z.-Y.Ma, Phys. Rev. **C71**, 034305 (2005).

[78] J.Piekarewicz, Phys. Rev. **C73**, 044325 (2006).

[79] M.Yamagami and K.Matsuyanagi, Nucl. Phys. **A672**, 123 (2000).

[80] K.Hagino, N.W.Lwin and M.Yamagami, Phys. Rev. **C74**, 017310 (2006).